Author:
Robinson, Benjamin D

Title:
Multi-frequency nonlinear ultrasonic diffuse imaging for material and defect characterisation

MULTI-FREQUENCY NONLINEAR ULTRASONIC DIFFUSE IMAGING FOR MATERIAL AND DEFECT CHARACTERISATION

By

Benjamin D Robinson

Department of Mechanical Engineering
University of Bristol

A dissertation submitted to the University of Bristol in accordance with the requirements of the degree of Doctor of Philosophy in the Faculty of Engineering.

December 2021

Word count: 35,661

For my parents

Abstract

Advances in ultrasonic nonlinear imaging techniques have increased the detectability of fatigue cracks during earlier stages of formation. This thesis explores the novel nonlinear ultrasonic diffuse energy imaging (NUI) technique used for non-destructive testing (NDT). In contrast to current linear methods the NUI method is able to image tightly closed crack tips and quantify the degree of nonlinearity present in the defect without the need for mechanical scanning or complicated bespoke set-ups. More specifically, unlike nonlinear coherent methods the NUI method is able to resolve nonlinear closed crack tips without the need for coherent reflections from damage, meaning the orientation of the crack tips is not required and the method can be extended to classical nonlinearity induced by lattice anharmonicity and dislocations.

A sensitivity analysis of the NUI technique is first explored to establish the sensitivity profile of the method and further understand the detectability of nonlinear features in materials. This is achieved through experimental and simulated data, and explores the influence of attenuation and transmission frequency on detectability of nonlinear features. Consistent sensitivity over the frequency transmission range investigated is observed and is attributed to the competing effects of increased attenuation and nonlinearity as frequency increases. The knowledge of the sensitivity profile is then used to investigate a multi-view diffuse method to allow optimisation of the position of the sensitivity profile used to detect the nonlinear feature. This is only effective at 5 MHz where a nonlinear feature is detected very close to the array which is otherwise undetectable using the existing single-view NUI technique.

Further optimisations of the NUI technique are investigated. Firstly, a multi-frequency adaptation is explored and compares the sensitivity of the NUI technique using varying transmission frequencies and receiving at different frequency components (low, sub-harmonic, fundamental and second harmonic). The most effective configuration is transmitting at 5 MHz and receiving at the low frequency and the second harmonic component. A phase metric is also investigated in an attempt to reduce the diffuse field dependency of this method. The results show some reduction in sensitivity to the diffuse field, suggesting there is some benefit to computing the proposed phase metric over the current energy metric. The optimisation of the diffuse time parameters is investigated and a phase coherence metric is established to process full matrix capture (FMC) data and determine the time in which ultrasonic energy has homogenised in the material. The results suggest the metric converges when the field is diffuse and is tested with the experimental performance of the NUI technique in imaging a crack tip.

Finally, using the optimisations proposed in this thesis the detection of classical nonlinearity (lattice anharmonicity and dislocations) is investigated on dog-bone samples subjected to loading from a 4-point bending jig. This study concludes that the NUI method requires further optimisation to detect lower-level classical nonlinearity.

Acknowledgements

I would like to express my sincere gratitude to my project supervisors Professor Anthony Croxford and Professor Bruce Drinkwater. I would also like to acknowledge Dr Jack Potter for his guidance during the early stages of my PhD and Dr Rhodri Beaven for his invaluable support in the UNDT lab.

I am also grateful to the technical staff at the University of Bristol for their support and expertise in manufacturing of specimens required for experimental work.

Thank you to the Engineering and Physical Sciences Research Council (EPSRC) and the NDE Research Association (NDEvR; Rolls-Royce, EDF, Hitachi and SKF) for funding the research.

I'd also like to thank the members of the UNDT and Ultrasonics research group at Bristol for their inspiring conversations and friendship.

Finally, I would like to express my gratitude to my family for their emotional support and encouragement during my studies. It wasn't until submission I was able to reflect on how supportive they had been.

Author's declaration

I declare that the work in this dissertation was carried out in accordance with the requirements of the University's *Regulations and Code of Practice for Research Degree Programmes* and that it has not been submitted for any other academic award. Except where indicated by specific reference in the text, the work is the candidate's own work. Work done in collaboration with, or with the assistance of, others, is indicated as such. Any views expressed in the dissertation are those of the author.

SIGNED: ..... DATE: .....

Contents

List of Figures

List of Tables

Nomenclature

α_l, α_s	attenuation coefficient: longitudinal and shear
A, B, C	Landau-Lifshitz third order elastic constants: first, second, third
c_l, c_s	sound speed: longitudinal and shear.
δ_j^T	Transmission delay law for each jth element to focus at an inspection point
ϵ	Strain
E	Young's Modulus
$F_{j,k}(t)$	Sequential frequency domain received signals for each combination of transmitter (j) and receiver (k) elements in the full matrix capture
$f_{j,k}(t)$	Sequential time domain received signals for each combination of transmitter (j) and receiver (k) elements in the full matrix capture
$H_{j,k}(t)$	Parallel frequency domain received signals for each receiver (k) elements
$h_{j,k}(t)$	Parallel time domain received signals for each receiver (k) elements
k	wave number
l, m, n	Murnaghan constants: first, second, third
β	Nonlinearity parameter
N	Number of elements
ρ	Density of material
σ	Stress
σ_0	Initial static stress
τ	moving window length
t	time
T	Record window length
t_e	end gate-time

T_n	moving window number
t_s	start gate-time
u	Particle displacement
ν	Poisson's ratio
x, y, z	Cartesian spatial coordinates

Chapter 1

Introduction

This thesis is concerned with the development and optimisation of the nonlinear ultrasonic diffuse energy imaging (NUI) technique for monitoring crack growth in mechanical components. The aim of this thesis is to enhance current techniques to increase the detectability of closed crack tips and automate this method for industrial use by investigating its optimisation on artificially grown nonlinear damage in Aluminium.

In the aerospace and power generation industries, metallic parts such as pipelines, nuclear reactors and aerospace components are subjected to cyclic high pressures and temperatures which reduce their operational lifetime. The reliability and integrity of these structures are key to ensure safe operation. It is known that materials used in these industries experience fatigue, thermal ageing, creep, plasticity and radiation damage all of which cause the material to become more nonlinear [9]. Most notably, crack growth caused by cyclic loading occurs frequently in engineering structures and components. Such fatigue is hard to detect early in life, therefore detection methods are desirable to plan maintenance repairs for improved safety. The consequence of these processes is the demand for *in situ* testing of components in-order to detect defects and quantitatively determine their remaining life at earlier stages of fatigue to ensure safe operation.

It is vital to use reliable non-destructive testing (NDT) methods for early detection of these defects to plan maintenance and guarantee safety. Conventional linear ultrasonic methods, using a variety of transmit and receive configurations, have proven effective in imaging these defects, however these methods are considered inaccurate at early stages of degradation where the crack tip is partially or fully closed, due to limited reflections from the damage [10–12]. Therefore these conventional methods are optimised and focused towards identifying fatigue cracks towards the middle or end of the components lifetime. The result of these limitations is relatively short intervals for inspection and higher safety factors to ensure the detectability of fast growing crack tips, reducing efficiency and increasing cost.

Nonlinear methods have been developed to detect the response from micro-structural fatigue which precedes crack growth in engineering components. As micro-structural degradation (such as dislocations) persists, cracks initiate and grow (initially tightly closed), exhibiting nonlinear effects from opening and closing. This nonlinear mechanism becomes a dominant feature to measure and allows for the detection of fatigue crack tips prior to the development of volumetric damage (which can then be detected using conventional methods). Micro-structural nonlinearity is classified in two groups: classical and non-classical. Classical nonlinearity is induced when a longitudinal wave propagates through a medium with a nonlinear stress-strain relationship (which occurs in all materials). The stress-strain relationship is generally defined as quadratic and is generated by dislocations and lattice anharmonicity [13–15]. Non-classical nonlinearity is induced by crack tips where the interface of the crack opens and closes, and only allows the compressional component of the wave to transmit [2, 16, 17]. Both nonlinear mechanisms produce measurable nonlinearity in received ultrasonic signals allowing for detection of fatigue damage before the formation of larger volumetric defects. Several ultrasonic nonlinear measurement techniques have been developed that capitalise on induced second harmonic generation (SHG) and frequency modulation caused by classical [18, 19] and non-classical [20–22] nonlinearity. However, the requirement for complicated configurations

for these experiments limits these methods to lab research and prevents industrial deployment [23–26], and will be discussed in more detail in Section 2.2.

Recent advances in the field have enabled the development of nonlinear phased array methods which increase the applicability of nonlinear measurement techniques for industrial use, by removing the requirement for mechanical scanning and reducing the inspection time. Such approaches have been effective in detecting and spatially resolving nonlinear features [5, 27,28] using a variety of transmit and receive configurations. These nonlinear methods are split into two main groups: coherent and diffuse. The nonlinear phased array coherent techniques evaluate the transfer of energy to additional harmonics present in the wave backscattered from the point of inspection, such as the fundamental wave amplitude difference technique [3, 28], fundamental sequential-parallel subtraction method [27] and sub-harmonic methods [4]. The key requirement of these methods are linear reflections from the nonlinear damage at the inspection point, therefore the orientation of damage such as fatigue crack tips can influence their reliability.

The stochastic formation of closed crack tips means the orientation of the crack tip is not known, therefore a technique that does not rely on linear scattering is desirable. The second type of nonlinear phased array method is the NUI technique which removes the dependency of linear scattering on the detectability of defects. The NUI technique evaluates the nonlinearity once the field is diffuse, that is, statistically uniform throughout the specimen [5]. The benefit of this technique is that it does not rely on backscatter from the inspection point and therefore it has the potential to resolve classical nonlinearity, such as bulk material nonlinearity. Since the closed crack tips are typically generated from the surface or larger volumetric fatigue, contact-acoustic nonlinearity (CAN) sources are generally located near a large linear scatterer, allowing for the nonlinear information to propagate back to the array. However, bulk nonlinearity induced by strain-fields is generally distributed throughout the material and therefore close proximity to

linear reflectors is less likely, meaning the nonlinearity can not propagate back to the array. This NUI technique implements the same parallel-sequential subtraction method but captures information later in time when the field is diffuse. The key requirement of the NUI technique is that the energy is diffuse throughout the specimen before the receivers begin to capture the signal, meaning the relative loss of energy from the focal point diffuses uniformly through the material. As such, the relative diffuse energy between the parallel and sequential field is proportional to the energy lost at the focal point, and therefore proportional to the nonlinearity at that location [5]. The optimisation of the time when the receivers begin and stop capturing the field is vital to ensure that the ultrasonic data is diffuse and contains the smallest contribution from noise. This optimisation is therefore critical for the practical implementation of this technique.

1.1 Thesis objectives

The focus of this thesis is the optimisation of the NUI technique to increase the detectability of fatigue crack tips, which will allow earlier detection of fatigue. This will be achieved through a number of optimisations investigated on artificially produced crack tips.

Firstly, the sensitivity profile of the NUI method for detecting fatigue crack tips will be investigated, achieved through experimental and simulation investigation. The purpose of this is to spatially determine the most detectable region of the array and study the influence of attenuation rates and transmission frequency on the detectability of the NUI method. Using the known sensitivity profile an optimised detection method is proposed to control the point of the sensitivity profile used to detect the crack tip. To increase detectability further, nonlinear energy at various reception frequencies are investigated, introducing a multi-frequency method which evaluates the nonlinear energy at nonlinear components within the spectrum. The performance of the alternative frequencies are compared via signal-to-noise ratio (SNR) measurements to establish the most effective frequencies for localising fatigue crack tips. The most effective configuration can then be used to resolve nonlinear features more accurately and resolve lower levels of nonlinearity, which allows for earlier detection of fatigue crack tips.

The detectability of nonlinear features using the NUI technique is highly dependent on the diffuse field, therefore the capturing of data during a diffuse state is vital to detect fatigue cracks at early stages of development. Therefore, the dependency of NUI on the diffuse field is investigated, and a diffuse field metric is established to approximate the time the field has homogenised. The capture of data in an optimally diffuse state will allow for increased detectability of crack tips. In addition, to reduce the dependency of NUI on the diffuse field, a phase NUI metric is introduced.

Finally, using the multi-frequency method, diffuse metric optimisations and sensitivity

optimisations, an investigation into resolving bulk material nonlinearity (classical nonlinearity) will be conducted. This is investigated using samples containing a strain field induced via loading and attempts to validate the NUI method for determining classical nonlinearity.

1.2 Thesis outline

The structure of this thesis is consistent with the objectives described in the previous section and is as follows:

A literature review is presented in Chapter 2 which reviews the literature principally relevant to this thesis. Firstly, nonlinear wave propagation and classical/non-classical nonlinearity is introduced to set the theoretical baseline of the project. Subsequently, nonlinear measurement techniques are compared (second harmonic measurement and wave-mixing) to introduce various methods for measuring nonlinearity induced by fatigue. The development of ultrasonic phased arrays for various transmission configurations and conventional linear imaging methods is introduced. Following this, the nonlinear phased array methods are introduced in two categories: coherent and diffuse methods. The advantages and disadvantages of both these methods are compared in depth.

Chapter 3 investigates the NUI sensitivity profile of the array through analysis of experimental and simulation results. Using knowledge of the sensitivity profile a multi-view diffuse method is proposed to provide some dynamic control over the sensitivity of the array. The efficacy of transmission frequencies for detecting fatigue crack tips is also investigated to determine the most effective frequencies for exciting nonlinearity induced by crack tips.

Chapter 4 investigates an adaptation of the single NUI method which measures nonlinear energy at multiple frequencies. This chapter evaluates the performance of each nonlinear frequency component in detecting fatigue crack tips by comparing the SNR of each image

with the current single frequency method. Following this analysis a frequency combination for transmission and reception is determined to ensure maximum nonlinear resolution of features.

Chapter 5 investigates two phase metrics for detecting fatigue crack tips in test specimens. The performance of the metrics is compared with the SNR of the current NUI metric for multiple start gate-times. This process evaluates how the performance of the metrics vary with a change in the diffuse field state. Since there is a limitation in achieving a diffuse state in large geometries, a metric less reliant on the diffuse field is desired.

Chapter 6 introduces a phase coherence metric for determining the time in which the energy in the wave-field has homogenised and a diffuse field has been achieved. This metric is tested against the performance of NUI for multiple start gate-times and investigates multiple parameters (e.g. cycle length, sample volume and frequency transmission).

Chapter 7 employs the optimisations discovered in the previous chapters and investigates the detection of material nonlinearity induced by strain-fields from fatigue. Using the most effective multi-frequency configuration, the proposed multi-frequency method and the diffuse phase coherent metric, the efficacy of NUI for resolving material nonlinearity is extensively explored.

Chapter 8 concludes the findings of the thesis and suggests the direction of further research. This includes the future applications of optimisations, and additional optimisations required.

Chapter 2

Nonlinear wave propagation and NDT

In this chapter literature relevant to the research in this thesis will be discussed. Firstly, the general principles of elastic nonlinear wave propagation will be introduced. The measurement of elastic non-linearity has been investigated in multiple fields [29]. Most notably, the micro-structure of crystalline metallic materials (such as dislocations, precipitates and micro-cracks) have been shown to induce elastic nonlinearity, first observed using acousto-elastic methods [30, 31]. This led to the development of ultrasonic nonlinear methods for the quantitative measurement of micro-structural changes, such that early material degradation and remaining life of components can be estimated. This subsection presents a theoretical overview of elastic nonlinearity in two different forms: classical and non-classical.

Nonlinear ultrasonic measurement techniques can be broadly categorised into three groups: second harmonic generation (SHG), nonlinear spectroscopy and nonlinear ultrasonic phased arrays. The first method measures the second harmonic (or higher) wave generated in the nonlinear medium or a third wave which is generated through wave mixing. These methods provide a global measure of classical nonlinearity in the material and can estimate the fatigue (e.g. dislocations) in the material. The second class is nonlinear spectroscopy methods which measure nonlinearity through analysis of the frequency spectra at points in the material to

resolve various types of nonlinear damage. This method has shown to be sensitive to damage precursors or discrete defects, for global or localised measurements. The third class are nonlinear phased array methods which are capable of spatially resolving elastic nonlinearity in materials. These methods have emerged in recent years, and have shown potential in localising closed crack tips. Firstly, linear phased array methods will be introduced to outline the fundamental processing used for phased array configurations. The nonlinear methods, which use a variety of transmission configurations and processing procedures, will then be discussed in depth to establish the advantages and disadvantages of each method.

2.1 Elastic nonlinearity in solids

2.1.1 Derivation of the nonlinear wave equation (classical)

In the context of damage characterisation the most commonly adopted nonlinear ultrasonic technique is measurement of the second harmonic generated wave. This method is concerned with measuring the distortion of a sinusoidal wave of a given frequency through a nonlinear medium. This distortion is observed as a transfer of energy away from the excitation frequency, typically to the second harmonic. The amplitude of generated higher harmonics decreases with increasing order, therefore this technique generally only considers the second harmonic. The elastic nonlinearity of a medium can then be inferred by the relative amplitudes of the excitation frequency and higher harmonics. The following section will outline the derivation of nonlinear wave propagation, assuming longitudinal wave propagation in an isotropic nonlinear medium.

To begin this analysis we must first introduce the nonlinear Hooke's law, which assumes quadratic nonlinearity and higher orders for the relationship between stress and strain,

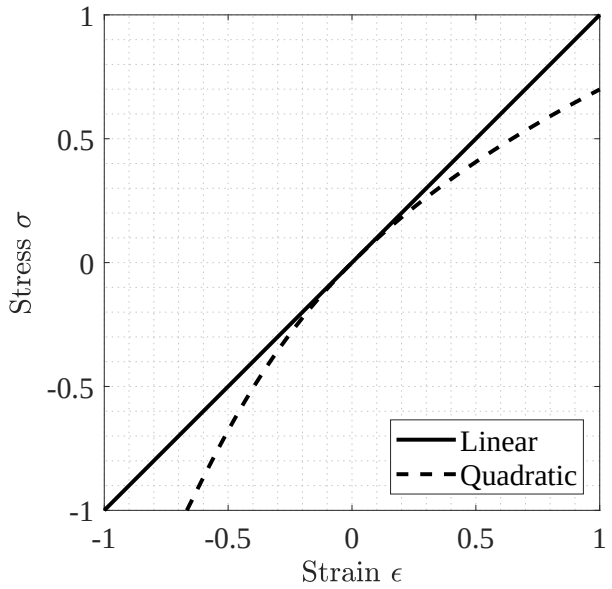

FIGURE 2.1: Illustration of quadratic nonlinearity

$$\sigma = E\epsilon(1 + \beta\epsilon + ...) \tag{2.1}$$

where σ is the stress, ϵ is the strain, E is the Young's Modulus and β is the nonlinearity parameter. An illustrative comparison of linear and quadratic stress-strain relationships can be seen in Fig. 2.1. The equation of motion for the propagation of a one dimensional elastic wave in an isotropic medium is defined as,

$$\rho\frac{\partial^2 u}{\partial t^2} = \frac{\partial \sigma}{\partial x} \tag{2.2}$$

where ρ is the density of the material, u is the particle displacement, t is the temporal co-ordinate and x is the propagation distance. The strain can be related to the particle displacement via the following expression,

$$\epsilon(x,t) = \frac{\partial u(x,t)}{\partial x} \tag{2.3}$$

When considering quadratic nonlinearity, an adaptation of the wave equation is required to produce a nonlinear equation of motion. Only the first few terms are required from a Taylor series expansion as the displacement of ultrasonic wave are so small that the contribution of higher order derivatives is minimal. Therefore by truncating Eq. 2.1 to the second term, and using Eq. 2.2 and Eq. 2.3 the nonlinear wave equation is derived,

$$\rho\frac{\partial^2 u}{\partial t^2} = E\frac{\partial^2 u}{\partial x^2} + 2E\frac{\partial}{\partial x}\left[\beta\left(\frac{\partial u}{\partial x}\right)^2 + \ldots\right] \tag{2.4}$$

The second term on the right represents the quadratic nonlinearity. Note that if the nonlinearity parameter $\beta = 0$, then the equation will return to the linear wave equation. In the case of material nonlinearity in metallic solids, induced by lattice anharmonicity and dislocations, the nonlinear conversion is relatively low [32], meaning the nonlinear term in Eq. 2.4 is significantly lower than the linear term. This allows the solution of the nonlinear wave equation to be derived by the perturbation method (a full explanation of this method can be found in the work by Ginsberg (1998) [33]). Adopting this method, the solution is assumed to take the following form,

$$u = u^{(0)} + u^{(s)} \tag{2.5}$$

where u is the total response, u_0 is the incident (linear) field and u_s the secondary (nonlinear) field. The secondary field is the "perturbation" away from the linear response due to the quadratic nonlinearity. The perturbation method assumes that the nonlinearity is small and does not influence the linear field (a quasi-linear approximation). The linear equation is formed from Eq. 2.4 by replacing the $u = u^0$ and $\beta = 0$, obtaining:

$$\rho \frac{\partial^2 u^{(0)}}{\partial t^2} = E \frac{\partial^2 u^{(0)}}{\partial x^2} \tag{2.6}$$

The nonlinear equation for the secondary field can then be formed by using $u^{(0)}$ in the nonlinear forcing terms in Eq. 2.4 giving,

$$\rho \frac{\partial^2 u^{(s)}}{\partial t^2} = E \frac{\partial^2 u^{(s)}}{\partial x^2} + 2E \frac{\partial}{\partial x} \left[\beta \left(\frac{\partial u^{(0)}}{\partial x} \right)^2 \right] \tag{2.7}$$

To derive the linear solution, we can define the source excitation as $u = U_0 \sin(-\omega t)$ and therefore the solution as a sinusoidal forward propagating harmonic wave,

$$u^{(0)} = U_0 \sin(kx - \omega t) \tag{2.8}$$

where U_0 is the source excitation amplitude, k is the wave number and ω is the angular frequency. Next, it is necessary to substitute $u^{(0)}$ as the forcing terms on the right hand side of Eq. 2.7, resulting in

$$\rho \frac{\partial^2 u^{(s)}}{\partial t^2} - E \frac{\partial^2 u^{(s)}}{\partial x^2} = -E\beta U_0^2 k^3 \sin[2(kx - \omega t)] \tag{2.9}$$

Next we adopt the trial solution,

$$u^{(s)} = f(x) B \cos[2(kx - \omega t)] \tag{2.10}$$

where f is a function of the distance and B is a constant. To obtain the solution for the fundamental and second harmonic waves it is necessary to substitute this solution into Eq. 2.9 implementing the perturbation method of multiple scales, giving the following solution:

$$u = u^{(0)} + u^{(s)} = U_0 \sin(kx - \omega t) + \frac{\beta}{4} U_0^2 k^2 x \cos[2(kx - \omega t)] \tag{2.11}$$

This equation indicates that the nonlinear perturbation from the linear propagation oscillates at twice the fundamental frequency. From this solution we can derive the amplitude A_1 and A_2, corresponding to the fundamental and second harmonic respectively, giving

$$A_1 = U_0 \tag{2.12}$$

$$A_2 = \beta / 4 k_0^2 U_0^2. \tag{2.13}$$

These equations can be combined and rearranged to calculate the nonlinearity parameter as a function of the relative amplitudes between the fundamental and second harmonic,

$$\beta = \frac{4}{k^2 x} \frac{A_2}{A_1^2} \tag{2.14}$$

where β is calculated for a given distance and excitation frequency. Typically, the nonlinearity parameter is measured in a through transmission configuration where the nonlinear material is excited using a single-frequency and the signal is received on the opposite side of the material. Through Fourier analysis it is then possible to calculate the relative amplitude of the fundamental and second harmonic. This method will be discussed further in Section 2.2 in more detail.

2.1.2 Definition of β

The calculation of β can be inferred through bulk wave analysis as derived in the previous section. The nonlinearity parameter can also be related to three elastic parameters known as third-order elastic constants (TOECs) which describes isotropic quadratic nonlinearity in three dimensions. TOECs can be represented as A, B and C known as the Landau-Lifshitz third order elastic constants [34]. Alternately, these constants can be expressed as Murnaghan constants [29] as $l = B + C$, $m = A/2$ and $n = A$. The nonlinearity parameter related to the TOECs is expressed as,

$$\beta = -\left(\frac{\frac{3E(1-\nu)}{(1+\nu)(1-2\nu)} + 2A + 6B + 2C}{\sigma_0 + \frac{E(1-\nu)}{(1+\nu)(1-2\nu)}} \right) \tag{2.15}$$

where ν is Poison's ratio.

The parameter β is determined primarily by the crystalline structure, in particular any lattice anharmonicity (i.e. asymmetry of the lattice) present in the structure. Additionally, local stress fields induced by varying micro-structural effects contribute to β known as dislocations, which are crystallographic defects in the crystal structure which cause changes in the atomic arrangement.

Dislocations induced by degradation result in a nonlinear relationship between the glide displacement and the applied stress. Without pinning, this dislocation contributes to elastic nonlinearity and is further increased when the dislocation becomes pinned between two points [13]. This pinning can be caused by other dislocations, grain boundaries and precipitates or other material inclusions. When the movement of the dislocation is slowly limited by the local stress state of these pinning points the dislocation will bow. Once this occurs the total

strain will be the sum of both the lattice strain and the bowed dipole, producing a nonlinear stress-strain relationship. The dependence of β on dislocations is also determined by the type. For example, edge dislocations have proven to induce larger nonlinear effects than screw dislocations [14].

Dislocation dipoles occur when two pinned dislocations are in close enough proximity to become one single dynamic system. The stress-strain relationship of these dipoles are inherently nonlinear, contributing to local elastic nonlinearity and therefore the parameter β. Theoretical models have been validated against experimental work investigating the contribution of elastic nonlinearity from dipoles by measurement of the second harmonic (β parameter) [15, 30]. Cyclic loading promotes mutual trapping of dislocations as they move in response to cyclic stresses, this can lead to the formation of single dislocations (monopoles), a complex arrangement of dipoles or even multi-poles.

The presence of precipitates also contributes to the value of β. In isolation precipitates do not directly influence β, however in the presence of dislocations a resulting stress-field is induced and contributes to the magnitude of β. The magnitude of the bulk nonlinear response is determined by the volumetric density and distribution of the precipitates. Most types of damage (e.g. fatigue, creep, damage, thermal ageing and radiation) are produced by the generation of precipitate dislocations, therefore the degree of damage can be determined by the magnitude of β. However, the precise dependency of β on damage type requires significant consideration of both the micro-structure and the damage type.

Over time these dislocations can lead to the development of closed crack tips or kissing bonds, where the surface of the crack interfaces are in-contact but not bonded. This type of fatigue damage induces additional non-classical forms of nonlinearity.

2.1.3 Contact-acoustic effects (non-classical)

At later stages of fatigue damage weaker classical sources of nonlinearity such as dislocations and micro-structural degradation leads to the development of crack tips which induce a non-classical form of nonlinearity. Previous studies have reported contact-acoustic nonlinearity (CAN), which occurs when an ultrasonic wave is incident on an un-bonded interface (but still in contact), which can cause nonlinearity due to self induced hysteretic behaviour [35] and a clapping effect [2, 16, 17]. This highly nonlinear effect has been observed for ultrasonic waves in fatigue crack tips and kissing bonds (bonded joints) [36, 37]. Using theoretical models and appropriate measurement techniques it is possible to quantify CAN.

When an ultrasonic wave is incident on an un-bonded surface the tensile stress component of the wave acts to open the interface of the crack tip, weakening the contact between the interfaces and inhibiting the transmission of the wave across the interface. The compressional component strengthens the interface by increasing the elasticity (through contact) between the two interfaces, allowing efficient transmission of the ultrasonic wave. The consequence of this interference results in bi-linear stress-strain relationship expressed as,

$$\sigma = E(1 - H(\epsilon - \epsilon_0)\frac{\Delta E}{E})\epsilon, \tag{2.16}$$

where H denotes a Heaviside function and ϵ_0 is the initial static strain at the interface. An illustration of this bi-linear stress-strain relationship is displayed in Fig. 2.2.

The bi-linear stress-strain relationship leads to a number of nonlinear dynamic responses. These non-classical effects contribute to super-harmonics and higher, which is consistent with classical nonlinear effects [38]. However, harmonic contributions caused by CAN also exist at sub-harmonics (i.e. $\omega/2$, $3\omega/2$, $\omega/3$, $2\omega/3$) in respect to the incident wave frequency

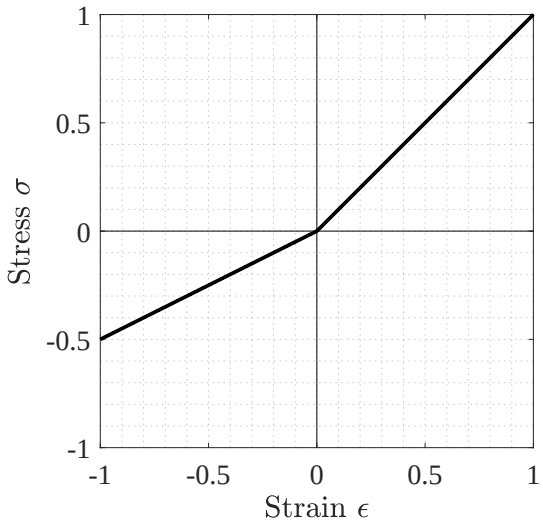

FIGURE 2.2: Illustration of bi-linear nonlinearity contact acoustic effects.

(ω) [39–41]. These harmonic contributions are easily differentiated from classical nonlinearity, meaning it is possible to directly measure these harmonics in order to characterise nonlinear defects.

Furthermore, when the shear component of a wave is at a normal incident to an un-bonded interface, the interface will exhibit frictional nonlinear effects. This results in the following mechanisms: a coulombs law with a constant friction coefficient and a slip-weakening friction law which consists of static and varying friction laws [42]. The state of this slip-stick behaviour is dependent on the magnitude of the incident shear wave stress, as large stresses are required to activate the slip, known as the threshold effect. This nonlinear mechanism is independent on loading direction, therefore the nonlinear stress-strain relationship is symmetrical and are illustrated in Fig. 2.3. The frictional nonlinear mechanisms parallel to the interface combined with the clapping effect in normal direction results in cumulative nonlinear dynamics known as non-classical.

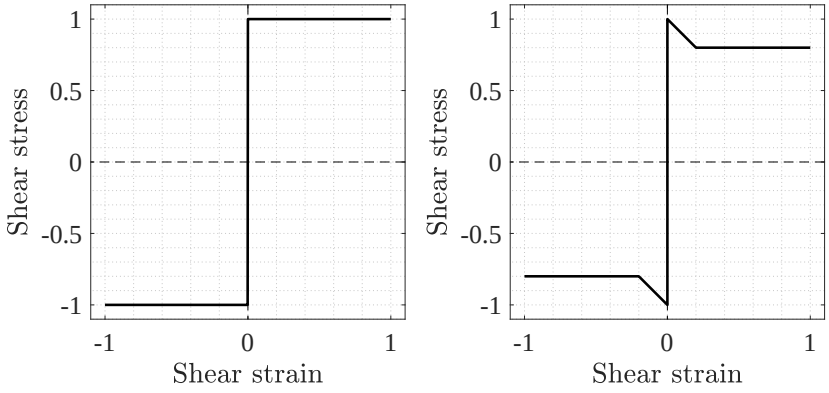

FIGURE 2.3: Illustration of shear stress-strain relationship: (a) coulomb friction law and (b) slip-weakening friction law.

2.2 Nonlinear measurement techniques

The next section will introduce the nonlinear measurement techniques implemented to detect the nonlinear mechanics outlined in the previous section. These techniques are broadly categorised into the following groups: second harmonic generation (SHG), wave mixing, nonlinear spectroscopy and phased array methods. The advantages and disadvantages of each method is discussed in depth to highlight the focus of this thesis.

2.2.1 Second harmonic generation measurement techniques

The most conventional techniques for measuring classical nonlinearity are measurement of the second harmonic generation (SHG), which has been implemented successfully for detecting nonlinearity induced by lattice anharmonicity (i.e. dislocations and dipoles) [18, 19]. When a longitudinal wave propagates through a quadratic nonlinear medium, the wave interacts with

itself causing energy to be transferred to the second harmonic. The propagating pulse continuously generates a second harmonic which constructively interferes along the propagation path, causing the second harmonic to grow with distance travelled. As mentioned previously in Section 2.1.1, the relationship between the fundamental transmission frequency and the second harmonic can be used to determine the nonlinearity parameter β. Therefore, it is possible to determine experimentally the degree of classical nonlinearity in a medium by measuring the amplitude at the second harmonic. The analytical definition of β dictates that it is a cumulative measure of nonlinearity over the propagation distance, meaning it is not possible to spatially resolve β at different distances. Subsequently, it is only possible to measure the nonlinearity once the wave has propagated to the surface, meaning it is only possible to measure SHG at the surface.

The requirement of this measurement technique is that there is two-sided access to the material, which is necessary to measure the ultrasonic wave at some point along its propagation path (at the surface). Single-sided access has been considered but has not proved to be a feasible technique for measuring SHG. Although previous work has reported [43,44] successful results using single-sided SHG in solid and fluids. However, when the propagating waves reflect off the back-wall towards the transducers SHG is induced on its backwards propagation path which is out of phase with the SHG induced on the forward propagation path. This results in destructive interference between the two propagation paths, removing the energy which has been transferred to the second harmonic. In reality, there is some energy at the second harmonic due to a difference in diffraction and attenuation between the two paths, but this is still very small and challenging to measure compared with a through transmission measurement (i.e. two sided configuration).

The general experimental procedure for measuring second harmonic generation is achieved by implementing two monolithic probes (e.g. transmitting at 5 MHz and receiving at 5-10

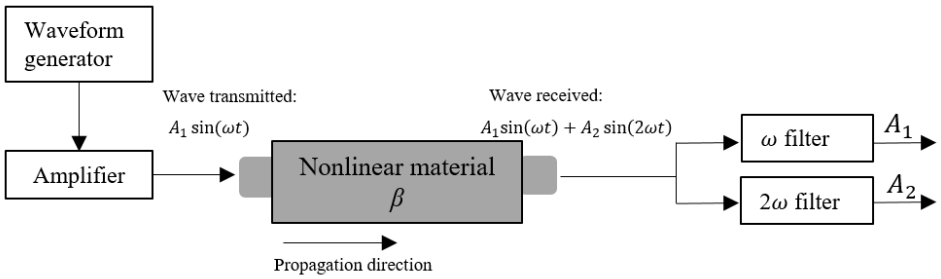

FIGURE 2.4: Schematic of monolithic nonlinear experiment configuration.

MHz). The schematic for this set-up is shown in Fig. 2.4. A pulse wave of frequency ω is transmitted at one side of the material and is received by a secondary monolithic probe on the opposite side of the specimen. The in-contact coupling allows for efficient transmission of the ultrasonic signal. The signal length is generally more than 10 cycles and captured using a broad-band receiver to ensure all nonlinear components are measured. In addition, a powerful amplifier is required during the implementation of SHG due to the weak harmonic amplitude relative to the incident amplitude. When the signals are received by the broadband transducer a number of processing techniques are applied to extract the desired information. The amplitude of the received signals is filtered at both the fundamental frequency (ω) and the second harmonic (2ω) to determine A_1 and A_2 respectively. Using this measurement it is then possible to infer the value β using Eq. 2.14. In practise, a more accurate measurement of β is achieved by repeating the measurement for a wide range of transmission voltages. Therefore, through multiple measurements of A_2^2 at different excitation amplitudes (i.e. A_1), the relationship between A_2^2 and A_1 can be calculated by fitting a linear line through the data points. The gradient of this line can then be used determine β.

Previous work suggests that a quantitative measurement of early stages of degradation (fatigue and creep) using SHG is achievable in a range of materials including aluminium [23], nickel super alloys [45], carbon steels [46] and titanium [47]. The general trends in these studies show that β increases with number of fatigue cycles, and therefore if measured quantitatively,

provides a deterministic measure of fatigue life. However, this monotonic relationship is true for most studies, but is not universal. Previous works have shown than an increase in fatigue results in a reduced β value. For example, two distinct peaks in β have been observed towards later stages of fatigue life in aluminium [48] when subject to low cycle fatigue. A similar effect has been observed in steel. Therefore it is important that trends of β with respect to fatigue life should be considered for each specific material and loading conditions. Another limitation of SHG is that it is not possible to distinguish between non-classical and bulk material nonlinearity along the propagation path, as well as instrument nonlinearity. The nonlinearity induced by the coupling applications can also have a significant effect on the results. In addition, varying attenuation and diffraction for the fundamental and second harmonics requires effective post-processing corrections [49, 50].

2.2.2 Wave mixing method

When two-incident waves mix together, material nonlinearity induces a nonlinear interaction between the two ultrasonic waves. The study and analysis of this interaction is called the Wave Mixing method, and consists of two classes: collinear and non-collinear mixing [51, 52]. Under particular conditions the two incident waves (assuming quadric nonlinearity at the point of intersection) will interact and generate a third wave, which has a frequency and wave vector equal to the sum and difference frequency of the two incident wave frequencies and their wave vectors. The two key advantages of this technique over SHG are that the nonlinearity parameter inferred through wave mixing is localised at the point of the waves intersecting, and the instrument and material nonlinearity may be separated since β is inferred by analysis of the generated wave. In the case where the generated wave is at the difference frequency, the attenuation it will experience will be significantly lower than the transmission and harmonic frequencies, meaning the wave is less susceptible to attenuation and therefore more nonlinear

information can be captured by the probes. The focus of this section will be a non-collinear interaction, providing a specific example of how wave mixing works.

In NDT the non-collinear technique is desirable as it only requires single-sided access. When implementing the non-collinear method the interactions between the waves do not have parallel vectors but are instead of some relative angle to their propagation directions. Quadratic nonlinearity at the point of intersection leads to the generation of the third wave. The scattered wave will have a direction vector which is equal to the sum or difference of the incident wave vectors ($k_3 = k_1 + k_2$ or $k_3 = k_1 - k_2$). The frequency of this generated wave will be equal to the sum or difference of the incident wave frequencies ($\omega_3 = \omega_1 + \omega_2$ or $\omega_3 = \omega_1 - \omega_2$). The theoretical solutions were first introduced by Jones and Kobett [53] and Taylor and Rollins [51]. The case that has mostly been applied to NDT is the interaction of shear waves to produce a longitudinal wave at the sum of the incident frequencies ($T(\omega_1) - T(\omega_2) \rightarrow L(\omega_1 + \omega_2)$). In order to produce a large amplitude longitudinal wave in the direction of the resulting wave vector ($k_1 + k_2$), the interaction angle of the incident frequencies ϕ and the ratio of the incident frequencies $\alpha_\omega = \omega_1/\omega_2$ must satisfy the following resonant condition,

$$\cos\phi = \alpha_\omega^2 + \frac{1}{2}(q + \frac{1}{q})(\alpha_\omega^2 - 1) \tag{2.17}$$

where q is the ratio of longitudinal and shear velocities. This condition can be satisfied for an number of relative angles, therefore the frequency ratio is not limited. However, there is a frequency ratio limit to Eq.2.17, where the frequency ratios must be between $(1-q)/(1+q)$ and $(1+q)/(1-q)$.

This methodology can be conducted using a double-sided configuration, see Fig. 2.5(a). Two monolithic transducers are coupled via a wedge to transmit shear waves at an angle into the material. The angle of the wedges are selected such that the refracted shear waves are

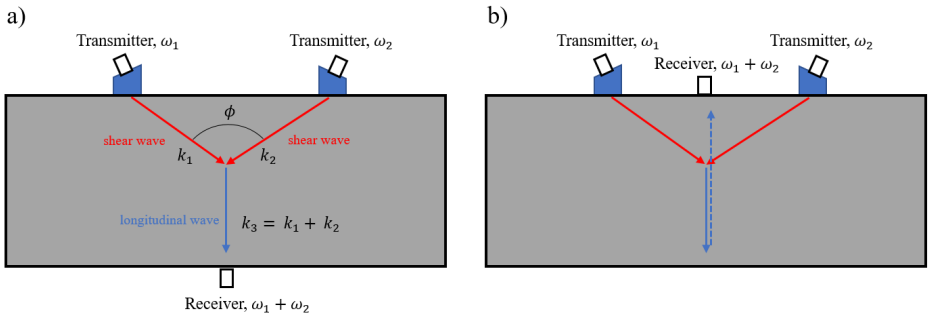

FIGURE 2.5: Schematic of a typical non-collinear wave mixing experimental setup: (a) double-sided and (b) single-sided

transmitted and interact at the chosen relative angle α_ω. The depth of the interaction can be modified by changing the distance between the transmitting probes. For a frequency ratio of 1 (i.e. the $\omega_1 = \omega_2$), the generated longitudinal wave propagates through the medium normal to the surface to be received on the opposite surface of the material.

Single-sided access of this experiment is also achievable and shown in Fig. 2.5(b). For this symmetric arrangement, the generated longitudinal wave scatters at normal to the surface (back-wall). This reflected wave will then be the first reflection received by the transducer position centrally on the transmission surface. If the frequency ratio is not equal to unity, than the generated wave will be steered away from the centre point (centre distance between transmitters). For this configuration, it is possible to scan through the depth of the material by altering the separation of the transducers. This is also achievable by changing the angle of the transducers, however requires the frequency ratio to be changed in order to ensure the resonance condition is satisfied.

The first experimental study to assess the feasibility of non-collinear mixing for damage characterisation was published by Croxford et al. [24]. This study conducted a $T(\omega_1) - T(\omega_2) \rightarrow L(\omega_1 + \omega_2)$ interaction to samples of Al-2014 for monitoring residual stress and low-cycle fatigue. Additional recent publications have experimentally validated this technique for detecting classical nonlinearities [54] as well as non-classical nonlinearities [55, 56]. In summary, the

wave mixing method can resolve elastic nonlinearity at the interaction volume meaning it is possible to measure nonlinearity locally at various locations in a material. By altering the configuration between the transmission traducers it is possible to take measurements locally throughout the material to determine a map of nonlinearity. This provides a significant advantage over SHG which can only determine the integral of nonlinearity along the propagation path. The spatial separation of the generated wave means it is possible to differentiate between instrument and material nonlinearity. The limitation of the wave mixing methods is the experimental configuration which is significantly more complicated than other nonlinear techniques, meaning this method is impractical for *in-situ* testing and monitoring, and therefore is currently limited to lab research.

2.2.3 Nonlinear elastic wave spectroscopy

Nonlinear elastic wave spectroscopy (NEWS) studies the interaction of a wave with its medium by analysing its frequency spectra. In a way all non-linear techniques are implemented by analysing frequency spectra, but this technique is focused on measuring the frequency spectra of a system in response to resonant excitation, as opposed to a single frequency. Using this technique it is possible to infer the elastic nonlinearity at a point in the material, rather than the later component of the propagating wave.

The class of techniques used to measure the global nonlinear response of a material are known as nonlinear resonant ultrasound spectroscopy (NRUS) methods. In a linear material or system, the structure has set natural frequencies and modes which are independent of excitation amplitude. In a nonlinear system, the modal frequency response is a function of the excitation amplitude. One type of these NRUS techniques introduced by Abeele et al. [1] is called nonlinear wave modulation spectroscopy (NWMS), a method which focuses on the application of harmonics and sum and difference frequencies in a material affected by damage.

This provides a measure of the global nonlinearity in the material. The material is excited using two continuous waves at different frequencies simultaneously, whilst inspecting the harmonics of the two waves and their sum and difference. In a linear material or undamaged specimen it is expected that the output spectrum will consist of two frequencies (the two input excitation frequencies) that have been slightly altered by wave dissipation and scattering (linear processes), and negligible nonlinearity. In a damaged material, harmonics and side bands are created by the nonlinearity within the material which is induced by micro-cracking and fatigue. The efficacy of this technique was tested on two plates, an un-damaged sample and a damaged sample containing numerous micro-cracks. The samples were excited using a sweep frequency (around the first natural frequency), measuring the peak amplitude displacements [1]. The results for this are presented in Fig. 2.6. The undamaged specimen only shows a change in the magnitude of the frequency response, while the damaged specimen shows a change in magnitude and frequency with an increasing excitation amplitude.

A further study by Courtney et al. [57] shows consistent results analysing the bi-spectrum of the signals transmitted into a fatigued aluminium sample. The difference in signals at the transmission bandwidth was shown to increase in the presence of damage and has proven to be robust to transducer position, boundary conditions and vibrational amplitudes. This study in particular concluded that consistent results are achieved when using multiple excitation modes in the experiment. This would remove the possibility that a particular mode has a node positioned at the defect, increasing the accuracy of this method.

The nonlinear resonant technique has also been effective in detecting fatigue in composite materials [58,59]. NEWS was able to detect the presence of damage in the structure, even when the damaged region only covered a small area. Meaning it has the potential to determine early stages of fatigue in composites. Alternatively, by investigating the harmonic and side-bands (using NRUS methodology) it is possible to determine not only the presence of damage but

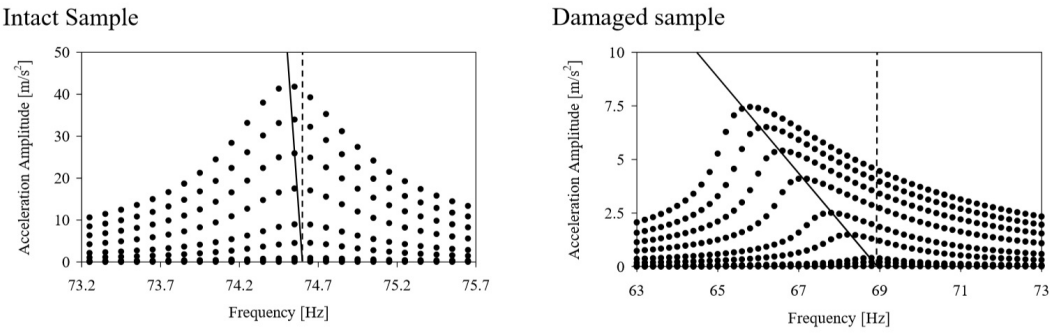

FIGURE 2.6: Example of nonlinear resonant spectroscopy (Image reproduced from [1]).

the severity.

The NRUS method was adapted further by Solodov et al. [2] using a laser vibro-meter to achieve localised measurements of the spectra and form images using the nonlinear information. For this study a high amplitude ultrasonic signal is transmitted into the material and the subsequent field is measured at locations on the surface by the laser vibro-meter. The efficacy of this technique was tested by growing a fatigue crack in an aluminium test sample. Analysis of the frequency spectra showed amplitudes of sub-harmonic components around the fatigue crack, but also self-modulation (the mixing of frequencies within the transmission bandwidth). Self-modulation results in an energy flux from the transmission band-width down to very low frequencies due to sum-difference frequency modulation. In Fig. 2.7(a) spectral results are plotted against excitation amplitudes, displaying the sub-harmonic content and self-modulation measured at the location of the fatigue crack.

A nonlinear image was then formed by extracting the frequency components of various surface locations by conducting a C-scan of the material. The sub-harmonic image from this scan is presented in Fig. 2.7(b). The resulting image clearly indicates the location of the fatigue crack. However, a limitation of this technique is that it is not possible to make through depth measurements of elastic nonlinearity but only surface measurements.

Another class of the NEWS methods is time-reversal nonlinear elastic wave spectroscopy

a) b)

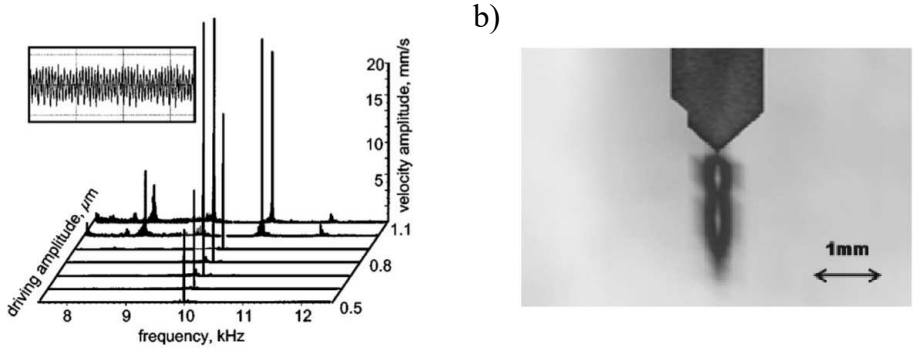

FIGURE 2.7: (a) Experimental spectral response of fatigue cracks using a 20 kHz excitation (b) Image generated from sub-harmonic data captured from C-scan (Image reproduced from [2]).

(TR-NEWS), which was first developed by Ulrich et al. [60]. This method exploits the reciprocity of a linear system. For example, consider two incident waves propagating at different frequencies in a damaged material, that are simultaneously co-incident at the location of the damage. The sum and difference frequencies induced by the nonlinearity from the damage will propagate into the field from that point (i.e. the damage location) to be received by a network of transducers. The received signals are then filtered at the sum and difference frequencies, time-reversed (reversing the order of the data points in the time domain) and re-broadcast. It is expected that the re-broadcast signals will focus on the nonlinear scatterer in sequence. Experimental results showed that the re-broadcast signal did focus at the fatigue crack by measuring surface displacement using a laser vibro-meter.

In summary, nonlinear spectroscopy techniques are capable of inferring elastic nonlinearity in materials through analysis of the spectra, both globally and locally. The localised measurements however, requires an extensive complex experimental set-up and procedure to scan samples. In addition, the application of this technique to large samples can potentially be very time consuming. The ability to infer elastic nonlinearity at various harmonics in the spectra is beneficial and offers the ability to resolve either classical, non-classical or both. In particular, the generation of a low frequency component caused by nonlinear mixing in the frequency band-width offers efficient detectability. Attenuation at low frequencies is relatively

lower compared with the transmission band-width, meaning a higher amplitude wave can be measured. Since nonlinearity induced by the materials can be significantly damped by attenuation this is very beneficial. The limitation of this method is that nonlinear measurements can only be conducted on the surface of the specimen, which prohibits industrial application where through depth analysis of elastic nonlinearity is required.

2.2.4 Nonlinear phased array techniques

2.2.4.1 Ultrasonic phased arrays

An ultrasonic phased array is a device comprising of multiple piezoelectric elements for transmitting and receiving ultrasonic signals. Conventionally, this is achieved through parallel transmission circuits that allow for transmission of ultrasonic plane beams, steered angled beams and focused beams by applying delays to the signal [37, 61]. All of these benefits allow for increased sensitivity and detection of features inside materials. Prior to phased arrays, monolithic traducers would be exclusively used for inspections. There are two main benefits from implementing a phased array over monolithic transducers, the first being a reduced inspection time as mechanical scans are not required for a significant volume (based on the size and sensitivity of the array). Secondly, it is possible to implement the various beam forming approaches mentioned via programming delays to the parallel output circuits.

The application of phased array configurations was initially in medical imaging for diagnostics purposes [62] and has been proven effective for NDT in engineering and aerospace industries [37, 63]. The most significant difference in ultrasonics between these two fields is that the inspection subject in engineering applications is typically static (i.e. time invariant), where in medical imaging the subject is time variant and therefore needs to be evaluated frequently per second (hence the optimisation of medical imaging is generally focused on frame

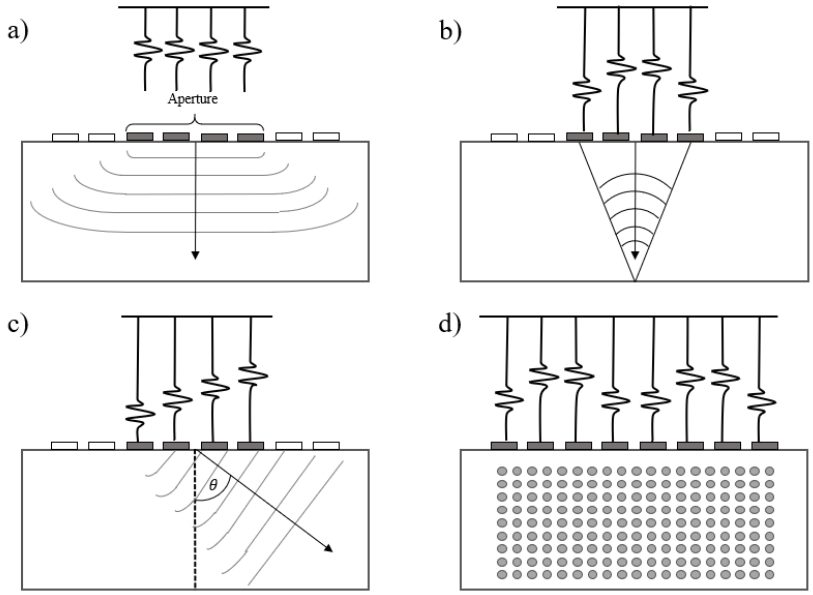

FIGURE 2.8: Schematic illustrations of (a) plane B-scan, (b) focused B-scan, (c) sector B-scan and (d) total focusing method.

rate). The medical transmission modes are grouped into the following three methods: plane B-scan, focused B-scan and sector B-scan (a schematic diagram of these methods are presented in Fig. 2.8(a-c)).

In engineering based NDT generally the specimen does not change at all over the period of the experiment, therefore more accurate processing tools can be used to detect features in materials (since the experiment is not constrained to high frame rate performance). It is possible to capture and store the time-domain signals and reprocess the data afterwards. This technique is known as full matrix capture (FMC) where the array transmits on each element in sequence whilst all elements are receiving and the time series data is stored in a matrix [63]. It has been proven that the equivalent plane B-scans, focused B-scans and sector B-scans can be formulated by extracting the corresponding time-domain signals from FMC data. The most critical technique for increased accuracy is the total focusing method (TFM), which provides a very high signal-to-noise ratio (SNR) and spatial resolution by synthetically focusing at each pixel point with all elements in post-processing [63].

The TFM method is implemented by firstly defining a x-z target grid space which is going to be imaged. Assuming the time series data is represented as $f_{j,k}(t)$ for all j transmitted signals and k received signals. All of the received FMC data is then synthesised to the image space to give the intensity $I(x,z)$ by the following equation,

$$I(x,z) = \left| \sum h_{j,k} \left(\frac{\sqrt{(x_j - x)^2 + z^2}) + \sqrt{(x_k - x)^2 + z^2})}{c_l} \right) \right| \tag{2.18}$$

for all j, k combinations. Where $h_{j,k}$ is the Hilbert transform for each transmitter and receiver pair, x_j and x_k are the co-ordinates of the centre of the elements and c_l is the longitudinal speed of sound in the material. The summation is used for all j and k combinations, meaning every sequential firing contributes to the formation of this image and thus using as much information as possible. Prior to this calculation, linear interpolation of the time domain signals is necessary to allow for the computation of the spatially dependent $I(x,z)$.

Nonlinear measurement techniques adapted to a phased array configuration offer huge potential for localised measurements of nonlinearity. The implementation of phased arrays to nonlinear methods will be discussed in the following sections. The techniques will be introduced in two main categories: coherent and diffuse methods.

2.2.4.2 Coherent field nonlinear imaging

In the case where a nonlinear feature exhibits reflections from its boundary (or is in close proximity to a reflector), the nonlinearity of the scattering feature can be determined using the coherent field (i.e. the coherent back scatter). These reflections allow nonlinear information to propagate back to the ultrasonic transducer. Capturing nonlinear information during the coherent field means the SNR of the received signals is high and the resolution of nonlinearity

is elevated.

The earliest nonlinear coherent technique was implemented for detecting nonlinear scattering from micro-bubble contrast agents in the presence of tissue [64]. This technique implements a modified Doppler and colour Doppler pulse sequence by inverting every second pulse signal and subtracting them. The method suppresses the linear scattering from the subject (the micro-bubble) subsequently revealing the nonlinear scattering in the frequency spectra. Another well researched technique is the amplitude modulation technique (AM) which excites the wave field at two amplitudes. The relative harmonic amplitudes between the two fields gives a measure of nonlinearity. The difference in harmonic amplitude is caused by the varying input amplitude and has been proven a robust measure of nonlinearity [65].

Nonlinear coherent methods since then have been adapted to phased arrays to spatially resolve relative amplitude difference induced by fatigue cracks in metals. The fundamental wave amplitude difference (FAD) method has been proven to detect contact acoustic effects in fatigue cracks [3] by measuring the energy lost at the fundamental frequency. Since all forms of nonlinearity (i.e. classical and non-classical) result in energy being transferred away from the harmonic, therefore it is possible to measure all nonlinear contributions at a focal point by evaluating the energy lost at the fundamental frequency. Assessing the energy lost at the fundamental to nonlinear harmonics provides higher selectivity to detecting fatigue cracks over measuring sub-harmonic and super-harmonic component of the spectrum. However, measuring energy lost from the fundamental removes the ability to separate the types of nonlinear fatigue (i.e. contact-acoustic or material nonlinearity), since the measurement is the total loss of energy from the fundamental to different nonlinear components, and not the measurement of individual nonlinear spectral components. This technique was validated using a 32 element 5 MHz array, the lower and higher amplitude images are presented in Fig. 2.9(a-b), and the subtracted image is present in Fig. 2.9(c). The low and high amplitude images

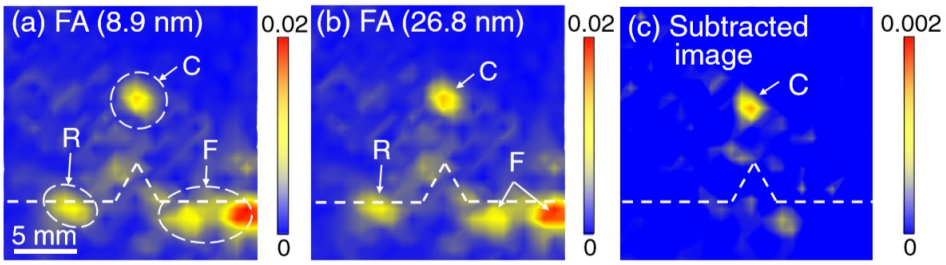

FIGURE 2.9: FAD used to detect a closed fatigue crack: (a) lower input amplitude, (c) higher input amplitude and (c) difference (images reproduced from Ikeuchi et al. [3]).

indicate that the fatigue crack exhibits significant linear scattering relative to the back wall, as well as coherent noise exhibited throughout the image domain. The subtracted image in Fig. 2.9 (c) suppresses the linear scattering from the crack tip and the back wall, and only the nonlinear residual remains, resulting in a clear spatial resolution of the nonlinear feature and a measurable sensitivity. In addition, the coherent noise from the low and high amplitude images in Fig. 2.9 (a-b) have been suppressed reasonably well.

Another form of FAD has been introduced by Haupert et al. [28] which consists of three modes of parallel transmission: only odd elements, only even elements, and all elements firing. The variation of energy transmitted to each focal point between odd and even compared to all firing results in a localised amplitude difference. The all elements firing transmission physically focuses within the medium at multiple focal points by applying delays on transmission and reception producing a linear image. The odd and even mode repeats this focusing process but only the odd or even elements are active. These images are then added together and subtracted from the all element firing transmission, resulting in the generation of a nonlinear image.

A demonstration of feasibility was conducted by Haupert et al. [28] on a stainless steel AISI304 sample subjected to thermal fatigue loading to create a thermal fatigue crack with a residual stress field. The technique was implemented using a 5 MHz 64 element array with an inter-element pitch of 0.42 mm, contact coupled to the surface opposite the fatigue crack. The conventional imaging is capable of detecting the linear scattering from the feature,

approximately 8 dB above the coherent noise. Coherent noise (e.g. grain noise) was also measured in the results, and is sparsely distributed throughout the image. The corresponding nonlinear image has suppressed the coherent noise and the linear scattering from the defect, resulting in an increased sensitivity to the defect of 25 dB.

A sequential-parallel subtraction technique has also been implemented by Cheng et al. [27], which relies on two modes of transmission: parallel and sequential. In parallel mode the elements fire the signals at once and delay laws are applied to each element to focus at points in the material. In sequential mode the elements transmit the signals individually and each time-domain signal for each transmit and receiver pair is stored in a full matrix capture (FMC), the same delay laws are then applied in post-processing to synthetically focus at pixel locations. The main difference between the modes of transmission, is that during sequential transmission the elements are fired individually, and the high intensity focus is not generated in the sample but in post-processing. Assuming the principle of linear superposition holds for both the parallel and sequential fields, the two transmission modes have nearly identical linear propagation. Therefore, the two resulting images would be linearly equivalent and any differences in amplitude would be attributed to nonlinearity at the focal point. This difference can be exploited to determine the elastic nonlinearity at the focal point. The technique has been validated for detecting closed crack tips at varying stages of early development against micro-graphic images of the fatigue.

The coherent methods previously described evaluate elastic nonlinearity at the focal point through analysis of energy lost from the fundamental. A coherent technique for imaging closed cracks at the sub-harmonic frequency was first developed by Ohara et al. [4]. This technique implemented both a monolithic transducer and a phased array for transmission and reception respectively, as seen in the configuration in Fig. 2.10 (a). The monolithic transmitter is translated across the surface and the received signals produced into images by correcting

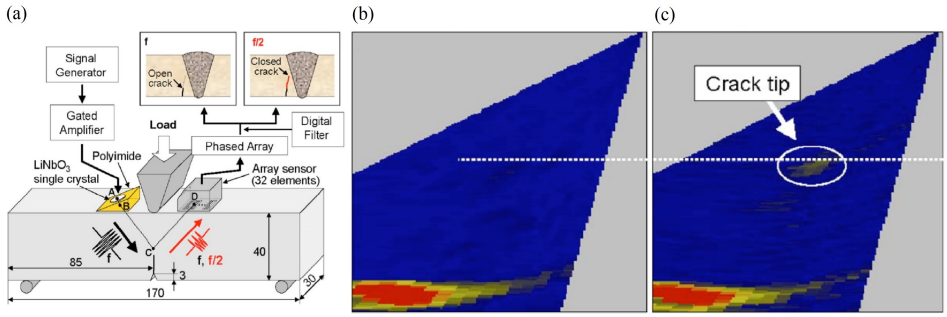

FIGURE 2.10: Sub-harmonic imaging monolithic and phased array configuration and imaging results: (a) configuration, (b) fundamental frequency and (c) sub-harmonic frequency (results reproduced from Ohara et al. [4]).

for the various propagation paths and then integrating the signals received from each element in the array. The signals are then band-pass filtered at the fundamental frequency and the sub-harmonic frequency to produce corresponding images. The performance of this apparatus was assessed using a three-point bend (3PB) test fatigue sample made from stainless steel, using 7 MHz monolithic transducer and a 5 MHz 32 element phased array.

The study investigates the fundamental and sub-harmonic response from a close crack tip under various stress intensities. When under a low stress intensity compared with a high stress intensity, the sub-harmonic is sensitive to detecting the fatigue crack (see Fig. 2.10(b)), whilst the fundamental is not able to resolve the feature (see Fig. 2.10(c)). This indicates that the crack tip is partially closed, and therefore the sub-harmonic (induced by contact-acoustic and frictional nonlinearity) is more detectable during low stress stages of fatigue and/or early stages of fatigue. However, in the results for the high stress intensity, the fundamental is more sensitive to the crack tip than the sub-harmonic. Overall both methods have been effective in detecting the nonlinearity induced by the fatigue crack.

The main benefits of coherent methods is the capture of ultrasonic data with a high signal-to-noise ratio (SNR) meaning coherent and random noise levels have low influence in the constructed nonlinear image. Therefore the detectability of the feature is generally high and is more robust in detecting sources of non-classical nonlinearity. Since nonlinear signals are

captured in the coherent field more nonlinear information can be analysed to determine the location of the feature. This results in a higher resolution of the nonlinear feature above the noise floor. The dependency on linear scattering limits coherent techniques to non-classical nonlinearity since classical linearity generally does not produce reflections.

2.2.4.3 Diffuse field nonlinear imaging

The phased array methods described in the previous section are principally dependent on scattering from the nonlinear feature to measure a field at the sub-harmonic and fundamental frequencies. Theoretically, these methods only measure a small proportion of nonlinearity induced when the wave-field is incident since reflected nonlinear energy will propagate in various directions throughout the material. In particular, if a micro-crack is closed only the forward propagating field through the material contains the nonlinear information and would require a receiving array on the opposite surface. In addition, the orientation of the crack tip can limit the coherently scattered field, meaning limited nonlinear information is received by the array. To improve detectability a nonlinear ultrasonic diffuse energy imaging (NUI) technique was proposed to overcome these challenges [5]. This method is advantageous since it allows for the total nonlinear information (scattered in all directions) to be evaluated from a fully diffuse field.

The NUI technique utilises the physical difference between sequential and parallel transmission, first proposed by Potter et al. [5]. It is worth noting that the coherent method used by Cheng et al. [27] mention in the previous section implements the same transmission configuration. In parallel transmission, the ultrasonic signals are fired near simultaneously using an applied delay law, to produce a high intensity focus at a point in the material. During sequential transmission the signals are fired independently (known as a FMC) while all elements are receiving and the interference effects are applied in post-processing by synthetically focusing

with the delay laws. The linear propagation between the two fields is identical, therefore any difference between the two fields can be attributed to nonlinearity (i.e. elastic nonlinearity at the focal point), since the presence of nonlinearity will result in varying propagation between the two fields.

In the parallel case (where all elements are firing) the material experiences more stress at the focal point than contributions from the individual sequential transmissions. The nonlinearity is determined by the flux of energy away from the fundamental, therefore it is expected more energy will be lost in the parallel case. For example, consider the case of longitudinal wave propagation through an elastic solid with isotropic bulk nonlinearity truncated to the second order. For the parallel and sequentially focused fields using a phased array with N number of elements, the wave amplitude A at the focal point differs by a factor of N. The amplitude of the second harmonic generated is proportional to A^2, and the energy of the second harmonic is proportional to A^4, hence the energy lost from the fundamental is proportional to A^4. The ultrasonic energy lost from the fundamental in the parallel focusing is therefore N^3 higher than the energy lost from the summation of N transmission cycles in the sequential case (see table 2.1 for more detail) [5]. Since phased arrays are of the order $N = 100$, the difference in energy lost between the two fields is significant. This measure of difference in energy between the two fields infers nonlinearity at the focal point in the subsequent diffuse field.

Transmission mode	**Amplitude of fundamental**	**Amplitude of second harmonic**	**Energy lost from fundamental**
Parallel	NxA	$(N$x$A)^2$	$(N$x$A)^4$
Sequential	NxA	NxA^2	NxA^4

TABLE 2.1: Amplitude at the fundamental, amplitude at the second harmonic and energy lost from the fundamental at the focal point for a single transmission cycle.

Measurement of the total nonlinear energy in the system is not feasible in the coherently scattered field, however it is possible in the subsequent diffuse field later in time. After the initial transmission and multiple scattering (from boundaries) the ultrasonic energy will

homogenise in the structure. In this state the ultrasonic energy is statistically diffuse in the structure and the energy measured at any point in the material is proportional to the total energy in the system. During this time the energy lost from the fundamental at the focal point is spread uniformly throughout the structure, and the relative diffuse energy of the parallel and sequential field is proportional to the relative energy loss at the focal point. Therefore, ultrasonic nonlinearity at the focal point can be estimated by measuring the relative diffuse energy loss at the fundamental between the parallel and sequentially focused fields. This is the principle of NUI, the metric is therefore defined as the normalised difference in diffuse energy between the sequential and parallel fields.

The technique was implemented by Potter et al. [5] on artificially produced fatigue crack samples to assess efficacy. Since the crack tips are expected to behave nonlinearly, these fatigue samples provide a clear point of nonlinearity in the material to detect. The fatigue crack in this case has been drilled to produce linear reflectors to emulate a surface breaking crack and clearly indicate the benefit of nonlinear imaging in aiding linear imaging. The nonlinear and linear (TFM) results using a 5 MHz 64 element phased array are presented in Fig. 2.11. As seen in Fig. 2.11(b) the image is dominated by linear scattering from the drill hole and the back-wall. There is some linear scattering observed at the location of the crack tip, however this is a very subtle feature and does not provide any indication of nonlinearity and size. The nonlinear image presented in Fig. 2.11(a) shows clear isolation and detection of the crack tip due to local elastic nonlinearity. Moreover, the linear suppression in this technique is particularly effective, which is a consequence of NUI. Since the nonlinearity is not derived from the coherently scattered field at the focal point, the instrument and material nonlinearity is consistent between the two firing methods and therefore does not produce artefacts from linear features (which is the case with coherent methods discussed in Section 2.2.4.2). This effective suppression of linear features is crucial since the crack tip is emerging from the drill-hole in the sample, and therefore without effective separation of linear and nonlinear features, a small

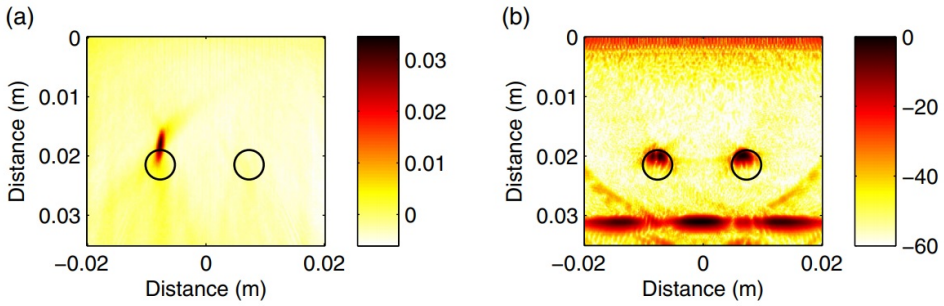

FIGURE 2.11: Nonlinear diffuse field phased array results: (a) Nonlinear metric γ and (b) linear method (TFM) (results reproduced from Potter et al. [5]).
1

nonlinear defect will be masked by the strong linear features.

The technique has also been validated for the monitoring of the early stages of fatigue crack growth [6]. The method was tested on steel compact tension (CT) specimens subject to various loading cycles. The detection of the nonlinear features is validated against micro-graphic images. This study investigated the sizing of crack tips for loading cycles between 40,000 and 100,000 cycles (presented in Fig. 2.12(a)-(c)), and shows the maximum magnitude of the nonlinear metric increases almost linearly with crack growth. In addition, the position of peak nonlinear amplitude and the actual crack tip location as measured from micro-graphs is investigated. The image location of the crack tip is below the location of the actual crack tip by approximately 1 mm, as seen in Fig. 2.12(c). This is not necessarily caused by the location of maximum nonlinear response. Less of the crack lies under the footprint of the focal region when focused at the crack, therefore reducing the measured nonlinear response. Despite this off-set, the locations of the peak nonlinear amplitude in the images are consistent with the actual crack tip location measured from surface micro-graphs. The study concludes that the NUI method is capable of imaging micro-scale fatigue cracks down to 15 % of fatigue life. It is worth noting that the percentage of fatigue life in this study is measured as the number of loading cycles (at various experimental stages) divided by number of loading cycles at failure. The diffuse state of the material is what provides the sensitivity to the NUI method, placing

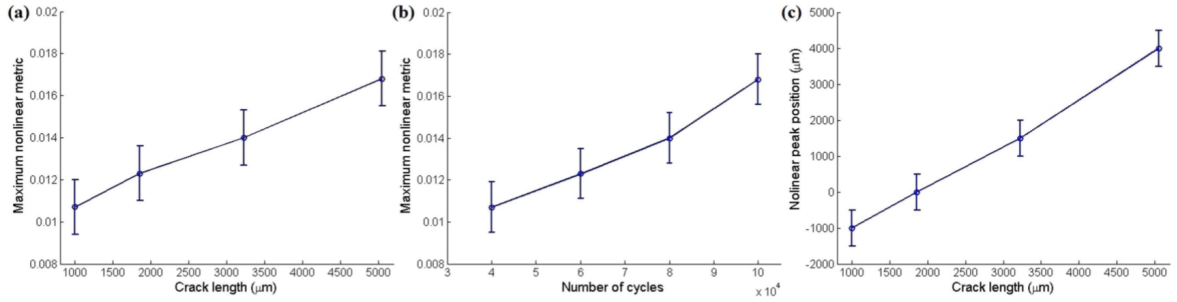

[H]

FIGURE 2.12: Maximum nonlinear diffuse metric during fatigue as a function (a) actual crack length and (b) number of fatigue cycles. (c) the measured crack length from the diffuse image as a function of the micrographically measured crack length (results reproduced from Cheng et al. [6]).

limits on practical applications. The current results for NUI have been obtained on relatively small test specimens in a laboratory environment, therefore this method has only been proven effective in ideally diffuse conditions. The method is yet to be evaluated on larger volumetric samples which reflect those used in industry.

In summary, NUI offers the ability to spatially resolve fatigue cracks without the presence of strong linear back-scatter. This means the technique can be implemented when the orientation of the fatigue crack is unknown and more importantly, has the potential to resolve classical nonlinearity (induced by lattice anharmonicity and dislocations). It also provides the ability to capture more nonlinear information which propagates throughout the structure. However, the limitation of this method is the dependency on the diffuse field and therefore efficacy on relatively larger samples is unknown.

2.2.5 Summary of nonlinear methods

A broad range of nonlinear methods for measuring elastic nonlinearity have been introduced. Each method has particular experimental requirements, set-ups and sensitivity to different types of nonlinear damage. By comparison with linear imaging, these methods are capable of characterising micro-structural fatigue prior to the formation of larger volumetric damage,

meaning it is possible to detect defects earlier.

Nonlinear phased array methods are advantageous over other more complicated nonlinear experimental set-ups. In particular, a measure of localised nonlinearity can be determined in a specimen (without the requirement for mechanical scanning) which is not possible using monolithic probes, in turn reducing experimental run time. Phased array techniques also facilitate through depth nonlinear analysis and are not limited to surface measurements. A summary of advantages and disadvantages of the various nonlinear phased array methods are presented in Tab. 2.2. The coherent phased array methods are shown to be effective in imaging nonlinear features by measuring nonlinearity in the coherent backscatter. These methods are limited to fatigue scattering linear reflections, therefore in the case of fatigue crack tips the orientation can effect the efficacy of the techniques. In real-life samples the orientation of crack tips is unknown and therefore presents a limitation to the coherent method. Moreover, the coherent methods only measure nonlinear information which back-propagates to the array and ignores the nonlinear information which scatters in all directions in the material. The NUI method addresses these limitations by measuring the total nonlinear information in the subsequent diffuse field which does not rely on direct coherent scattering. The NUI method is therefore capable of measuring bulk material nonlinearity (classical) which does not produce linear reflections to be measured. Given the clear advantages over the coherent method it is evident that the NUI method should be further researched as it has the most potential for industrial application.

Nonlinear phased array techniques	**Damage sensitivity**	**Advantages**	**Disadvantages**
Sub-harmonic (Coherent)	Partially closed crack.	Through depth imaging. Single-side access.	Dependent on linear scattering near the feature (crack orientation dependency). Multiple transducers required. Analysis limits nonlinear information.
FAD (Coherent)	Partially closed crack.	Through depth imaging. Single-side access. Single array required.	Dependent on linear scattering near the feature (crack orientation dependency).
Seq-par (Coherent)	Partially closed or closed crack.	Most sensitive imaging metric. Through depth imaging. Effective linear suppression.	Dependent on linear scattering near the feature (crack orientation dependency).
Seq-par (Diffuse)	Partially closed or closed crack. Has potential to resolve bulk nonlinearity.	Through depth imaging. Effective linear suppression. Not dependent on linear reflection (crack tip orientation independent).	Requires a measurable diffuse field (limits volume size).

TABLE 2.2: Advantages and disadvantages of nonlinear phased array techniques.

2.3 Research scope

This thesis will focus on optimising NUI given its applicability to resolving non-classical features (fatigue crack tips) without the requirement of scattering from the nonlinear feature and the potential for resolving classical features (dislocations and anharmonicity). The current weakness of NUI will be addressed while incorporating the strengths of wave mixing and nonlinear spectroscopy methods. The study will focus on the following five aspects of NUI:

1. The NUI method has proven to be effective in detecting fatigue crack tips, however, further investigation into detectability of nonlinear features using various transmission frequencies is required to ensure maximum sensitivity to low level nonlinear responses. In this thesis various transmitting frequencies will be evaluated using simulated and

experimental sensitivity maps. In addition, a multi-view NUI method is proposed to increase the detectability of features.

2. As indicated in literature, nonlinear features cause energy to be transmitted to a variety of frequency components, such as sum-difference frequencies, second and sub-harmonics. This thesis proposes an adaptation of the current NUI method which evaluates energy at the individual frequency components (as opposed to energy lost from the fundamental), where an increase in sensitivity is expected.

3. The dependency of the diffuse field on the NUI method is fundamental to the detection of features in a material and the general efficacy of this method. Therefore, an investigation into approximating the time a wave-field has homogenised and is diffuse will be conducted. This will increase the sensitivity of the NUI method to resolving relatively lower levels of nonlinearity.

4. An alternative phase method less sensitive dependent on a diffuse field is proposed. The aim of this is to maintain the key benefits of NUI without a significant dependency on the diffuse field, enhancing the method to be more applicable to larger geometries.

5. Using the optimisations proposed in this thesis the efficacy of NUI for resolving bulk material nonlinearity will be evaluated. The focus will be to resolve nonlinear features not currently detectable using nonlinear phased array methods.

Chapter 3

Nonlinear sensitivity analysis

3.1 Introduction

As discussed in Chapter 2, the nonlinear ultrasonic diffuse energy imaging (NUI) technique is capable of detecting closed fatigue cracks in aluminium [5] and mild steel [6]. The key benefit of NUI is the ability to detect nonlinear damage independent of directional scattering amplitude meaning the orientation of the crack tip can be unknown, such as in real fatigued engineering components. Additionally, this method has the potential to resolve bulk material nonlinearity (induced by anharmonicity and dislocations), which does not produce any linear scattering. However, the requirement for a diffuse field means there are limitations with regards to sensitivity. Capturing in a diffuse state means there is less energy available to be measured caused by a reduced signal-to-noise ratio (SNR), which limits the applicability of this method in larger geometries, where reaching a diffuse state is more difficult. In this study, the sensitivity profile of the NUI method will be evaluated to determine the limitations of the method in detecting fatigue crack tips, specifically addressing the issues described. The sensitivity profile will be established using both simulated and experimental data to determine the most appropriate configuration. A range of transmission frequencies will be analysed to

determine the most effective excitation frequency in detecting fatigue as well as analysis of simulated nonlinear sensitivity across two materials: Aluminium 2014 and Mild Steel.

Closed fatigue cracks generally grow from larger volumetric features, however the depth and orientation of the closed crack tip is unknown. Therefore, it may not be possible to directly measure the nonlinear feature using the most sensitive location below the array, since the relative distance between the crack tip and the phased array is not measurable. However, a multi-view method can be implemented by imaging the material after the back-wall reflection, allowing for control over which section of the sensitivity profile is used to detect the fatigue, potentially increasing the detectability of nonlinear features. Prior understanding of the nonlinear sensitivity profile is desired to implement this strategy.

3.2 Diffuse energy method

The theory of NUI proposed by Potter et al. [5] will first be introduced. This will be a full description of the methodology used throughout this thesis and explains the fundamental requirement of capturing in the diffuse field.

As mentioned previously in the literature review, NUI relies on two modes of transmission: sequential and parallel. During parallel transmission the elements fire near simultaneously with an applied delay law to produce a high-intensity focus at a defined location in the material. The sequential mode fires each element individually and the time domain signals for each transmitter-receiver pair are stored in a full matrix capture (FMC) and is synthetically focused in post-processing using the applied delay laws. In both cases where there is the assumption of linear superposition, the linear propagation between the sequential and parallel fields are identical (assuming the specimen is time invariant). However, the presence of elastic nonlinearity causes the two fields to differ, which can be exploited by subtracting the two fields,

suppressing the linear features and isolating the nonlinearity. In the parallel case (where all elements are firing) the material experiences more stress at the focal point than contributions from the individual sequential transmissions. The nonlinearity is determined by the flux of energy away from the fundamental, therefore it is expected more energy will be lost in the parallel case.

The diffuse state is what provides sensitivity to NUI. The method relies on the relative diffuse energy between the two fields being proportional to the relative energy loss at the focal point, which infers the nonlinearity at that point in the material. Therefore requirement to measure diffuse energy between the two transmission modes means the selection of the start gate-time t_r (the time when each element starts to record data) and window length T (length of the time signal each receiver acquires) is critical. The selection of these parameters is a compromise between two competing effects. First, later in time the ultrasonic field convergences to a diffuse field where energy is homogenised. Second, wave propagation is dissipative, therefore the SNR reduces with time. A compromise is selected to ensure the diffuse field condition is achieved whilst the SNR is maximised. An investigation into the selection of these parameters is provided in Chapter 6.

If we assume $f_{j,k}(t)$ is the time-domain signal for each transmit (j) and receive (k) pair for the sequential mode, the transmission delay law $\delta_i^T(r)$ for each jth element to focus at the inspection point $r(x, z)$ and can be expressed as,

$$\delta_j^T(r) = \frac{\sqrt{(x_i - x)^2 + z^2} - \sqrt{(x_a - x)^2 + z^2}}{c_l} \tag{3.1}$$

where c_l denotes the longitudinal wave velocity and x_a is the reference element which is the centre of the x-axis of the delay law. The frequency spectra of $f_{j,k}(t)$ is approximated using a fast Fourier transform (FFT) and is expressed as,

$$F_{j,k}(\omega) = \int_{t_r}^{t_r+T} f_{j,k}(t) e^{-i\omega t} dt \tag{3.2}$$

were t_r is the start gate-time and T is the end gate-time.

The parallel time-domain data is denoted $h_k(r,t)$ for signals received on element k for all focal points r in the material. The frequency spectra of $h_k(r,t)$ is expressed as,

$$H_k(\omega) = \int_{t_r}^{t_r+T} h_k(r,t) e^{-i\omega t} dt. \tag{3.3}$$

The bandwidth integration limits used is an important consideration and are selected in post-processing. A broad-bandwidth will increase the ultrasonic energy incident at the focal point, however this can also cause nonlinear energy flux to harmonics to be within the evaluated bandwidth. Therefore, the bandwidth should be set to the maximum where there is no internal energy flux to harmonics and ensure only the fundamental nonlinear energy loss is considered. Aware of additional nonlinear frequency components such as energy transfers to harmonics, sub-harmonics, sum and difference frequencies, the evaluation bandwidth limits is set as $2/3\omega_0$ and $4/3\omega_0$. Therefore only the energy lost from the fundamental is evaluated in the calculation. Thus the diffuse acoustic energy for an N element array in sequential transmission E_s at focal point $\bar{r}$ is calculated as follows,

$$E_s(r) = \sum_{k=1}^{N} \left(\int_{\frac{2}{3}\omega_0}^{\frac{4}{3}\omega_0} \omega^2 \mid \sum_{j=1}^{N} F_{j,k}(\omega) e^{-i\omega\delta_j^T(\bar{r})} \mid^2 d\omega \right) \tag{3.4}$$

The the parallel transmission E_p, this is calculated as follows,

$$E_p(r) = \sum_{k=1}^{N} \left(\int_{\frac{2}{3}\omega_0}^{\frac{4}{3}\omega_0} \omega^2 \mid H_k(\omega) \mid^2 d\omega \right) \tag{3.5}$$

The nonlinear metric, γ, is calculated as the relative difference in diffuse energy between the parallel and sequential transmission giving,

$$\gamma(r) = \frac{E_s(r) - E_p(r)}{E_s(r)} \tag{3.6}$$

where E_s and E_p is the parallel and sequential diffuse energy. This metric provides a measure of a statistical difference in diffuse energy at the fundamental between the parallel and sequential fields. The procedure for modelling this methodology will be discussed in the next section.

3.3 Simulation sensitivity

To simulate the NUI method outlined in the previous section a quadratic elastic nonlinearity perturbation method has been adopted, whereby the linear and nonlinear fields are simulated separately. This simulation methodology has been adopted in literature for nonlinear imaging in a previous study and will be implemented for this project [66].

The NUI technique operates on the assumption that the sequential and parallel energy loss at the focal point in the coherent field, caused by elastic nonlinearity, is equivalent to that of the diffuse field. Therefore it is only necessary to model the energy of the parallel and sequential fields in the coherent field to model the contribution of elastic nonlinearity, as modelling of the coherent prorogation to the focal point is proportional to the energy transferred in the diffuse field. The simulation will therefore model the flux of energy from the linear to the nonlinear field due to elastic nonlinearity in the coherent field. This energy flux measure provides sufficient analysis of the relative energy lost at the focal point between the two fields, which is proportional to the relative diffuse field energy.

The NUI experiments have been validated for detecting closed crack tips [5, 6]. In these experiments the non-classical nonlinearity will be predominately contributing to the nonlinear energy flux, since classical nonlinearity is a much smaller effect. Since the ultimate aim in the development of this NUI technique is to be able to resolve classical nonlinearity (induced by lattice anharmonicity and dislocations), this simulation will model classical material nonlinearity. A disadvantage of this method is that crack tip nonlinearity (non-classical) does not behave as a point-like nonlinear feature, which will potentially cause discrepancies in analysis, which will be discussed in more detail in this chapter. By assessing the energy flux from the linear to nonlinear field, due to quadratic elastic nonlinearity, at various focal points in the material it is possible to determine the nonlinear sensitivity of this phased array experiment.

The simulation will be conducted using three transmission frequencies: 1, 2.5 and 5 MHz. Each transmission frequency simulation will model two sample materials: Aluminium 2014 and Mild Steel. The selection of samples represent those used in industry and offer varying attenuation rates for analysis. The appropriate attenuation values for each transmission frequency and material will also be implemented to evaluate the influence of attenuation on the sensitivity of this nonlinear method. This is an important parameter to assess for industry since attenuation rates have the potential to limit sensitivity and therefore reduce industrial applicability.

For the perturbation solution of the nonlinear field, the forcing linear simulation will be computed with an analytical solution at each time-step. The linear displacement field will then be used to force the nonlinear field which is computed using a finite difference method. All time stepping calculations were computed in C++/CUDA with extensive use of parallelisation on the GPU. This is important when simulating NUI which requires focusing at each pixel point in the imaging space to establish the nonlinearity at each point, which is a time intensive procedure.

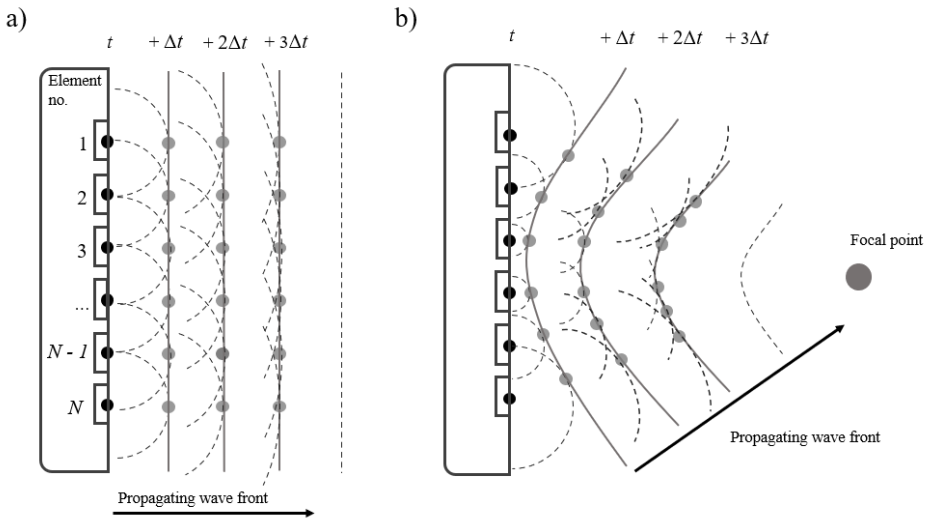

FIGURE 3.1: Illustration of incident field from point sources of a phased array: (a) plane beam and (b) focused beam.

3.3.1 Linear field (Incident)

For modelling nonlinear wave propagation a perturbative approach is implemented by modelling the incident $\bar{u}^{(0)}$ and secondary field $\bar{u}^{(s)}$ components separately. The total displacement field as the sum of the linear incident field and the secondary nonlinear field,

$$\overline{u}(t,\overline{r}) = \overline{u}^{(0)}(t,\overline{r}) + \overline{u}^{(s)}(t,\overline{r}) \tag{3.7}$$

The incident field is simulated using an analytical solution, with each transducer element modelled as a displacement source to simulate the desired propagating wave-front. The sum of these spherical sources determines the wave front. An illustration of the linear wave field model adapted to a phased array is presented in Fig. 3.1(a) for a plane wave where the elements are fired simultaneously. For each time step, Δt, the wave-front is the sum of the spherical sources from the previous time step. For a focused beam it the same principle but with delay laws applied relative to the focal point of the desired beam. This is illustrated in Fig. 3.1(b)

where the delay laws cause the spherical waves to interfere to produce a wave-front focused towards the focal point.

In this study the incident field, $\bar{U}^{(0)}$, is evaluated in the frequency domain from an analytical solution for a focused ultrasonic array and include both longitudinal and shear components of displacement [66],

$$\bar{U}^{(0)} = \Delta(2\pi c_l/\omega_0)^{1/2} T(\omega) \sum_{n=1}^{N} \Bigg[\bar{A}_n(\bar{r}) C_L(\omega) D_{Ln}(\bar{r},\omega) B_n(\bar{r}) e^{i\omega(\frac{|\bar{r}-\bar{a}_n|}{c_l}-\delta_n)} + \bar{A}_n(\bar{r}) C_S(\omega) D_{Sn}(\bar{r},\omega) B_n(\bar{r}) e^{i\omega(\frac{|\bar{r}-\bar{A}_n|}{c_s}-\delta_n)} \Bigg] \quad (3.8)$$

where c_l and c_s are the longitudinal and shear velocities respectively. $T(\omega)$ is the Gaussian spectra in the frequency domain expressed as $T(\omega) = \exp\{-\alpha(\omega-\omega_0)^2\}$ at the centre frequency, ω_0. The beam spread, B_n is expressed $B_n(\bar{r}) = |\bar{r}-a_n|^{-1/2}$. The amplitude unit vector of the longitudinal field component is expressed as $A_n(\bar{r}) = (\bar{r}-a_n)/|\bar{r}-a_n|$.

The directivity of the array is accounted for and describes the angular amplitude distribution of wave modes from the array transducer elements. The directivity is modelled differently for both the longitudinal and the shear components, as the differing displacement directions significantly effects the distribution into the field [67]. The longitudinal directivity function D_{ln} is defined as,

$$D_{Ln}(\theta,\omega) = sinc\left(\frac{\pi\omega b \sin\theta}{c_l}\right) \frac{\left((c_l/c_s)^2 - 2\sin^2\theta\right)\cos\theta}{F_0(\cos\theta)} \quad (3.9)$$

The shear directivity function D_{sn} is defined as,

$$D_{Sn}(\theta,\omega) = sinc\left(\frac{\pi\omega b\sin\theta}{c_s}\right)\left(\frac{c_l}{c_s}\right)^{5/2}\frac{\left((c_l/c_s)^2\sin^2\theta-1\right)^{1/2}\sin 2\theta}{F_0(\frac{c_l}{c_s}\sin(\theta))} \tag{3.10}$$

where θ is the elevation angle and F_0 is expressed as,

$$F_0(\zeta) = \left(2\zeta^2-\left(\frac{c_l}{c_s}\right)^2\right)^2 - 4\zeta^2(\zeta^2-1)^{1/2}\left(\zeta^2-\left(\frac{c_l}{c_s}\right)^2\right)^{1/2} \tag{3.11}$$

The linear field in the simulation is computed via this analytical solution and is used to determine the nonlinear derivatives in the nonlinear field.

3.3.2 Nonlinear field (Secondary)

The nonlinear field is assumed to be a quadratic stress-strain displacement and therefore implements the following governing quadratic partial differential equation of motion in isotropic media in three dimensions,

$$\begin{aligned}\rho_0\frac{\partial^2 u_i}{\partial t^2} - \mu\frac{\partial^2 u_i}{\partial x_k\partial x_k} - \left(K+\frac{\mu}{3}\right)\frac{\partial^2 u_l}{\partial x_l\partial x_i} = \\ \left(\mu+\frac{A}{4}\right)\left(\frac{\partial^2 u_l}{\partial x_l\partial x_k}\frac{\partial u_l}{\partial x_i}+\frac{\partial^2 u_l}{\partial x_l\partial x_k}\frac{\partial u_i}{\partial x_l}+2\frac{\partial^2 u_i}{\partial x_l\partial x_k}\frac{\partial u_l}{\partial x_k}\right)+ \\ \left(K+\frac{\mu}{3}+\frac{A}{4}+B\right)\left(\frac{\partial^2 u_l}{\partial x_i\partial x_k}\frac{\partial u_l}{\partial x_k}+\frac{\partial^2 u_k}{\partial x_l\partial x_k}\frac{\partial u_i}{\partial x_l}\right)+ \\ \left(K-\frac{2}{3\mu}+B\right)\left(\frac{\partial^2 u_i}{\partial x_k\partial x_k}\frac{\partial u_l}{\partial x_l}\right)+ \\ \left(\frac{A}{4}+B\right)\left(\frac{\partial^2 u_k}{\partial x_l\partial x_k}\frac{\partial u_l}{\partial x_i}+\frac{\partial^2 u_l}{\partial x_i\partial x_k}\frac{\partial u_k}{\partial x_l}\right)+ \\ (B+2C)\left(\frac{\partial^2 u_k}{\partial x_i\partial x_k}\frac{\partial u_l}{\partial x_l}\right)\end{aligned} \tag{3.12}$$

where u_i is the ith component of the particle displacement, k is the bulk modulus, and μ is the shear modulus.The terms x_1, x_2 and x_3 are the rectangular co-ordinates. A, B and C are the third-order elastic constants, these are the cubic-strain terms for elastic energy [53]. The elastic moduli are determined as $K = E/3(1-2v)$ and $\mu = E/2(1+v)$. The left side of Eq. 3.12 is the linear contribution and the right hand side is the nonlinear perturbation.

Since the nonlinear contribution of the secondary field is significantly smaller than the incident field, the contribution of the secondary field to the right hand-side is ignored. This is known as a 'quasi-linear' approximation and is implemented theoretically during the derivation of the nonlinear wave equation via the perturbation method [33]. We can therefore implement the following nonlinear equation of motion,

$$\rho_0 \frac{\partial^2 u_i^{(s)}}{\partial t^2} - \mu \frac{\partial^2 u_i^{(s)}}{\partial x_k \partial x_k} - \left(K + \frac{\mu}{3}\right) \frac{\partial^2 u_l^{(s)}}{\partial x_l \partial x_i} = F_i \tag{3.13}$$

splitting these terms into temporal and spatial derivatives we end up with the following equation,

$$\frac{\partial^2 u_i^{(s)}}{\partial t^2} = \left[\mu \frac{\partial^2 u_i^{(s)}}{\partial x_k \partial x_k} + \left(K + \frac{\mu}{3}\right) \frac{\partial^2 u_l^{(s)}}{\partial x_l \partial x_i} + F_i \right] \frac{1}{\rho} \tag{3.14}$$

with the following forcing terms,

$$
\begin{aligned}
F_i = &\left(\mu + \frac{A}{4}\right)\left(\frac{\partial^2 u_l^{(0)}}{\partial x_k \partial x_k}\frac{\partial u_l^{(0)}}{\partial x_i} + \frac{\partial^2 u_l^{(0)}}{\partial x_k \partial x_k}\frac{\partial u_i^{(0)}}{\partial x_l} + 2\frac{\partial^2 u_i^{(0)}}{\partial x_l \partial x_k}\frac{\partial u_l^{(0)}}{\partial x_k}\right) + \\
&\left(K + \frac{\mu}{3} + \frac{A}{4} + B\right)\left(\frac{\partial^2 u_l^{(0)}}{\partial x_i \partial x_k}\frac{\partial u_l^{(0)}}{\partial x_k} + \frac{\partial^2 u_k^{(0)}}{\partial x_l \partial x_k}\frac{\partial u_i^{(0)}}{\partial x_l}\right) + \\
&\left(K - \frac{2}{3\mu} + B\right)\left(\frac{\partial^2 u_i^{(0)}}{\partial x_k \partial x_k}\frac{\partial u_l^{(0)}}{\partial x_l}\right) + \left(\frac{A}{4} + B\right)\left(\frac{\partial^2 u_k^{(0)}}{\partial x_l \partial x_k}\frac{\partial u_l^{(0)}}{\partial x_i} + \frac{\partial^2 u_l^{(0)}}{\partial x_i \partial x_k}\frac{\partial u_k^{(0)}}{\partial x_k}\right) + \\
&(B + 2C)\left(\frac{\partial^2 u_k^{(0)}}{\partial x_i \partial x_k}\frac{\partial u_l^{(0)}}{\partial x_l}\right)
\end{aligned}
\tag{3.15}
$$

The nonlinear forcing terms are calculated using the linear displacement field, u^0, calculated from the analytical solution for linear wave propagation (see Eq. 3.8). The derivatives for the forcing terms and secondary field are computed using finite difference (FD) stencils to approximate the solution at each time-step. Prior to this it is necessary to expand the Einstein notation of the derivatives in the forcing terms in Eq. 3.15 (see Appendix A). To ensure that accuracy was maintained, a 4th order central difference formula was implemented for both the first and second order derivatives. The derivatives are computed spatially using this formula and temporally with a Runge-Kutta 4th order time stepping routine (see Appendix B).

3.3.3 Nonlinear Work Done, ψ

The nonlinear phased array simulation infers the nonlinear sensitivity of the array by assessing the implicit energy flux from the incident (linear) field to the secondary (nonlinear) field at various focal points in space. The partial differential equation defined in Eq. 3.12 could be solved directly using a similar method without perturbation approximations, producing a more accurate solution. However, the purpose of this modelling is to evaluate the energy transferred due to nonlinearity, in terms of magnitude and where it exists in space. By keeping explicit separation of the incident and secondary field this can be achieved more simply than

modelling the field as a whole. If solved directly as one field it would require computation of the diffuse field which is a computationally expensive endeavour. Instead, this can be achieved implicitly by evaluating the nonlinear work done by the incident to the secondary field. In the methodology presented there is no nonlinear energy loss from the incident field, since it is inferred implicitly. The nonlinear work done by the incident field to the secondary field is defined as,

$$\Psi(\bar{r}) = \int_{t_1}^{t_2} \bar{F}(\bar{r},t)\dot{\bar{u}}^{(s)}(\bar{r},t)dt, \tag{3.16}$$

where t_1 and t_2 are the time limits of the simulation and $F(\bar{r},t) = (F_x, F_z)$ is the nonlinear forcing vector for each time step along the x and z axis. The time length of simulation is set to ensure the incident field has focused at the focal point. The key benefit of modelling the nonlinear work done is that the metric is spatially resolved within the field meaning the time of the simulation only has to be sufficiently long to allow the incident field to propagate to the focal point. The nonlinear weighting function ψ within a specimen of aluminium are presented in Fig. 3.2 for multiple focusing points, where it is clear that the magnitude of nonlinear energy transferred between fields changes with the distance from the array. The nonlinear energy transferred between the two fields for multiple focus points can be used to infer the nonlinear sensitivity profile of the array.

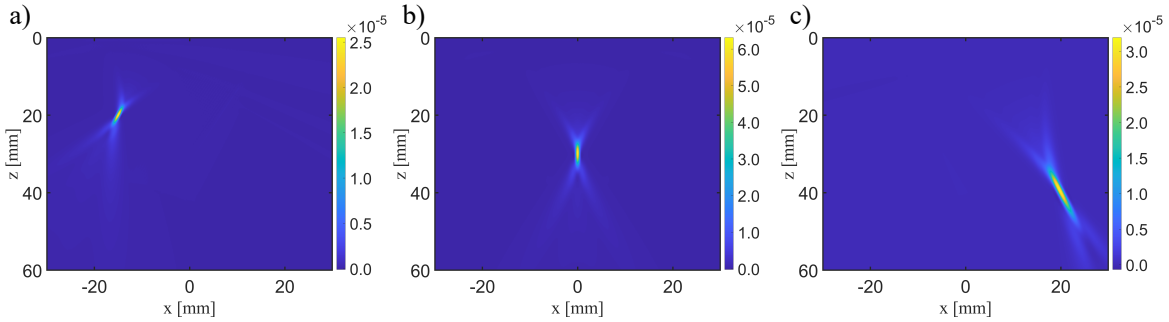

FIGURE 3.2: Nonlinear weighting function, $\psi(\bar{r})$, for aluminium various focal points: (a) $\bar{r}_f$ = [-15 20] mm, (b) $\bar{r}_f$ = [0 30] mm and (c) $\bar{r}_f$ = [20 40] mm.

3.3.4 Nonlinear sensitivity profile, η

To determine the nonlinear sensitivity profile the weighting function in Fig. 3.2 must be measured at each focal point, $\bar{r}_f$. It is required that a similar measurement of energy transfer is used between the work done metric in the simulation and nonlinear energy metric in the experiments. The values taken from the experimental nonlinear images will be maximum γ from each image, which indicates energy lost from the fundamental at the crack tip. The experimental sensitivity is assessed by translating the array and measuring the response of a crack tip using the multiple sensitivity regions of the array (this is discussed in further detail in Section 3.4). The reduction in sensitivity when the array is translated will result in reduced detectability, and therefore the maximum value of the nonlinear feature is most straight forward and applicable. Since the validation process infers the energy lost at the focal point through the detection of the maximum feature (i.e. the crack tip) in the image, it is necessary to repeat this process in the simulation. The energy loss from parallel transmission can be determined by calculating the maximum of $\Psi(\bar{r}_f)$. This can then be related directly to the nonlinear metric γ by subtracting the sequential and parallel energy flux fields. If the spatial energy flux from the sequential case is denoted $\Psi_s(\bar{r}_f)$, then the contribution of nonlinear elastic energy to the nonlinear imaging metric is expressed as,

$$\eta(\bar{r}_f) = \frac{E_s - E_p}{E_s} = \frac{\max(\Psi_s(\bar{r}_f)) - \max(\Psi(\bar{r}_f, \bar{r}))}{\max(\Psi_s(\bar{r}_f))} \tag{3.17}$$

Note that the sequential term in Eq. 3.17 is spatially invariant since the nonlinear losses occur during acquisition and are independent of the sequential post-processing calculation. Therefore, the parallel energy flux can be used directly as a measure of array sensitivity.

3.3.5 Model parameters

3.3.5.1 Material and array parameters

The nonlinear simulation was conducted for two commonly used isotropic materials: Aluminium 2014 and Mild Steel. The material parameters for each undamaged material are presented in Tab. 3.1 and are consistent with the materials used in the experimental analysis. The steel third-order elastic constants (TOECs) are obtained from a study by Takahashi et al which investigates the second and third order elastic constants of polycrystalline steels [8]. Stress is applied to the steel sample and is increased step-wise, and the velocity of the elastic wave is measured at each step. For this study, the results from the S30 sample in an adiabatic state is used as the TOECs for simulating the steel sample. The TOECs in this study are Murnaghan constants (l,m,n) and can be represented as Landau-Lifshitz (A,B,C) constants using $l = B+C$, $m = A/2+B$ and $n = A$. The aluminium values are from work by Lubarda et al. which implements an extension of linear theory for calculating TOECs.

Property	Aluminium 2014	Mild Steel
Young Modulus, E (GPa)	90	200
Poisons ratio, v	0.35	0.26
Density, ρ (kg/m^3)	2700	7850
A (GPa)	-344	-505
B (GPa)	-124	-65
C (GPa)	-19	-730
β	7.18	8.70

TABLE 3.1: Material mechanical properties for Aluminium 2014 and Mild Steel [7, 8].

The arrays simulated were Imasonic 1, 2.5 and 5 MHz arrays, as presented in Tab. 3.2,

Centre frequency (MHz)	No. of El. (mm)	El. width (mm)	El. pitch (mm)
1	64	15	1.5
2.5	64	15	0.5
5	64	10	0.6

TABLE 3.2: Phased array specifications used for experiments.

The ultrasonic displacement Δ is set to 6 nm for each element transmission. This is a book value from work by Potter et al. [66] measured using a laser vibrometer.

3.3.5.2 Spatial and temporal parameters

The simulation propagation time is set to ensure the incident focused beam propagates to the focal point and beyond to ensure analysis of the point-spread function. This is achieved by setting $t_1 = 0$ and establishing t_2 in Eq. 3.16 to ensure all the energy has propagated to the focal point. This was achieved by calculating the distance to the focal point for each transmission and calculating the required propagation time given the longitudinal material velocity, c_l. The time limits are proportional to the grid size (x,z), and therefore larger samples (where an increased image domain is required) will increase the time limits. The various simulation times used for each transmission frequency is presented in Tab 3.3, which are adjusted to account for varying image domain sizes used for each simulation. The image domain sizes are adjusted to account for differing pitch sizes, to ensure sufficient imaging space is computed for analysis whilst computational performance is maintained. The varying longitudinal sound speed for each material is negligible, therefore to be conservative the simulation durations are calculated using the material with the lowest sound speed.

Centre frequency (MHz)	Simulation duration, t_2 (μ s)
1	17.5
2.5	10
5	10

TABLE 3.3: Simulation duration for each transmission frequency and material simulated.

The temporal resolution Δt is calculated to ensure accurate computation of the nonlinear field. This is achieved by sampling 25 time points per period of the excitation frequency, ω_0, using the following equation,

$$\Delta t = \frac{T_p}{25} \tag{3.18}$$

where T_p is the periodic time which is calculated as $T_p = 1/\omega_0$.

The spatial resolution Δx is determined to ensure 25 sample points per wavelength λ using the following calculation,

$$\Delta x = \frac{\lambda}{25} \tag{3.19}$$

where $\lambda = \frac{c_l}{\omega_0}$. These spatial and temporal resolutions are sufficient for the calculation of nonlinear field terms.

3.3.5.3 Attenuation

Attenuation can have a significant effect on the propagation of longitudinal and shear waves in a medium. It is therefore necessary to account for such phenomena in this simulation. This is achieved by implementing an attenuation coefficient in the incident field calculation. Since the secondary field is being driven by the incident field, the reduction in displacement due to attenuation in the incident field will translate into the secondary field directly. The attenuation term to be included in the incident field calculation in Eq. 3.8 is calculated as,

$$C_{L,S} = \exp\{-\alpha_{L,S} x\} \tag{3.20}$$

where α is the attenuation (Np/m) and x the propagated distance in the x-direction in m. It is expected that the attenuation will significantly affect the nonlinear sensitivity, the maximum sensitivity is expected to spatially shift towards the array due to exponentially

increasing attenuation losses with distance propagated. The attenuation coefficients α used for the simulation are presented in Tab. 3.4, and are book values from a study by Zhang et al. [68]. The attenuation values are applied to the linear wave field which forces the nonlinear field, therefore the attenuation directly influences the nonlinear work done and therefore the nonlinear sensitivity.

Material	1 MHz		2.5 MHz		5 MHz	
	L	S	L	S	L	S
Aluminium	5.60×10^{-3}	2.10×10^{-3}	1.60×10^{-1}	7.59×10^{-2}	1.22	9.42×10^{-1}
Steel	1.70×10^{-3}	7.00×10^{-3}	6.54×10^{-2}	2.69×10^{-1}	9.95×10^{-1}	3.99

TABLE 3.4: Longitudinal (L) and shear (S) attenuation (Np/m) for Aluminium 2014 and Mild Steel.

3.4 Experimental sensitivity

3.4.1 Experimental parameters

By following the NUI methodology highlighted in Section 3.2 an experimental sensitivity study is performed using a fatigue crack tip grown in a Aluminium 3 point-bend (3PB) specimen. The purpose of this is to determine the sensitivity of the array to a known and consistent nonlinear feature (i.e. the crack tip), which is a discrete nonlinear feature much higher in amplitude than the surrounding material nonlinearity, meaning a higher SNR is available for measurement. For these reasons it can be used as a close experimental approximation of a point-like nonlinear feature. Since this feature is inherently time invariant, it is possible to determine the sensitivity of the array in the x direction by translating the array laterally relative to the nonlinear feature location as seen in Fig. 3.3. During this process nonlinear images are acquired at each translation position where the feature will be detected using various locations within the sensitivity profile of the array. To evaluate the through depth sensitivity, z, the top surface of the specimen is machined down in 6 stages (of 5 mm increments) for the lateral study to be conducted at each of these machining steps. By taking the maximum of each of

these nonlinear images for lateral scans for through depth stages an experimental sensitivity map can be determined.

The array translation is conducted by mechanically scanning the array along the surface of the specimen above the crack tip. Nonlinear diffuse images taken at different translation positions are presented in Fig. 3.4 where the increased sensitivity is observed when the array is directly above the feature. This provides an increased magnitude of the nonlinear parameter γ and SNR compared with the translated positions off-set from the centre axis. The maximum γ reduces by approximately 27% and 36% for +9 mm and -12 mm off-sets respectively, confirming that detectability of the feature is dependent on the location of the feature relative to the array.

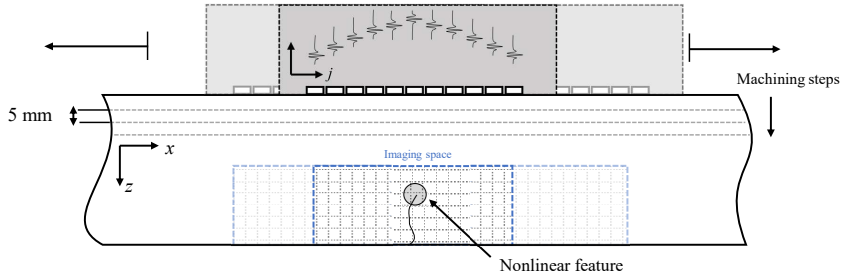

FIGURE 3.3: Experimental configuration for phased array translation process.

The experimental validation was conducted with 2.5 and 5 MHz phased arrays where approximately 40 nonlinear images were taken at multiple translation points for each machining stage. In the case of NUI it was observed that, the variability of results can be significant due to varying transmission output from the array controller and variations in coupling (this is discussed further in Section 6.3). To reduce the impact of this variability a low-pass filter is applied to each lateral section, to smooth out the experimental error. Using the lateral sections from each machining stage the data is interpolated to the imaging space used for both the experimental and simulated data, allowing for direct comparison of the sensitivity profiles.

All NUI experiments were conducted using a Verasonics array controller using Imasonic

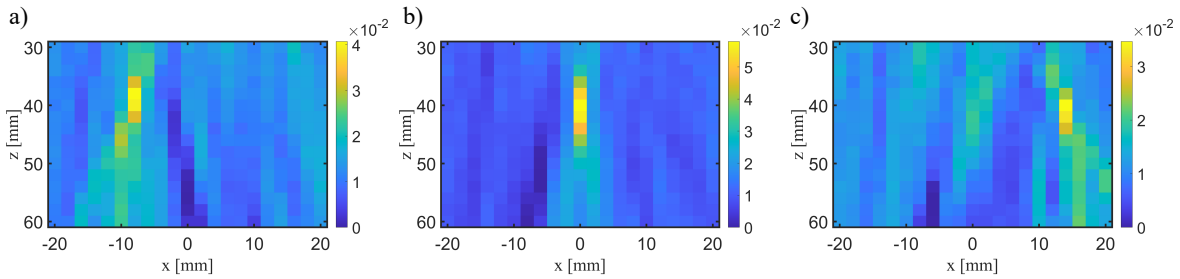

FIGURE 3.4: Nonlinear diffuse images (γ) transmitting at 5 MHz for multiple translations on the surface: (a) +9 mm (b) 00 mm and (c) -12 mm.

arrays specified in Tab. 3.2. A cycle length of 3 is facilitated via the arbitrary waveform generation capabilities of the array controller to match the input signal length used in the simulation. However, it is worth noting that the exact cycle length will not be transmitted into the material due to the array transfer function. The diffuse times (t_r and T) are set for each transmission frequency to ensure the nonlinear energy is captured during the diffuse field. These times are based on preliminary experiments to determine the most effective diffuse times for resolving the nonlinear feature for each transmission frequency. The selection of the diffuse times through statistical analysis will be investigated in Chapter 6.

Trans. Frequency	t_r	T
T1	0.5	0.08
T2.5	0.25	0.04
T5	0.25	0.04

TABLE 3.5: Start-time, t_r(ms), and window length, T(ms), for each transmission frequency used for the 3PB specimens.

3.5 Results

3.5.1 Simulation and experimental sensitivity

Following the defined simulation and experimental procedures the nonlinear sensitivity is evaluated for multiple array transmission frequencies, as well as varying array sizes, defined specifically for different frequency transmissions. By evaluating Eq. 3.17 for multiple focus

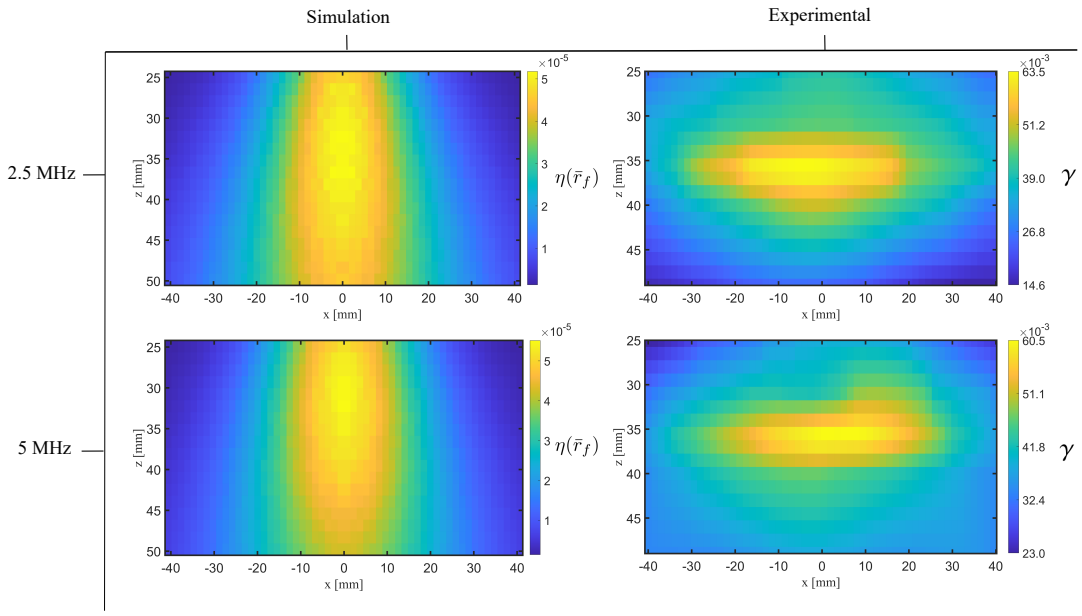

FIGURE 3.5: Simulation and experimental results for 2.5 and 5 MHz array transmissions.

points in the imaging space the dependence on η value on the the location measurement point relative to the array is measured, producing a simulated sensitivity map. It is expected that the nonlinear work done η (inferred from the TOECs) will vary as a function of position in the $x-z$ space. This spatial variation is expected to converge closely with experimental results where a crack tip is used as a known source of nonlinearity.

The sensitivity results using the 2.5 and 5 MHz phased arrays are presented in Fig. 3.5, where there is a consistent maxima at a depth of 36 mm for both transmission frequencies across the experimental and simulated data. The distribution of the profile along the x-axis at the maxima is relatively consistent across the experimental and simulated results where there is a reduction in sensitivity of 50 % between -25 mm and 25 mm for both transmission frequencies. The sensitivity profile along the z-axis (through depth) does not show consistency, the point of highest experimental sensitivity is much more localised showing that the sensitivity drops by 50% between 30 mm and 42 mm for both frequencies. In the simulation case, both transmission frequencies show significant sensitivity between 25 mm and 50 mm reducing by only 20%. This variation in simulation and experimental sensitivities is potentially caused by

differing nonlinear sources used for each sensitivity investigation.

The more localised experimental sensitivity profile is potentially caused by changing exposure to the interfaces of crack tip with depth, altering the intensity of the opening and closing of the crack interface, resulting in less nonlinearity being induced at the focal point. For example, when focused at a crack tip close to the array the focused beam excites the interface of crack tip at more angles and is therefore exciting a larger surface area of the interfaces, resulting in increased acoustic nonlinearity. When focusing further into the material the angle of interaction is reduced and a reduced surface area of the interface is excited, resulting in less nonlinearity. The sensitivity in the experimental case is therefore determined by both the intensity of ultrasonic energy incident at the focal point and the exposure of the displacement incident waves to the surface area of the interfaces. The combination of these effects results in a more localised sensitivity profile where sufficient ultrasonic energy is incident at the focal point and increased exposure to the crack induces more nonlinearity.

3.5.2 Material analysis

The nonlinear sensitivity in different materials is desired to investigate the performance of NUI for a variety of polycrystalline compounds with different material properties for nonlinearity. The third order elastic constants (TOECs) for the materials is expected to have a significant influence on the nonlinear work done by the incident field, since the degree of material nonlinearity is defined by the measured TOECs which determines the forcing term in Eq. 3.15. In addition, it is expected that varying attenuation values will have a significant effect on the nonlinear work done, since the nonlinear field is driven by the linear field. For instance, an increase in attenuation will reduce the incident wave amplitude at the focal point, and in turn will reduce the nonlinear work done. Attenuation is expected to adjust the sensitivity profile of the array as well, the point of highest sensitivity is expected to move towards the array since the

linear field will decay exponentially causing near field focusing to provide higher sensitivity. The longitudinal attenuation will be most influential since the focusing is achieved for the longitudinal component meaning mostly bulk wave energy is transferred to the nonlinear field at the focal point. To address these effects the percentage difference between simulations with and without attenuation is calculated to determine the quantitative differences between the two sensitivity profiles. It is expected that the aluminium sensitivity profile will be more influenced by attenuation since the measured attenuation rates are higher than steel for the selected frequencies. In addition, attenuation is expected to influence the nonlinear sensitivity at higher frequencies since the attenuation rates are relatively larger.

The simulated sensitivity results transmitting at 5 MHz are presented in Fig. 3.6. It can be seen that in the case of aluminium and steel the attenuation reduces the nonlinear work done, η, by approximately 16% and 14% respectively. The results for a 2.5 MHz transmission are presented in Fig. 3.7 and it can be seen that in the case of aluminium and steel the attenuation reduces the nonlinear work done by approximately 2% and 0.8% respectively. The results for a 1 MHz transmission presented in Fig. 3.8 confirms that the attenuation reduces the nonlinear work done by 0.14% and 0.04% for aluminium and steel respectively. It is clear that the reduced attenuation rates at 1 MHz influence the nonlinear sensitivity less compared with the 2.5 and 5 MHz transmissions as expected.

The subtracted images show the largest difference in nonlinear energy occurs at a depth of 50 mm for 5 MHz , 60 mm for 2.5 MHz and 110 mm for the 1 MHz transmission. The spatial distribution of this percentage difference shows the sensitivity profile is shifted towards the array in the presence of attenuation, confirming that the sensitivity of the array is spatially determined by attenuation rates. The linear field energy is attenuated at a higher rate reducing the energy incident at the focal point, causing less work done on the nonlinear field and thus reducing sensitivity. The exponential attenuation of wave energy with distance means focal

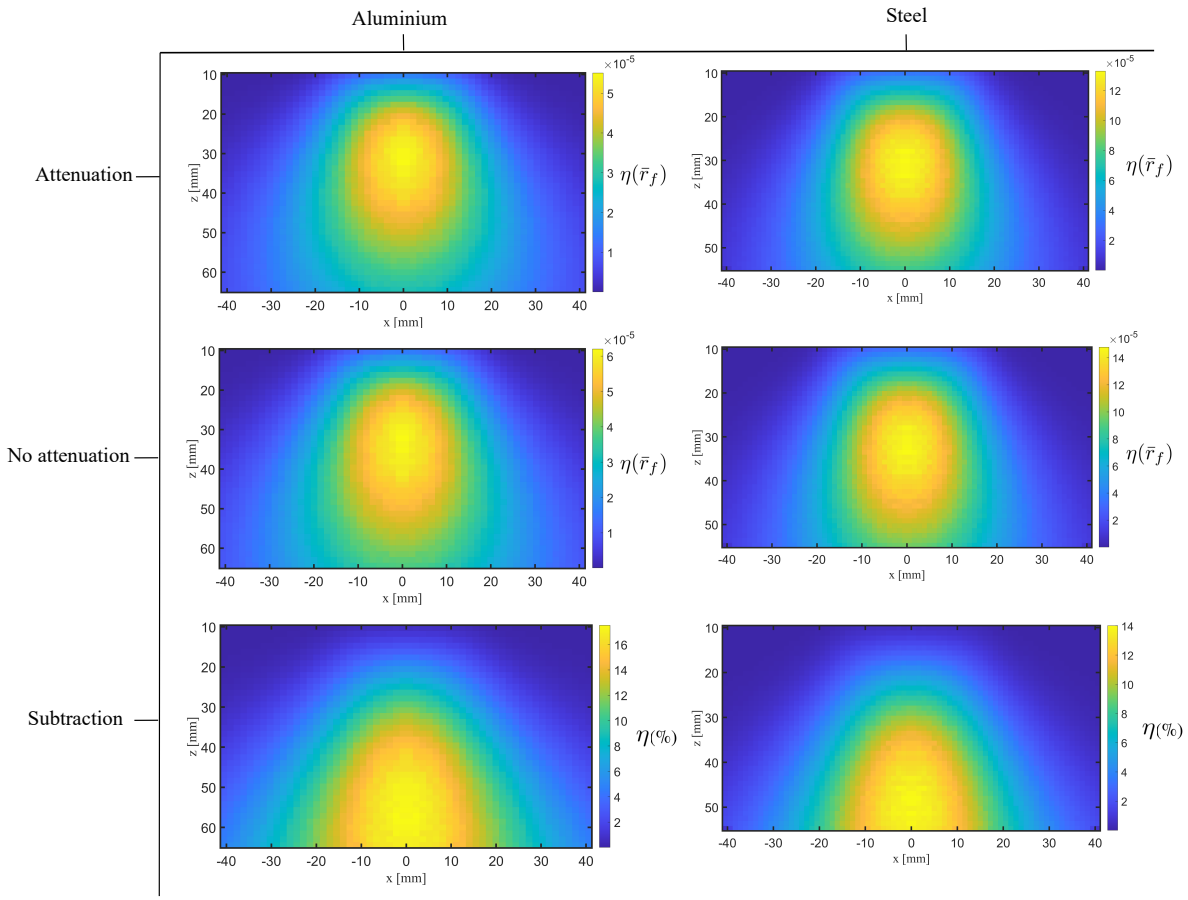

FIGURE 3.6: Nonlinear simulated sensitivity profile transmitting at 5 MHz for Aluminium and Steel with and without attenuation.

points further away from the array will transfer less energy to the nonlinear field, resulting in a shift in sensitivity towards the array.

When comparing the different materials without attenuation, generally it can be seen that the nonlinear work done is larger in steel compared with aluminium by a factor of 3 for 2.5 and 5 MHz transmission frequencies. The nonlinearity parameter β is larger for steel compared with aluminium and therefore an increase in the nonlinear work done is expected since the forcing terms which are calculated from the TOECs, determine the nonlinearity of the material. This is also observed for the 1 MHz transmission where there is an increase in the nonlinear work done by a factor of 2 for steel compared with aluminium. When attenuation is accounted for the difference in sensitivity performance is increased since the steel material experiences

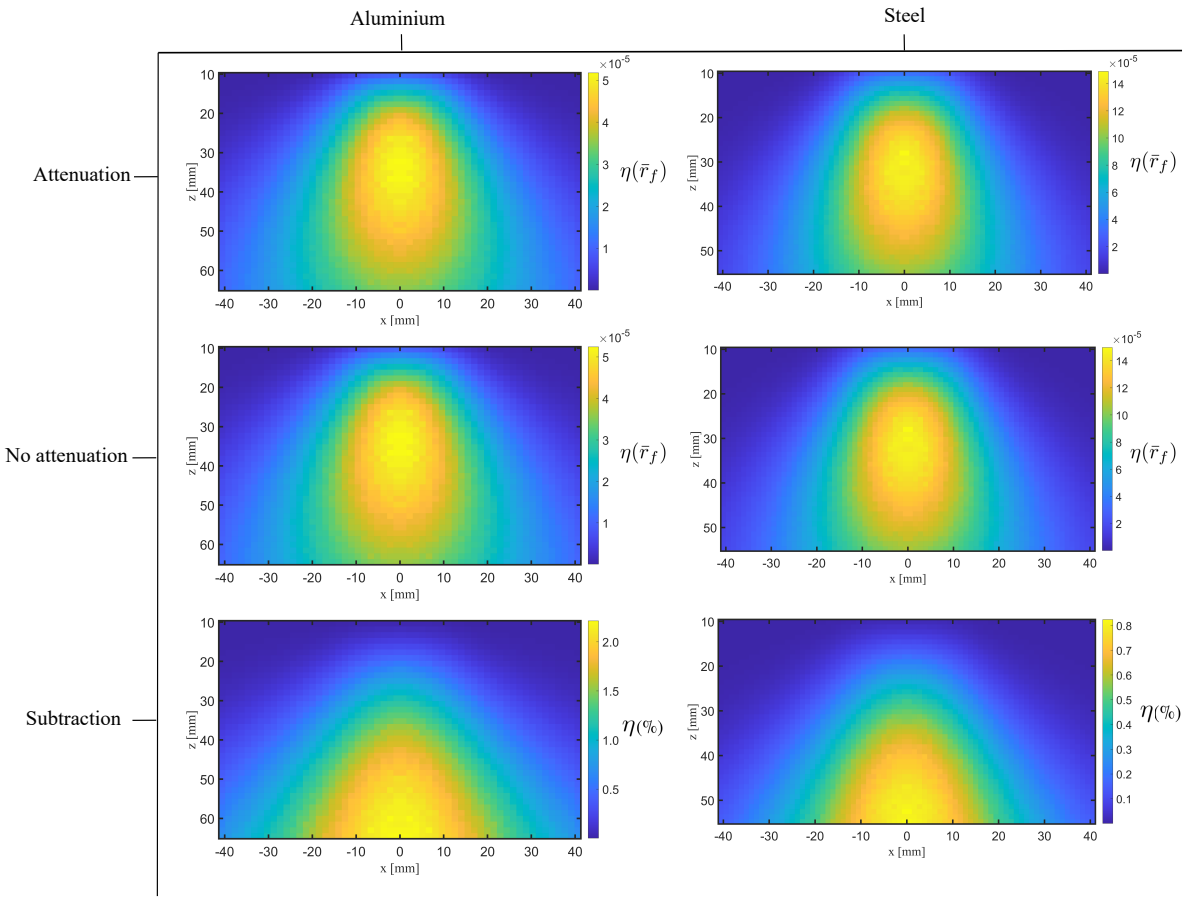

FIGURE 3.7: Nonlinear simulated sensitivity profile transmitting at 2.5 MHz for Aluminium and Steel with and without attenuation.

less longitudinal attenuation, and therefore more energy is transferred to the nonlinear field at the focal point.

The different frequency transmissions produces consistent maximum nonlinear sensitivity levels for each material. Despite induced nonlinearity being proportional to transmission frequency, the reverse effects of attenuation at higher frequencies reduces the sensitivity. At lower frequencies there is less nonlinearity induced, however the effects of attenuation are lower meaning nonlinear energy is not degraded significantly. This consistency is also observed in the experimental data in Fig. 3.5 where there is only an increase in maximum sensitivity at 5 MHz by approximately 5% compared with 2.5 MHz. This suggests that transmission frequency selectivity does not significantly effect the performance of the NUI method over the

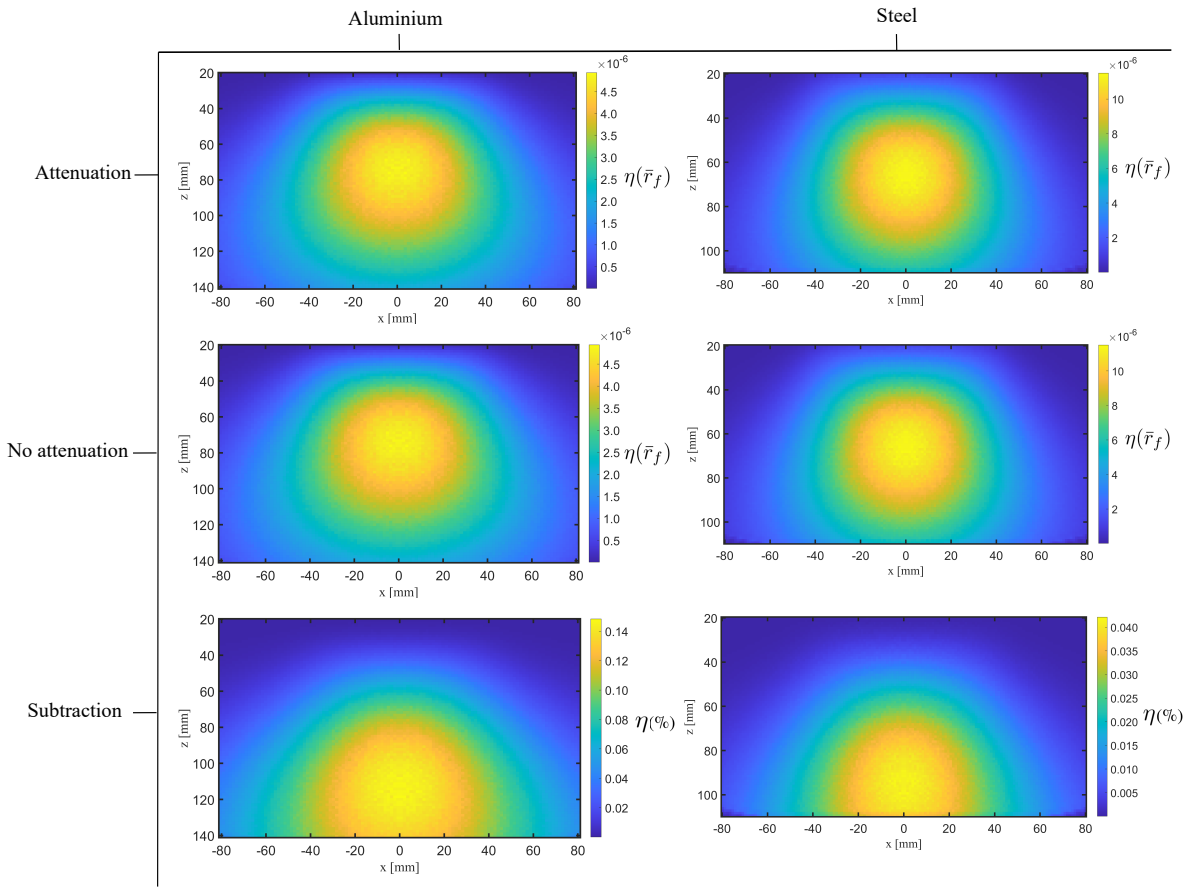

FIGURE 3.8: Nonlinear simulated sensitivity profile transmitting at 1 MHz for Aluminium and Steel with and without attenuation.

selected frequency range. However, it is important to consider that higher attenuation rates across real life samples will effect the nonlinear sensitivity and therefore the implementation of transmission frequencies will be material specific for industrial samples. These results also confirm that the location of the nonlinear source relative to the array is an important factor to ensure optimised resolution of the features. Since the location of the fatigue crack (distance from the array) cannot be controlled, any dynamic control over the sensitivity profile of the array would be very beneficial.

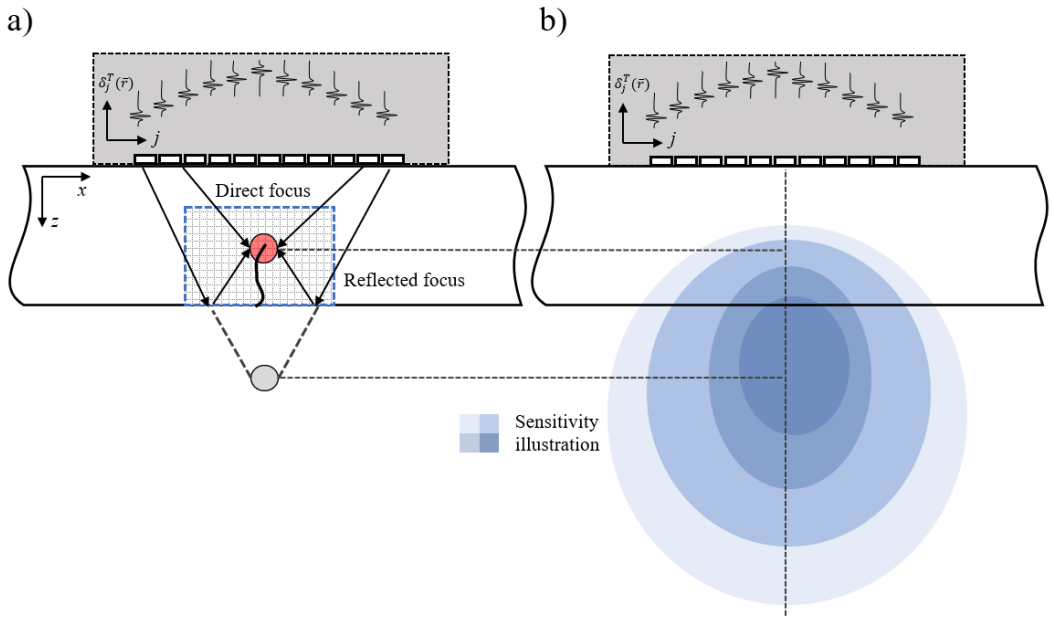

FIGURE 3.9: Multi-view propagation configuration.

3.5.3 Multi-view diffuse image

The previous study evaluated the sensitivity of the phased array, determining a specific distance from the array where there is significant and heightened sensitivity. In real specimens where fatigue samples are to be analysed without destructive measures (such as machining) it is desirable to examine nonlinear features (i.e. closed crack tips) using the highest sensitivity point of the array. Since the location of crack tips in samples cannot be controlled and the phased array sensitivity for NUI is not dynamic, a multi-view NUI method is proposed to focus at points within the image space reflected off the back-wall. The method is implemented by focusing at image pixel points past the back-wall, as illustrated in Fig. 3.9(a), causing the beam-formed wave to reflect off the back wall and focus in the material. If the sensitivity of the array is heightened at this point, assuming there is minimal transmission loss at the boundary, it is expected that there will be increased sensitivity to the crack tip using the reflected focus over the direct focus, as seen in the illustration in Fig. 3.9(b)). For this experiment a total of 3 reflection images will be captured in the following order: back-wall (BW), front-wall (FW) and

back-wall (BW). This process is conducted by focusing past the back-wall at focal positions z_f up to a maximum of three times the depth of the sample.

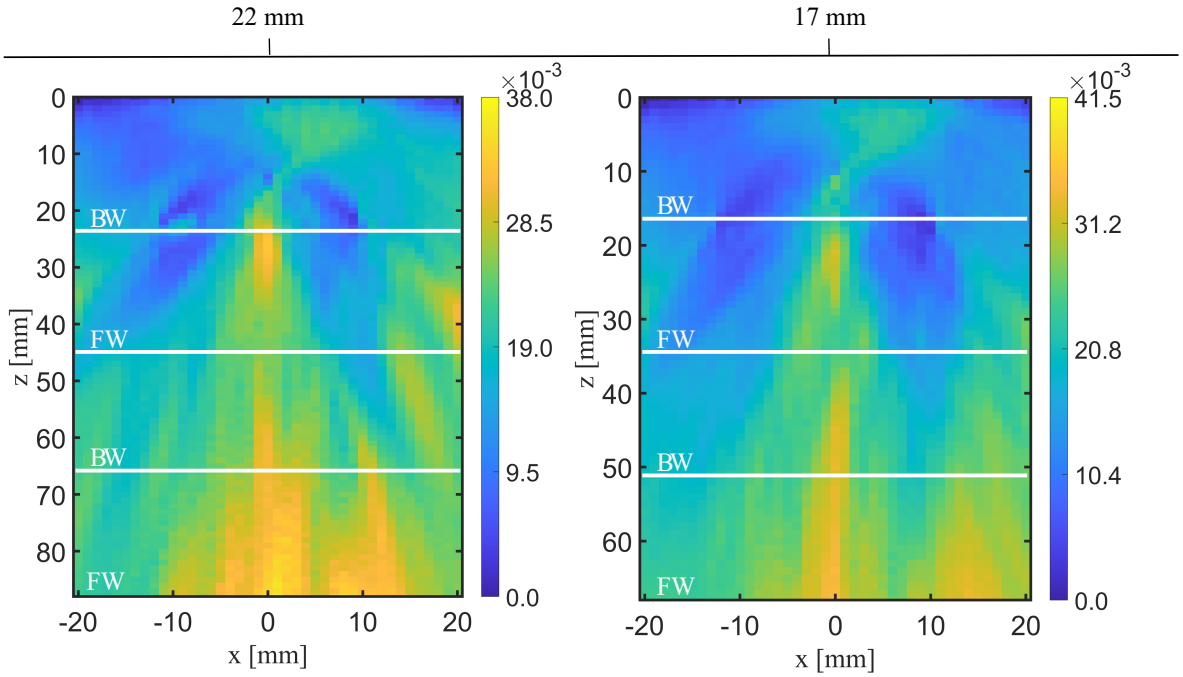

FIGURE 3.10: Multi-view diffuse nonlinear image γ transmitting at 5 MHz for machining depths 22 mm and 17 mm.

The multi-view NUI results transmitting at 5 MHz are presented in Fig. 3.10, where the full nonlinear images are plotted displaying multiple reflections through depth for two machining depth sizes: 22 mm and 17 mm. The white lines indicate the location of the front and back-wall for multiple reverberations. At the 22 mm machining depth size it is clear from these results that there is no detectability of the feature in the direct image (focusing from 0 to 22 mm). When evaluating the sensitivity profile for a 5 MHz transmission (see Fig. 3.5), at this focusing range the feature is undetectable. Therefore in the direct image in-sufficient incident energy is exciting the crack tip. The nonlinear feature has been detected in the 1st reflection image focusing past the BW (focusing from 22 to 44 mm) at a depth of 25 mm in the image. The 2nd reflection past BW-FW (focusing from 44 to 66 mm) shows detectability of the feature at 61 mm in the image. The 3rd reflection image focuses past the BW-FW-BW (focusing from 66 to 88 mm) is not able to resolve the feature. This is expected to be caused by low level ultrasonic

energy at the focal point caused by the limited sensitivity a large distances from the array. Once again, this is confirmed by the experimental sensitivity profile in Fig. 3.5, which shows the crack tip is undetectable when focusing past 50 mm depth. The energy captured in this image is attributed to random noise dominating the nonlinear energy captured and polluting the metric. At a 17 mm machining depth the nonlinear feature becomes slightly more dominant in the 2nd reflections image at a depth of 48 mm, suggesting a more sensitive region of the array is detecting the feature at this point. The feature is still undetectable in the direct image and is still detectable in the 1st reflection image. The detected crack tip and additional nonlinear artefacts throughout all image views are consistent across machining stages (offset from each other by 4 mm, as expected from machining). This confirms the response of the known crack tip is being detected and implies the additional artefacts are detected nonlinearity in the material.

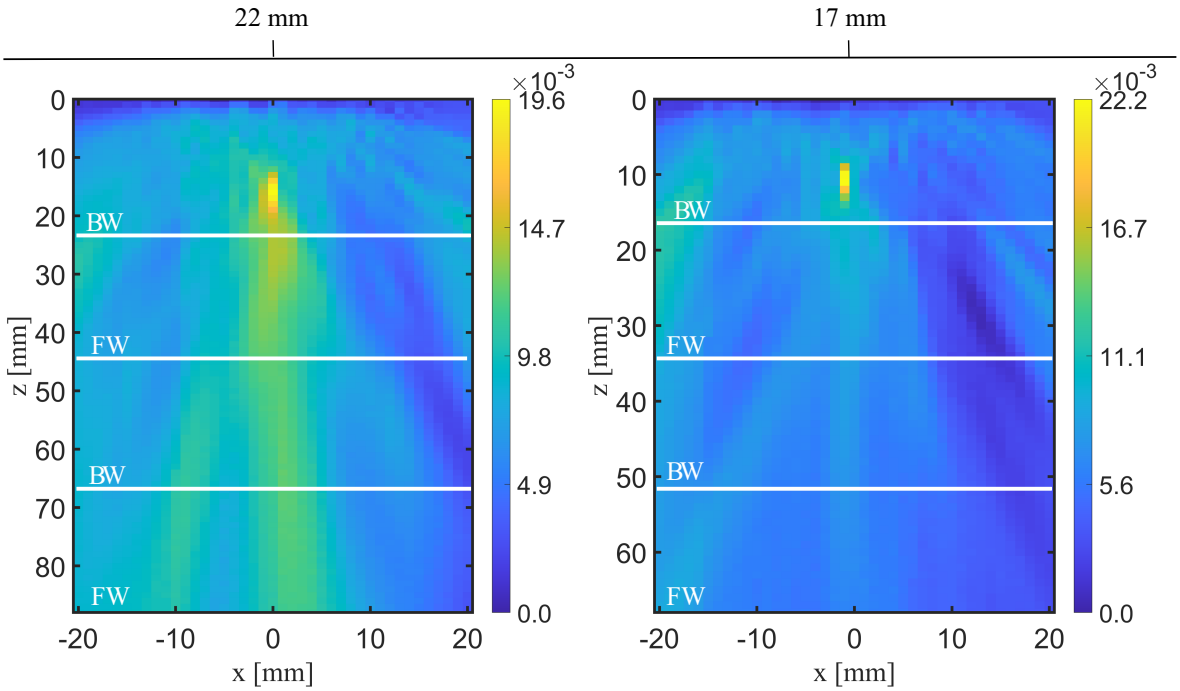

FIGURE 3.11: Multi-view diffuse nonlinear image γ transmitting at 2.5 MHz for machining depths 22 mm and 17 mm.

The 2.5 MHz transmission results are presented in Fig. 3.11 where the feature is only detectable in the direct images for both depths. Some energy is observed in the reflection

images for the 22 mm depth size sample, however the crack tip is not fully resolvable. The experimental sensitivity results presented in Fig. 3.5 show reduced sensitivity in the direct image, and increased sensitivity in the 1st and 2nd reflection images. This in-consistency can be associated with energy transmission at the reflection walls, meaning less energy is focused at the focal point. The lower energy focusing at the crack-tip causes a reduction in excited nonlinearity meaning less nonlinear information is available for capture. This reduction in incident energy at the focal point will increase with the number of wall reflections, and results in lower detectability compared with the direct image (despite reduced sensitivity at this range). The 1 MHz transmission results are presented in Fig. 3.12 where the 22 mm machining size results show the feature is resolvable only in the direct image (focusing from 0 to 22 mm). The simulated sensitivity results in Fig. 3.8 show low sensitivity at this range, therefore the detectability of the feature in the direct image is inconsistent with the simulation. It is possible that the crack tip at a particular distance from the array and transmitting at 1 MHz have induced a resonant nonlinearity causing this anomaly. At 17 mm depth size the nonlinear feature is not resolved in any of the views which supports this reasoning. The limited detectability in the reflection images is also associated with energy transmission at the reflection walls, reducing incident energy at the focal point.

The multi-view NUI method results show some benefit transmitting 5 MHz where in some cases the direct image is not capable of detecting the feature. The results for the 1 and 2.5 MHz transmissions are unclear and do not show any benefit to capturing multiple views.

3.5.4 Conclusion

The sensitivity profile of NUI has been established through experimental and simulation analysis. The point of maximum sensitivity for both the experimental and simulated profile is consistent for 2.5 MHz and 5 MHz transmission frequencies. However, the sensitivity profiles

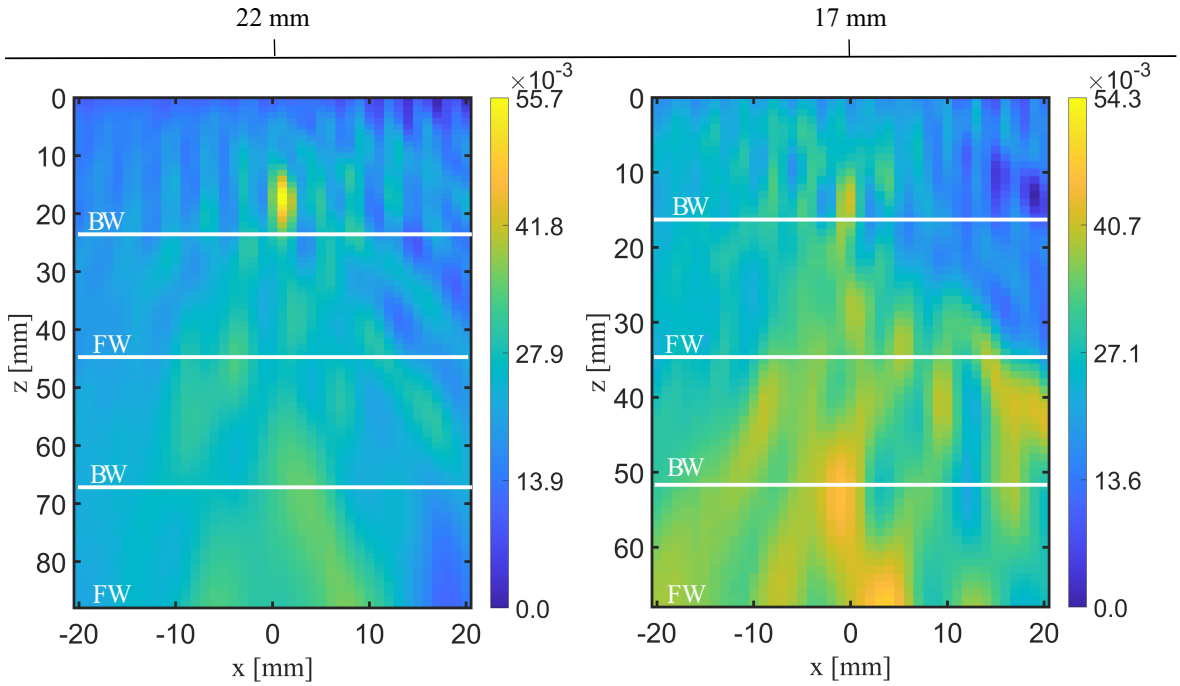

FIGURE 3.12: Multi-view diffuse nonlinear image γ when transmitting at 1 MHz for machining depths 22 mm and 17 mm.

display inconsistencies in sensitivity distribution which has been associated with the exposure to the crack tip during incident excitation. This varying effect leads to a highly localised nonlinear sensitivity profile in the case of the experimental study and has resulted in a limited validation in the z-axis. Along the x-axis the results are more consistent between simulated and experimental analysis.

The influence of attenuation on sensitivity has been investigated through simulations confirming the sensitivity of the profile of the array is shifted towards the array in the presence of attenuation. As expected, this effect is increased at higher frequencies where the influence of attenuation is much higher. In addition, the magnitude of sensitivity (nonlinear work done) reduces in the presence of attenuation as expected. These results confirm that the competing effects of increased attenuation and increased nonlinearity means the performance of the selected transmission frequencies is consistent. However, the distribution of the sensitivity profile should be considered as varying array sizes will change the sensitivity profile significantly.

A multi-view method has been proposed to ensure the most sensitive imaging region below the array is used to detect nonlinear features. This method has proven to be effective for 5 MHz where the nonlinear feature is not detectable using the single-view method. It is therefore suggested that a multi-view approach should be applied to industrial samples where the location of the feature is unknown.

The nonlinear sensitivity profiles for both simulated and experimental work have been determined and it is of interest to further optimise the sensitivity of the NUI method. The next chapter investigates a multi-frequency NUI method for increasing the detectability of closed crack tips in Aluminium.

Chapter 4

Multi-frequency diffuse imaging

4.1 Introduction

In this chapter, a multi-frequency nonlinear ultrasonic diffuse energy imaging (NUI) method is explored to obtain the benefits of nonlinear spectroscopy and is shown to have clear advantages over the single frequency method used in Section 3.2. In particular, this method allows for the effective separation of underlying ultrasonic nonlinear mechanics, such as low-frequency, sub-harmonic and second harmonic components using parallel-sequential modes of transmission (the same transmission modes used in Section 3.2) to create spatial maps for each nonlinear frequency component and increase the signal-to-noise ratio (SNR). The individual frequency components are detected using a dual array configuration, where an additional receiving array with a centre frequency matching the desired frequency component is coupled to the material. An increase in sensitivity is expected at lower frequency components due to reduced attenuation rates, meaning more nonlinear energy is captured. However, at higher frequency components more nonlinearity is induced and therefore an increase in sensitivity is expected despite relatively higher levels of attenuation. Both are expected to provide significant gains for detecting fatigue cracks compared with the current single frequency method [5], which

potentially allows for increased sensitivity to small nonlinear features.

4.2 Multi-frequency diffuse method

The single frequency NUI method determines the nonlinearity at each focal/pixel point by measuring the energy lost from the fundamental frequency. The measurement of energy lost from the fundamental to other frequency components (such as sub-harmonic and second harmonic components) accounts for both quadratic nonlinearity from the material and non-classical nonlinearity from the crack tip. The multi-frequency method measures nonlinearity by evaluating three frequency components: low, sub-harmonic and second harmonic. The low frequency component is induced by mixing within the transmission bandwidth, causing energy to be transferred to the DC component up to approximately the bandwidth of the fundamental frequency. This phenomena is caused by the superposition of two frequencies within the transmission bandwidth and results in the formation of a frequency component at the sum and difference of the two frequencies. When these two frequencies are very close to each other (i.e. in the same bandwidth), the difference of of the two frequencies will be very small and therefore a low frequency component will be generated. The magnitude of energy transferred to he low frequency is elevated in the presence of nonlinearity. When an ultrasonic wave is incident on a closed crack tip, energy is transferred to the sub-harmonic component, at half the fundamental frequency [39–41]. The detection of the sub-harmonic allows for isolation of nonlinearity induced by the crack tip, meaning contributions from material nonlinearity are potentially excluded. The second-harmonic component is induced by quadratic material nonlinearity [15, 30]. It is expected that transmission bandwidth mixing will also contribute to a transfer of energy to the second harmonic.

The detection of elastic nonlinearity as the difference of the statistical diffuse energy between parallel and sequential transmission modes has already been proven to work on fatigue crack

samples [5, 6]. NUI determines the nonlinearity at the focal point by evaluating the relative energy lost a the fundamental frequency between the parallel and sequential fields. The requirement to measure in the diffuse field is consistent with the single frequency method, where the start time, t_r, (the time when elements start receiving signals) and the window length T (the time the elements receive signals for) must be set appropriately for the method to work. The selection of these parameters is a compromise between two competing effects. Firstly, later in time the field converges more closely to a diffuse field. However, further in time the signals will attenuate during propagation leading to a reduced SNR. In the case of detecting multiple frequency components, the correct selection of window length, T, will be paramount for each transmitting and receiving frequency combination, since the range of frequencies have varying attenuation rates, therefore the signals will degrade at different rates. As frequency increases the rate of attenuation increases, meaning the ultrasonic signals will attenuate at a faster rate and a reduced SNR will occur sooner in time. An important consideration when defining the start time t_r is volume, since the convergence rate of a diffuse field is expected to be proportional to the volume of the sample. The more frequent propagating waves are incident with the reflective boundaries (decrease in propagation paths between geometric boundaries) the quicker a diffuse field is formed. This will be discussed in detail in Chapter 6.

Assuming $f_{j,k}(t)$ are the time-domain received signals for each combination of transmit (j) and receive (k) elements in the sequential case. The transmission delay law $\delta_j^T(\bar{r})$ is applied to the j^{th} element to focus at point $\bar{r}$. The parallel time-domain signals are denoted $h_j(t)$ received on element k for the parallel transmission of elements delayed independently by $\delta_j^T(\bar{r})$. The frequency spectra of $f_{j,k}(t)$ and $h_{j,k}(t)$ are given by $F_{j,k}(\omega) = \int_{t_r}^{t_r+T} f_{j,k}(t)e^{-i\omega t}dt$ and $H_k(\omega) = \int_{t_r}^{t_r+T} h_k(t)e^{-i\omega t}dt$, respectively. The diffuse acoustic energy for N element array in sequential transmission E_s at focal point $\bar{r}$ is evaluated as follows,

$$E_s(r) = \sum_{k=1}^{N}\left(\int_{\frac{2}{3}\omega_R}^{\frac{4}{3}\omega_R} \omega^2 \mid \sum_{j=1}^{N} F_{j,k}(\omega) e^{i\omega\delta_j^T(\bar{r})} \mid^2 d\omega\right) \tag{4.1}$$

and the parallel transmission E_p,

$$E_p(r) = \sum_{k=1}^{N}\left(\int_{\frac{2}{3}\omega_R}^{\frac{4}{3}\omega_R} \omega^2 \mid H_k(\omega) \mid^2 d\omega\right) \tag{4.2}$$

The energy at the desired frequency component is determined by integrating over the relative frequency bandwidth. Increasing the bandwidth will increase the ultrasonic energy captured, increasing the resolution of the feature. However, a broad bandwidth will increase sensitivity to more nonlinear components, reducing the selectivity to individual nonlinear frequency components. Therefore the evaluated bandwidth of the signals is defined as $\frac{2}{3}\omega_R$ and $\frac{4}{3}\omega_R$ for the sub-harmonic, fundamental and second harmonic components [5]. The low-frequency component exists around the DC frequency, therefore the limits are set between 0 Hz and $\frac{1}{4}\omega_T$, where ω_T is the transmission frequency. The upper limit for the low frequency is to ensure the bandwidth is sufficient to capture all the energy transferred to the DC component without capturing nonlinear energy present at the sub-harmonic. The general implementation of these bandwidths ensures sufficient energy is captured, whilst maintaining that the frequency components are separated and do not over lap. This is a key requirement for the study to ensure performances of the different frequencies are only attributed to the nonlinear mechanics desired.

The sensitivity of NUI to fatigue cracks is expected to increase when evaluating energy at additional frequency components. Firstly, the noise will be lower at frequencies outside of the transmission bandwidth (since noise will be generated at the transmission bandwidth), resulting in less noise energy in the nonlinearity metric. Secondly, the attenuation rates at the low frequency component are lower than at the transmission bandwidth, therefore more energy is available to measure in the diffuse field leading to increased sensitivity to nonlinear

features. The sensitivity of the single-frequency method to closed crack tips has already been established [5, 6], and in this study the low, sub-harmonic and second harmonic frequency components will be validated against the performance of the single-frequency method. Since the multi-frequency method requires two arrays, any gains in sensitivity must justify the more complicated configuration.

Another important consideration is the hard-ware filtering in the controller which has the potential to effect relatively lower frequency measurements. The array controller pre-amplification stage has a high-pass filter for removing ultrasonic energy at very low frequencies. This is expected to limit the nonlinear energy captured up to the cut-off of the filter, consequentially effecting the sensitivity of the multi-frequency method when detecting lower frequency components.

4.3 Experimental procedure

For this study, two types of fatigue samples will be tested: 3 point-bend (3PB) test samples and compact tension (CT) specimens. Using both methods of fatigue crack growth, samples of varying geometries and nonlinear features are produced. The 3PB samples were approximately 423 mm x 76 mm and 31.5 mm aluminium samples with initial starter notches machined in the centre of the sample via electrical discharge machining (EDM). Using the INSTRON 8872 hydraulic test machine a vertical fatigue crack was grown through the 3-point bending (as seen in Fig. 4.1). The loading varied sinusoidally from a minimum force of 1 kN and a maximum force 18 kN. The aluminium CT specimens were prepared following the E647 ATSM (American Standard of Test Materials) using a INSTRON 8800 hydraulic testing machine (as discussed in full in Appendix C). An initial starter notch was produced via EDM in the centre of the specimen to produce a stress concentration.

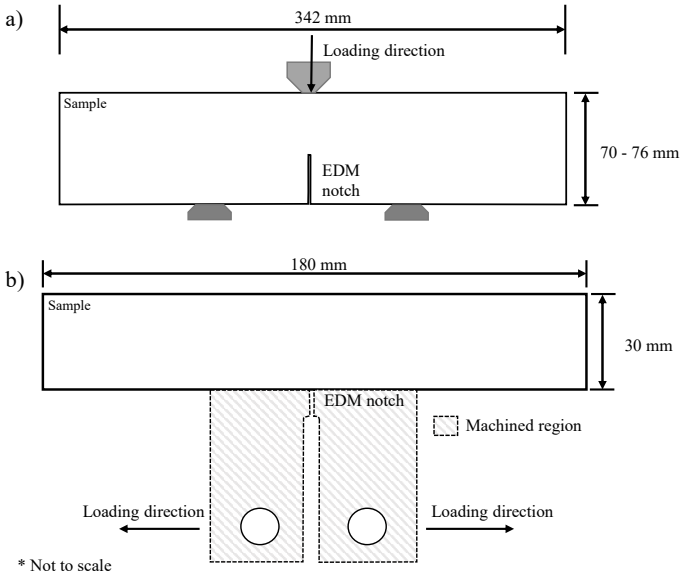

FIGURE 4.1: Sample drawings for: (a) 3PB specimens and (b) CT specimens.

All nonlinear experiments were facilitated using a Verasonics 128 element array controller (with a Hypertronics connector) with 5 Imasonic 64 element arrays with the following nominal centre frequencies: 1, 2.5, 5, 10 and 15 MHz (array specifications are presented below in Tab. 4.1). For each experiment two 64 elements arrays were connected to the controller, channels 1-64 were used for transmitting and receiving, whilst channels 65-128 were used for receiving only.

Centre frequency (MHz)	No. of El. (mm)	El. width (mm)	El. pitch (mm)
1	64	15	1.5
2.5	64	15	0.5
5	64	10	0.6
10	64	10	0.3
15	64	n/a	0.21

TABLE 4.1: Phased array specifications used for experiments.

For this study, the experiments were conducted transmitting on 1, 2.5, 5 and 10 MHz. Generally, is expected that the higher transmission frequencies will induce more nonlinearity,

but will also be more susceptible to noise (due to higher attenuation rates). The most effective frequency will also depend on the crack tip (orientation). The reverse is expected for lower transmission frequencies. The additional frequency components (low, sub and second) were evaluated using the secondary array. For example, when transmitting at 5 MHz the energy in the received signals were analysed at <1.25, 2.5 and 10 MHz. The array with the closest nominal frequency to the frequency components was then selected to ensure increased sensitivity to the energy at the frequency. The array configuration for each transmitting and receiving frequency combination is presented in Tab. 4.2. Depending on the frequency component of interest the receiving array is set accordingly for each experiment. The notation T-R is introduced to represent the centre frequency of the transmitting array (T) and the receiving array (R) frequency respectively. The values denoted in parenthesis represent the the centre frequency of the nonlinear component to be measured in MHz.

Frequency comp.	T1	T2.5	T5	T10
Low	R1(<0.25)	R1(<0.625)	R1(<1.25)	R1(<2.5)
Sub	R1(0.5)	R1(1.25)	R2.5(2.5)	R5(5)
Fund.	R1(1)	R2.5(2.5)	R5(5)	R10 (10)
Second	R2.5(2)	R5(5)	R10(10)	R15(20)

TABLE 4.2: Array selection for transmitting (T) and receiving (R) frequency combinations. The parenthesised values are the frequency component values in MHz.

The multi-frequency method is implemented by positioning the transmitting array on the surface opposite and centred on the crack tip, as shown in 4.2(a-b). This positioning is consistent with previous studies implementing the NUI technique and successfully detecting nonlinear features [5, 6]. The receiving array for the study was positioned side-by-side as seen in Fig. 4.2. NUI does not require focusing on reception (in post-processing) meaning the exact location of the receiving array is not necessary since the relative delay laws are not required. This is advantageous for samples with single-sided access or complex geometries (i.e. undefined surfaces which are hard to determine delay laws). However, it is suggested that

the receiving array be positioned as close to the receiver or nonlinear feature as possible to ensure sufficient energy is received by the array before noise dominates.

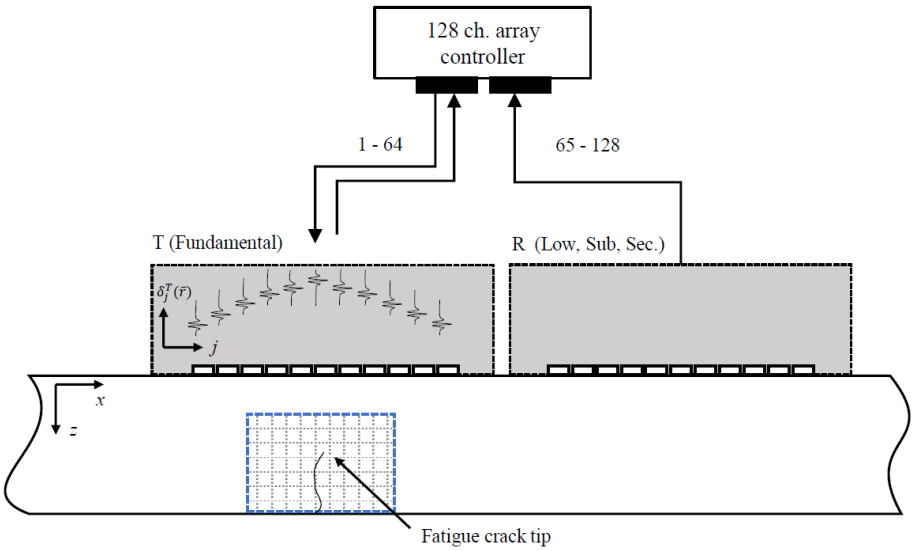

FIGURE 4.2: Dual array configuration for the multi-frequency method: a) The Verasonics channel assignment for transmitting (T) and receiving (R) using a single side access configuration.

For this study, arbitrary wave-form generation was facilitated (by the Verasonics controller) and 10 cycles was selected for the transmission signal. This was the highest cycle length available on the Verasonics controller and was selected to ensure maximum energy is transmitted into the material, and to maintain a narrow bandwidth for maximum separation of frequency components, enhancing the selectivity.

The diffuse times (t_r and T) as discussed previously are adjusted depending on the transmission frequency and the volume of the specimen, and are presented in the Tab. 4.3. These parameters are based on preliminary experiments to establish the most effective gate times in resolving the feature for each transmitting frequency and each sample type.

Trans. Frequency	t_r	T
T1	1.55	0.24
T2.5	0.4	0.20
T5	0.25	0.16
T10	0.1	0.08

TABLE 4.3: Start-time (t_r) and window length (T) for each transmission frequency used for the 3PB specimens.

4.4 Noise study

Before conducting the multi-frequency sensitivity study, it is necessary to evaluate the level of nonlinearity induced by the crack tip, giving insight into the level of nonlinearity present in each loaded sample compared with the unloaded samples. Fig. 4.3 presents the single frequency NUI (T5-R5) results for the undamaged sample and loaded samples, confirming the 3PB loading has successfully produced a detectable fatigue crack in the sample.

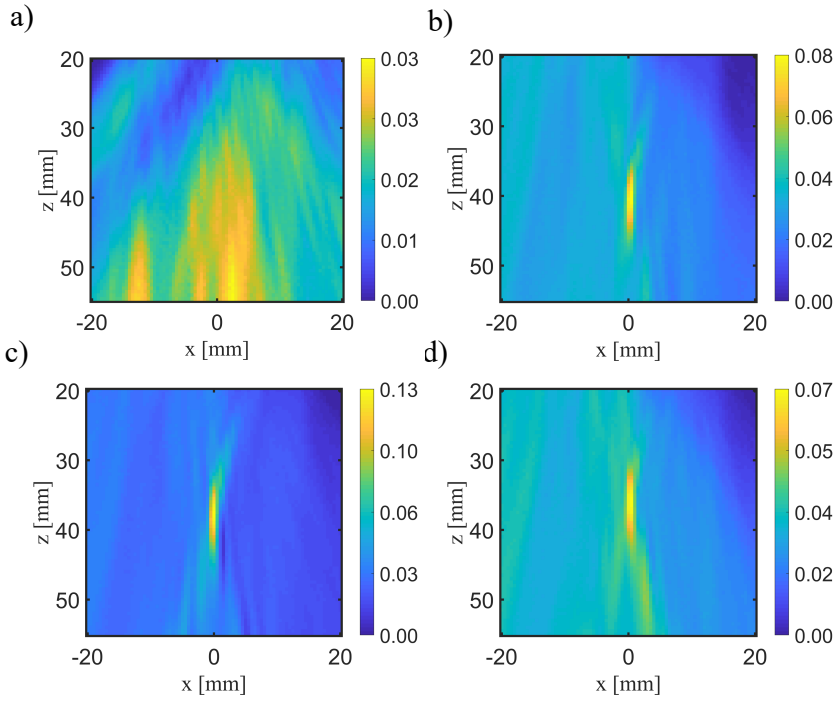

FIGURE 4.3: Nonlinear diffuse images for 3PB samples: (a) undamaged, (b) 3PB-1, (c) 3PB-2 and (d) 3PB-3.

The undamaged specimen provides insight into background noise levels and the characteristics of influential boundaries in the diffuse image. The grain structure of Aluminium contributes to energy absorption, degrading the signal and increasing the effect of incoherent noise (i.e. time varying and random) effecting SNR in the diffuse field. The grain structure will also contribute coherent noise (e.g. scattering from the grain structure) causing nonlinear noise artefacts in the images from imperfect subtraction. Therefore the background noise levels in Fig. 4.3(a) will inevitably mask some nonlinear features and set a clear detection threshold. In addition, time-variant perturbations in the system (such as variations in transmission energy between elements and environmental changes) are likely to occur between sequential and parallel acquisitions causing the subtraction of the two fields to be imperfect, contributing to the nonlinear background levels. Additionally, there is an increase in incoherent noise in the lower amplitude sequential measurements since the amplitude of the propagating waves are closer to the noise floor compared with the parallel case. This contributes further to an imperfect subtraction resulting in an increase baseline noise level in the nonlinear images. The baseline noise for all transmission frequency and frequency component configurations was assessed using the undamaged specimen and is presented in Fig. 4.4. These results display the background noise level indicating the detection threshold for each configuration (i.e. transmission and reception combination). When evaluating the performance of the multi-frequency method to known crack tips, understanding the spatial distribution of the noise within the image is to differentiate between features in the image caused by nonlinearity in the material (such as the kissing bond) and nonlinearity induced by noise.

Since the performance of the proposed multi-frequency method will be assessed against the established single frequency method, a normalised nonlinear metric is introduced to measure the relative sensitivity between frequency configurations. The nonlinear metric is normalised to the surrounding noise in the image forming a SNR metric. To determine the noise, the signal must first be defined spatially in the image, in this case the nonlinear feature (the fatigue crack)

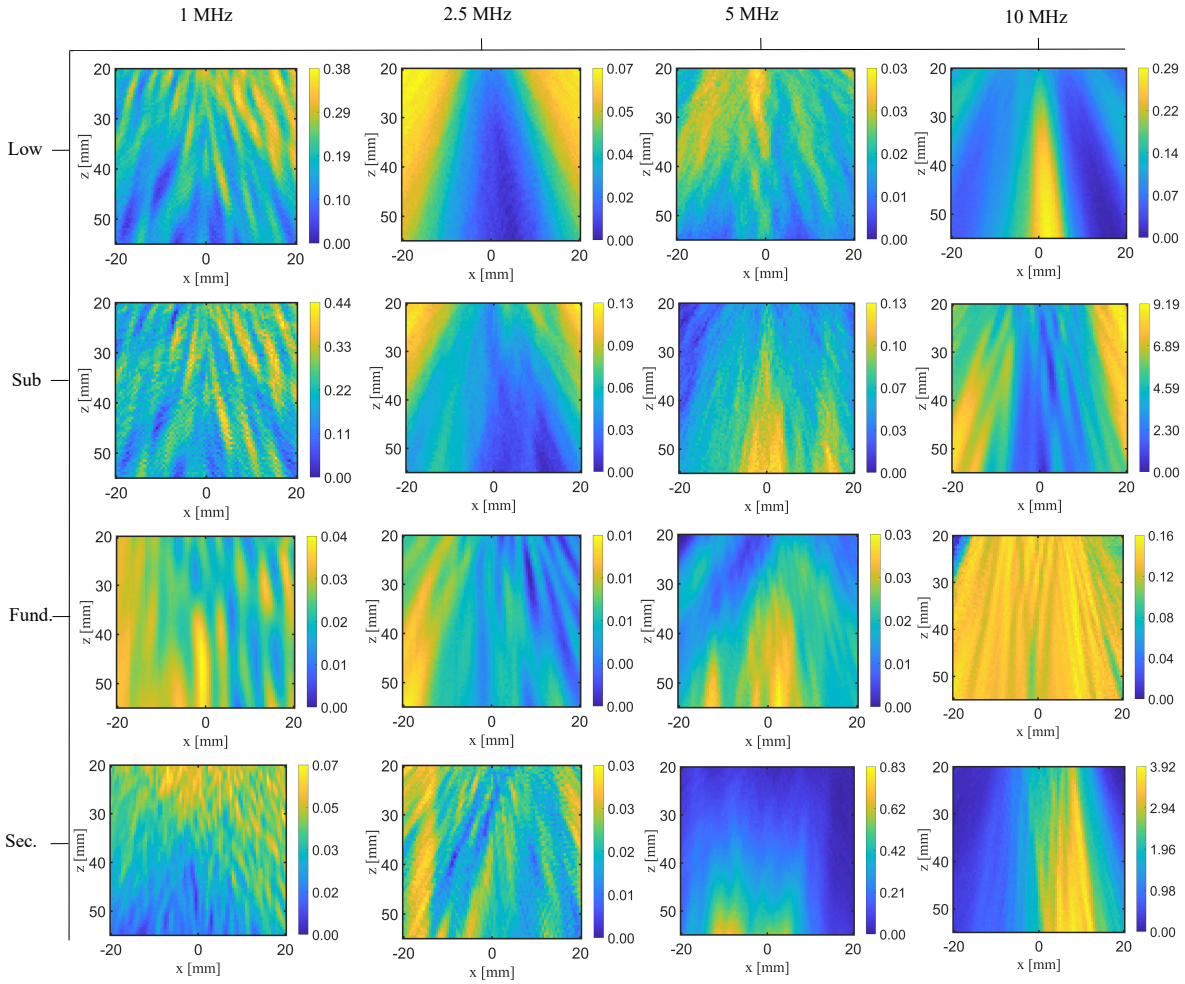

FIGURE 4.4: Nonlinear multi-frequency diffuse images displaying γ for all transmission and frequency component configurations for the undamaged sample.

must be known. The single frequency method has been validated for detecting fatigue crack growth [5,6], therefore the location of the fatigue crack will be established by the location of the maximum nonlinear feature from the T5-R5 configuration. Using the location of the nonlinear feature, a box is drawn around the feature to establish a boundary between the signal (including the point spread function of the feature) and the noise (defined as any information that is not signal), as seen in Fig. 4.5. The boundary is adapted to each NUI image and is tightly fitted to the point spread function to ensure any nonlinear energy from the crack tip is not included in the noise measurement. This ensures the measurement of noise across images is consistent. The nonlinear noise γ_n is then calculated as the rms of all the nonlinear information outside the

white box. This normalisation allows for direct comparison of the results for various frequency configurations when assessing sensitivity, which is vital considering the drastic variation in background noise between frequency configurations.

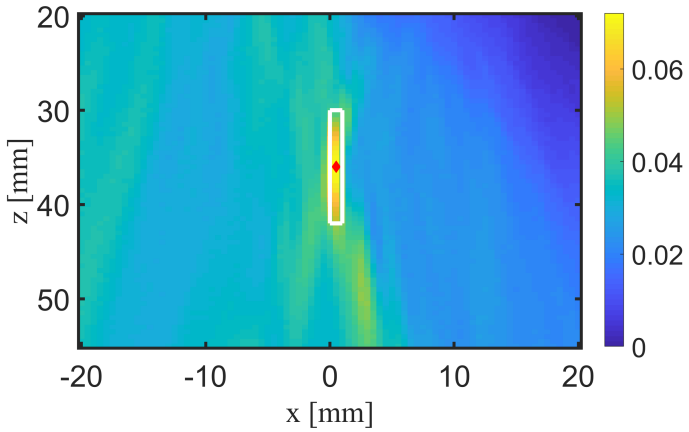

FIGURE 4.5: Diffuse imaging results displaying the nonlinearity parameter for a T5-R5 configuration on a 3PB specimen. The signal-noise boundary is indicated by the white box and the location of the nonlinear feature (i.e. the fatigue crack) is indicated by the red marker.

4.5 Sensitivity study

4.5.1 High nonlinearity features

The first consideration is the performance of the fundamental frequency component for different transmission frequencies since the excitation of the fatigue crack at different frequencies will have a significant influence on the sensitivity of the reception frequency components. It is expected that as the transmission frequency increases, nonlinearity at the focal point will be higher, increasing the energy lost from the fundamental subsequently increasing the energy measured in the nonlinearity metric. However, an increased transmission frequency will experience higher attenuation rates, accelerating the degradation of the signal, thus reducing the relative losses between the sequential and parallel fields, ultimately reducing sensitivity. It

is expected that varying excitation amplitudes will also contribute to variations in performance across transmission frequencies.

The results for 3PB-1 specimen are presented in Fig. 4.6, where the images represent γ/γ_n and are plotted for each transmission frequency and receiving frequency component. It is clear that the fundamental component when transmitting at 1 MHz is the most sensitive to the fatigue crack, by approximately a factor of 2 compared with the transmission at 2.5 MHz and 5 MHz. Therefore it can be assumed the effects of attenuation at higher frequencies significantly reduces the nonlinear energy received by the array at the transmission frequency, despite the increased nonlinear energy induced by the higher transmission frequency. Despite reduced nonlinearity excitation at 1 MHz the relatively lower attenuation rate facilitates more nonlinear information to be captured. It is also possible that the crack tip is more sensitive to a 1 MHz excitation causing a higher nonlinear response, and is therefore a feature of the crack tip as well as the transmission frequency.

During a 5 MHz transmission the sensitivity is increased when evaluating the energy at low and second harmonic components by a factor of 6 and 4 respectively, and the sub-harmonic component has reduced in sensitivity. The increased sensitivity at the low frequency component is attributed to the reduced levels of attenuation, meaning more nonlinear energy is received at the array. The increased sensitivity at the second harmonic is potentially caused by a significant reduction in noise outside the transmission bandwidth, despite significant loss in energy from higher rates of a attenuation. Similar trends are reflected when transmitting at 2.5 MHz, the low frequency component and second harmonic images show an increase sensitivity by approximately a factor of 2, while the sub-harmonic sensitivity has decreased. When transmitting at 1 MHz, the second harmonic component has increased sensitivity to the crack tip compared with the fundamental by a factor of approximately 2. However, at the low and sub-harmonic components only noise is present in the image meaning the crack tip is

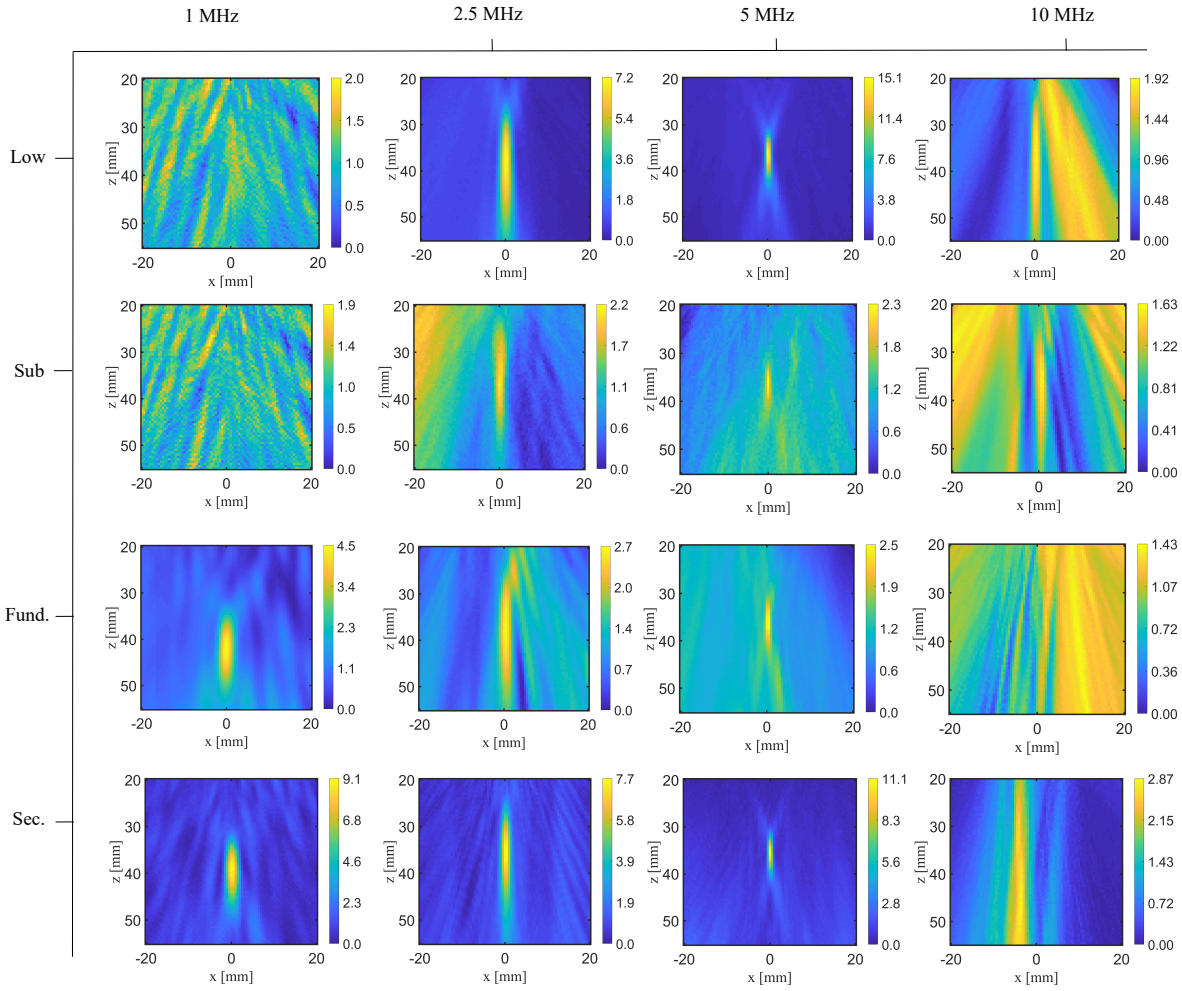

FIGURE 4.6: Nonlinear diffuse multi-frequency images for 3PB-3 presenting a noise normalised nonlinear metric γ/γ_n for transmission frequencies: 1, 2.5, 5 and 10 MHz.

undetectable.

When transmitting at 5 MHz for all the 3PB samples (see Fig. 4.7), there is consistent increased sensitivity at the low harmonic by a factor of 5 and 3 for samples 3PB-1 and 3PB-2 respectively. The improvement in sensitivity is also consistent at the second harmonic where there is an increase sensitivity of 4 and 3 for samples 3PB-1 and 3PB-2 respectively. This confirms the increased sensitivity at these additional frequency components is consistent across multiple nonlinear features.

The results transmitting at 2.5 MHz in all samples (presented in Fig. 4.8) display an increase

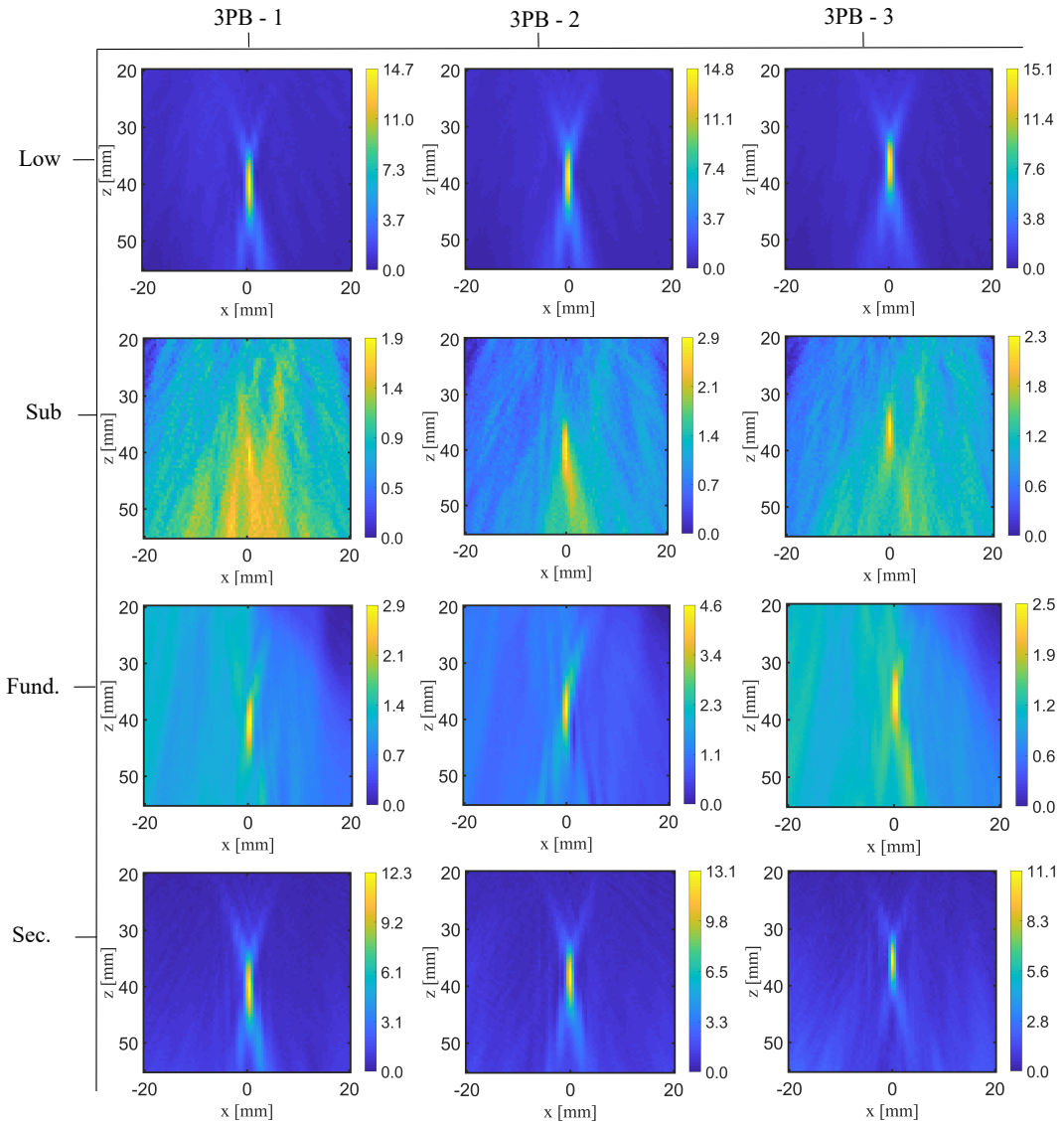

FIGURE 4.7: Nonlinear diffuse multi-frequency images for specimens 3PB-1:3 transmitting at 5 MHz. The noise normalised nonlinear metric γ/γ_n for each receiving frequency component

in sensitivity at the second harmonic for all the nonlinear features by factor of 3 and 7 for samples 3PB-2:3 and 3PB-1 respectively. Despite higher rates of attenuation at the second harmonic component the sensitivity has improved, indicating there is significantly less noise outside of the transmission bandwidth. There is no improvement at the low frequency component for samples 3PB-1:2, where unevenly distributed noise is contaminating the metric. This noise is suspected to be caused by the hardware high-pass filtering in the controller, reducing the ultrasonic energy at lower frequencies. This is also observed at the sub-harmonic component for samples 3PB-1:3, indicating that that high-pass filtering is still reducing the ultrasonic energy up to approximately 1.25 MHz (the sub-harmonic frequency).

When transmitting at 1 MHz the fundamental image shows high sensitivity to the crack tip, which suggests significant energy is moving away from the fundamental component to additional frequencies. However, the sensitivity at the low and sub-harmonic frequency components has reduced significantly and is dominated by spatially distributed noise consistent with the baseline noise measurements in Fig. 4.4. It can be inferred that the poor detection is caused by the hardware filtering suppressing the relatively lower nonlinear amplitudes at these frequencies meaning only hardware noise is being captured. The second harmonic does show an increase in sensitivity for 2 of the nonlinear features compared with the results for the fundamental but is not consistent for all the specimens.

For a 10 MHz transmission cycle the influence of noise across all the frequency components for all nonlinear features is significant, and shows no detection at the sub, fundamental and second harmonic components. It can be assumed that this is due to degradation of nonlinear energy caused by higher attenuation rates meaning predominately random noise and low amplitude nonlinear energy is being captured by the array. There is some sensitivity in the low frequency images, however noise is still dominating the metric meaning the detectability is low.

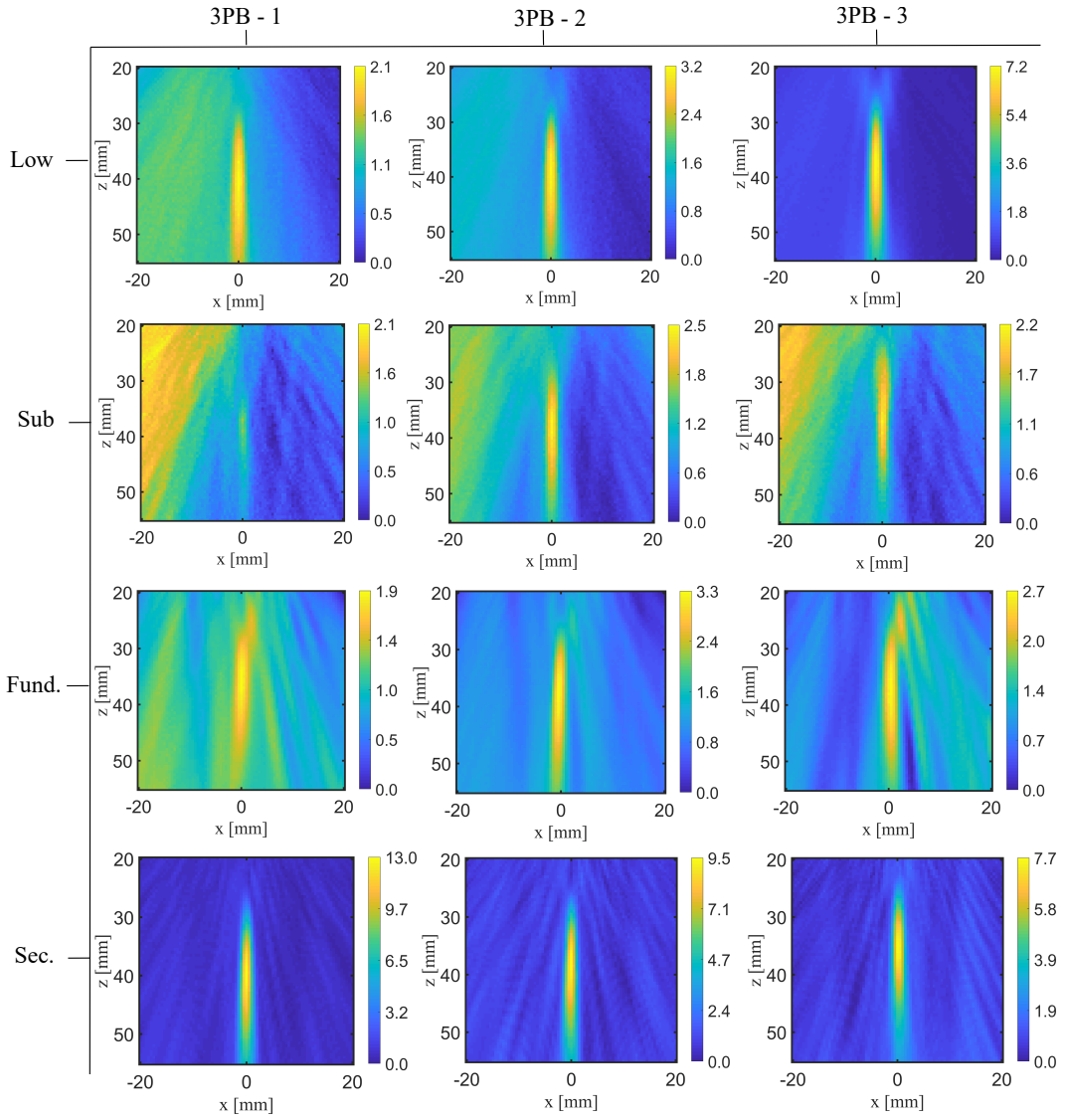

FIGURE 4.8: Nonlinear diffuse multi-frequency images for specimens 3PB-1:3 transmitting at 2.5 MHz. The noise normalised nonlinear metric γ/γ_n for each receiving frequency component.

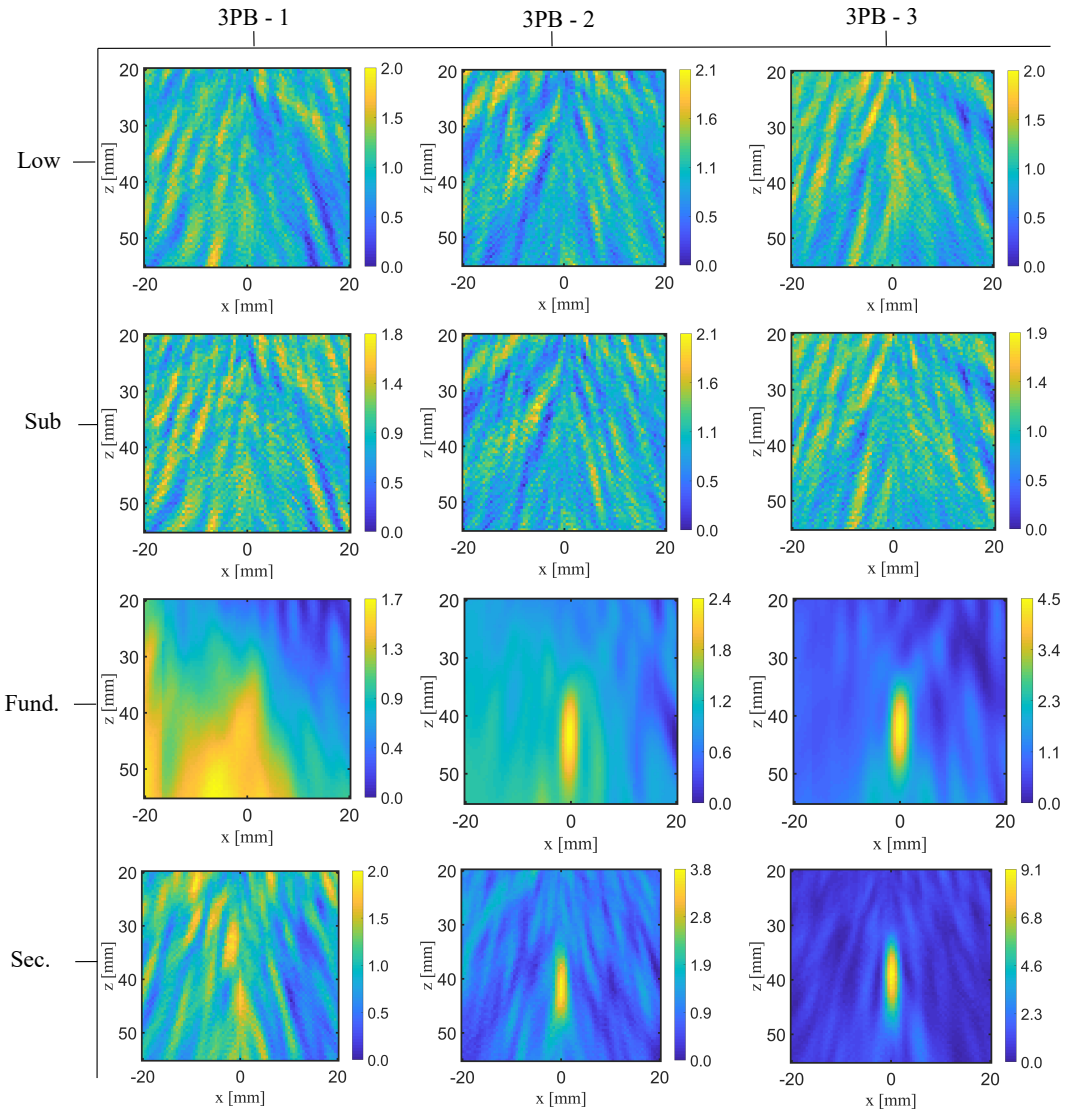

FIGURE 4.9: Nonlinear diffuse multi-frequency images for specimens 3PB-1:3 transmitting at 1 MHz displaying the noise normalised nonlinear metric γ/γ_n for each receiving frequency component.

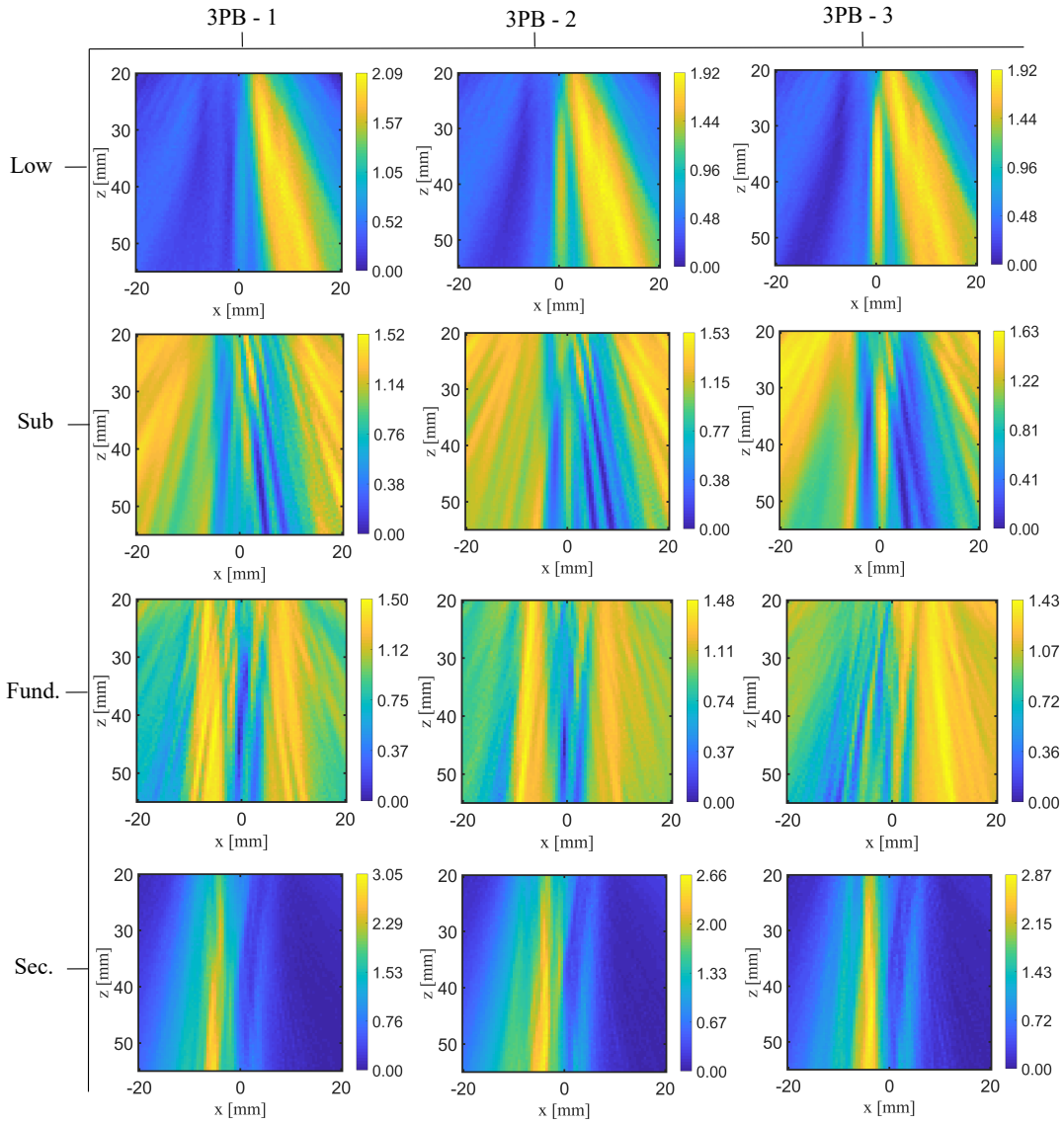

FIGURE 4.10: Nonlinear diffuse multi-frequency images for specimens 3PB-1:3 transmitting at 10 MHz displaying the noise normalised nonlinear metric γ/γ_n for each receiving frequency component.

Overall, the most sensitive detection method is a 5 MHz transmission frequency evaluating energy at the low and second harmonic components. The increased performance using this configuration is attributed to two processes. Firstly, the increased nonlinearity induced by a higher transmission frequency meaning more energy is transferred away from the transmission bandwidth, increasing the detectability of the feature. Secondly, an increase in reception sensitivity at the additional harmonic components caused by more energy being received at those frequencies. In the case of the low frequency component, as the nonlinear energy propagates through the materials after focusing, the lower frequency nonlinear energy experiences lower attenuation rates (compared with the fundamental) meaning more energy at this frequency is captured. The increased sensitivity at the second harmonic is due to reduced noise outside of the transmission bandwidth, allowing for nonlinear energy to be captured despite the effects of increased attenuation.

4.5.2 Low nonlinearity features

The previous study validated the multi-frequency method for detecting fatigue cracks grown using the 3PB method, in this section the efficacy of this method will be evaluated in detecting fatigue cracks in CT specimens. This method of growing fatigue has shown to produce crack tips with lower acoustic nonlinearity, see Fig. 4.11, where the the nonlinearity parameter for the CT samples is smaller by a factor of 10 compared with 3PB specimens. Another important observation is that the maximum nonlinear feature noise in the undamaged sample (which represents the baseline noise floor), is higher than the loaded samples, implying no crack tip has been detected using the current single frequency method (T5-R5) configuration. Therefore it is desirable to see if the feature is detectable at alternative frequency components, since the feature is arguably undetectable relative to the background noise.

The detectability of features when operating at relatively lower and higher frequencies has

shown to decrease due to a number of influential factors, therefore only the 5 MHz transmission will be evaluated. For the lower volume CT specimens the start gate-time, t_r, and window length, T, are both set to 0.075 ms to ensure the wave-field has homogenised before capturing data and ensure random noise energy is not considered in the metric.

The results for the 5 MHz transmission are presented in Fig. 4.12 and confirms that the sub-harmonic component and the second harmonic method have no sensitivity towards all the features. Sensitivity is observed at the low frequency component, and most notably is able to resolve the location of the crack tip, showing a clear offset from the back-wall at 30 mm. This shows a clear increase in sensitivity compared with the fundamental which is unable to locate the crack. This indicates that the incident wave does in fact excite the nonlinearity at the focal point and cause energy to be transferred, however the reduction in energy from the fundamental is so small that detectability at the fundamental is limited. The sensitivity to the crack tip at the low component is once again attributed to the lower rates of attenuation meaning the low frequency component is more measurable in the diffuse field than the loss from the fundamental component. Once again, it is also possible that the increased sensitivity is a function of the crack tip, causing an increase in sensitivity for a given transmission frequency.

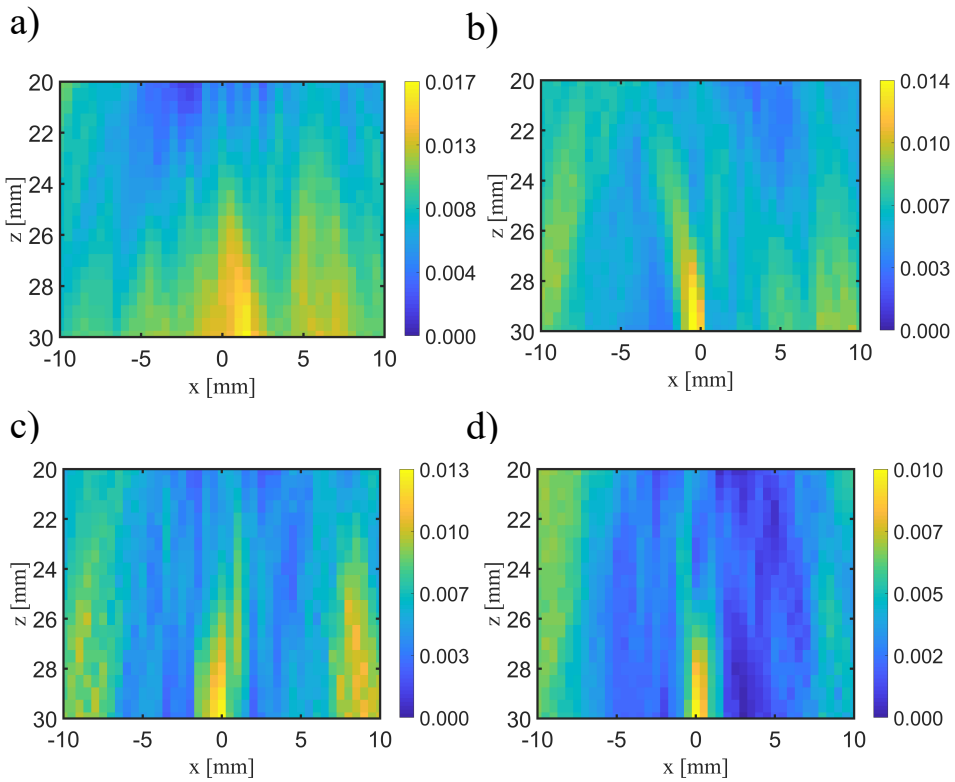

FIGURE 4.11: Nonlinear diffuse images for CT samples transmitting at 5 MHz and receiving at the fundamental: (a) undamaged, (b) CT-B, (c) CT-C and (d) CT-D.

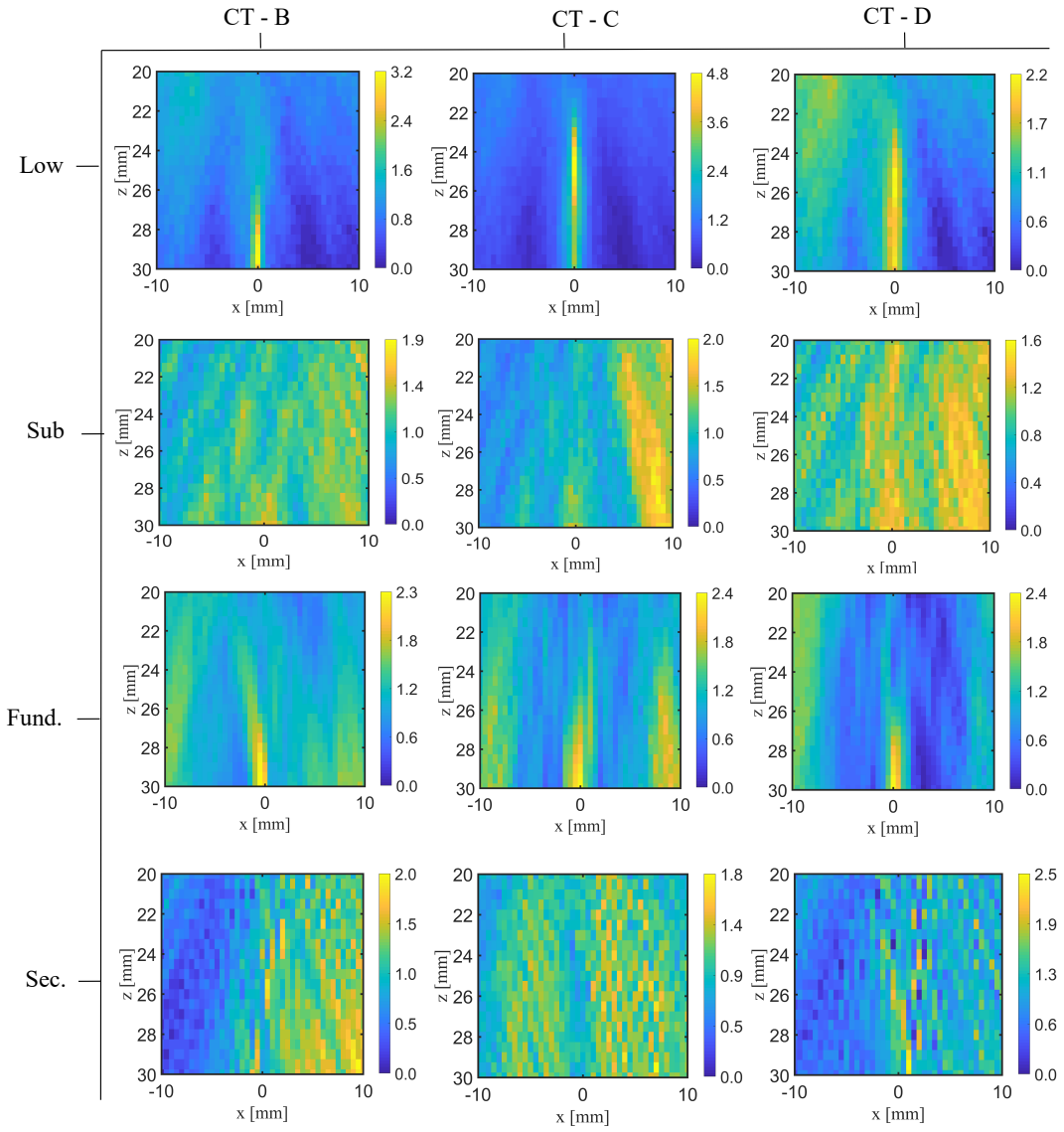

FIGURE 4.12: Nonlinear diffuse multifrequency images for the CT specimens transmitting at 5 MHz. The noise normalised nonlinear metric γ/γ_n for each receiving frequency component.

4.6 Conclusion

A multi-frequency adaptation of the current NUI method has been proposed to effectively detect fatigue cracks in two test specimen types containing a variety of nonlinear features. The proposed technique has displayed an increase in sensitivity by a factor of 4 and 6 compared with

the current single frequency method for a T5-R1 and T5-R10 frequency combination on the 3PB samples, displaying significant benefits to this dual array multi-frequency configuration. Only the T5-R1 dual configuration can detect the relatively lower nonlinearity in the CT specimens. The T5-R10 configuration shows no detection of nonlinearity, and is attributed to minimal second harmonic nonlinear energy being generated as well as increased attenuation at this harmonic, resulting in the capture of noise. The limitations of low frequency transmission are highlighted and are associated with the suppression of nonlinear energy via the hardware filter used in the instrumentation. Reduced sensitivity in higher transmission frequencies is observed and are associated with higher rates of attenuation reducing the nonlinear energy received and increasing noise captured. In addition, low levels of nonlinearity transparent to the single frequency method have been detected using a T5-R1 configuration, showing significant benefits in sensitivity for relatively low nonlinear features. Overall, the multi-frequency method has been able to increase the sensitivity of the current NUI method by evaluating the nonlinear energy contributions at the bandwidth frequency and the second harmonic. The increased sensitivity of the NUI method is a step closer towards resolving classical forms of nonlinearity such as dislocations.

Chapter 5

Diffuse Phase Imaging

The previous chapter investigated crack tip detectability using a spectrographic nonlinear ultrasonic diffuse energy imaging (NUI) technique by isolating various nonlinear frequency components, and evaluating the energy at these frequencies caused by varying nonlinear mechanisms. This chapter investigates crack tip detectability by evaluating the change in phase induced when an ultrasonic wave is incident with a crack interface, measuring the change in phase between the parallel and sequential fields. When the focused ultrasonic wave is incident with a kissing bond (i.e. a fatigue crack) the mechanical contact-acoustic nonlinearity (CAN) that occurs causes a phase shift in the signals. This mechanism induces ultrasonic nonlinearity causing a change in phase, which can be used to spatially map nonlinearity, localising CAN (crack tips) within a material. This is analogous to the acousto-elastic effect where a local stress change induces a variation in sound velocities causing a phase change in the ultrasonic signals, and have been theoretically established [29, 69, 70]. Therefore, when an ultrasonic wave experiences a stress change due to non-classical nonlinearity (a crack-tip), a variation in sound velocity can be expected and therefore a shift in phase.

Since a phase metric would not be associated with energy, the metric is expected to be less reliant on a diffuse field and therefore more effective in resolving crack tips in larger

geometries. This study implements a linear regression to the phase data, where the gradient and offset of the fitted line are used as the phase diffuse metrics for each focal point.

5.1 Sequential and parallel fields

The diffuse phase imaging method relies on the same sequential and parallel transmission implemented in the existing NUI method [5]. This investigation will evaluate the nonlinear elastic response of fatigue cracks by studying the relative phase properties of the received signals between the sequential and parallel fields. The nonlinearity induced by the opening and closing of the crack tip is referred to as contact acoustic nonlinearity (CAN), and causes the incident wave to experience varying stress states. This change in stress induces varying sound velocities which will cause the incident wave to experience a shift in phase, which is known as the acousto-elastic effect. It is possible that the plastic region around the crack tip will also contribute to this change in phase, since a change in Youngs' Modulus will alter the sound velocity. This chapter proposes an adaptation of the current diffuse energy method which assumes the phase change induced at the crack tip to be proportional to the pressure amplitude of incident wave, therefore meaning the phase change in the parallel case is expected to be N times larger than in the sequential case.

The time-domain signals for the sequential field is defined as $f_{j,k}$ for each transmit (j) and receiver (k) elements. $\delta_j(\bar{r})$ is the delay applied to the j^{th} element to focus at point $\bar{r}$. The frequency spectra of $f_{j,k}$ is defined as,

$$F_{j,k}(\omega) = \int_{t_r}^{t_r+T} f_{j,k}(t) e^{-i\omega t} dt \tag{5.1}$$

were t_r is the reception start-time and T is the end gate-time. The parallel time-domain signals are denoted $h_k(r,t)$ for signals received on element k for all focal points r in the

material. The frequency spectra of $h_k(r,t)$ is expressed as,

$$H_k(\omega) = \int_{t_r}^{t_r+T} h_k(t) e^{-i\omega t} dt. \tag{5.2}$$

The frequency spectra for the sequential transmission at the focal point $\bar{r}$ is synthetically focused during transmission in post-processing using the the focus delay laws $\delta_j^T(\bar{r})$ and is summed across all transmitting elements j, rendering the corrected frequency spectra $\hat{F}_k(\bar{r},\omega)$,

$$\hat{F}_k(\bar{r},\omega) = \sum_{j=1}^{N} F_{j,k}(\bar{r},\omega) e^{-i\omega\delta_j^T(\bar{r})} \tag{5.3}$$

A cross-correlation vector $y(\bar{r},\omega)$ is calculated by multiplying the the parallel and sequential frequency spectra, and summing across all the received signals,

$$y(\bar{r},\omega) = \mathrm{Im}\left\{ \sum_{k=1}^{N} \hat{F}_k(\bar{r},\omega) H_k^*(\bar{r},\omega) \right\} \tag{5.4}$$

where $*$ denotes the complex conjugate and the *Im* represents the imaginary component of the complex frequency spectra. Using the cross-correlation vector $y(\bar{r},\omega)$ the phase change between the parallel and sequential fields for each focal point is calculated by implementing a linear Ordinary Least Squares (OLS) regression to the data. The gradient and off-set coefficients from the regression are then used for determining the relationship in the cross-correlation vector, and therefore the phase change between the sequential and parallel fields at each focal point which represents the nonlinearity. The regression is fitted over the defined frequency bandwidth ($\frac{2}{3}\omega$ and $\frac{4}{3}\omega$). The cross-correlation vector $y(\bar{r},\omega)$ is presented in Fig. 5.1 for data captured when focused at the crack tip and in the material (where no fatigue/nonlinearity is expected to be). As expected, the higher nonlinearity at the crack tip causes the fitted line to have an increased gradient and offset coefficient compared with the material data. This

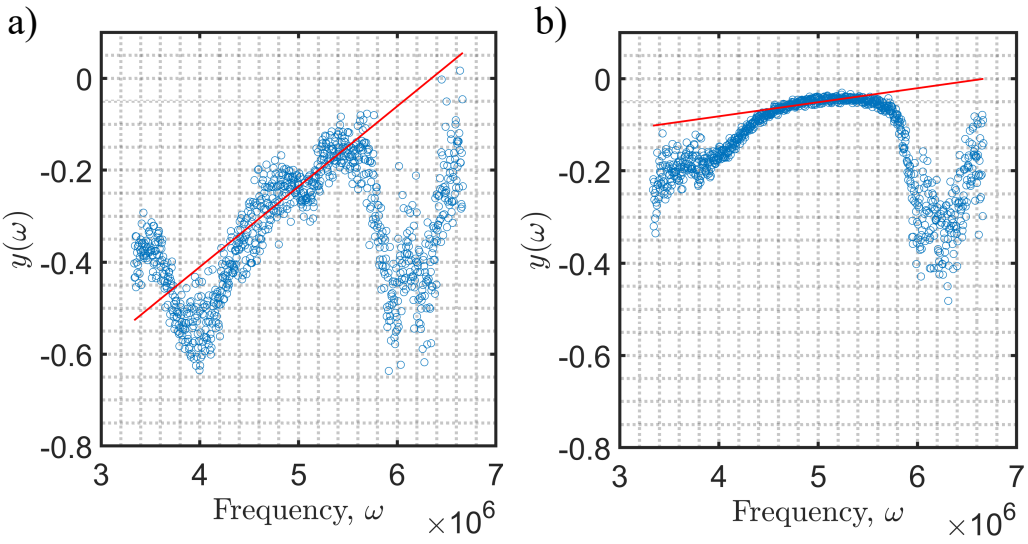

FIGURE 5.1: Cross-correlation vector $y(\bar{r},\omega)$ (blue) and fitted line (red) for data captured when focusing: (a) at the crack tip and (b) material.

preliminary analysis shows that the phase metric is sensitive to changes in nonlinearity, since the metric can differentiate between data captured in the material and at the crack tip.

It is expected that the phase metric will be less dependent on a diffuse field, since the phase is not directly associated with energy. The assumption is that the relative phase between the two fields does not rely on the nonlinearity propagating through the material and reaching a diffuse state, therefore a statistical diffuse difference between the fields is not required. The nonlinear information contained in the phase change propagating throughout the material can therefore be measured at any time. The limitation to the use of the diffuse field in larger samples caused by attenuation could therefore be resolved. With increasing propagation time, there are three main field states: coherent field, diffuse field and random noise field. During the coherent field the phase metric is expected to be more sensitive to the crack tip compared with the energy metric, since the phase metric is not associated with energy and therefore does not require the subsequent diffuse field to make an accurate measurement. In the diffuse field, the energy metric is expected to perform similarly to the phase metric, as the energy in the material has homogenised (a key requirement of the NUI method). In the later random noise

field, where the diffuse field has decayed and random noise begins to dominate, it is expected that the energy and phase metric sensitivity will reduce at the same rate, as information is suppressed by noise.

The experiments were facilitated using a Verasonics 128 element array controller (with Hypertronics connectors to independently drive two arrays) with 4 Imasonic 64 element arrays with the following nominal centre frequencies: 1, 2.5, 5 and 10 MHz (array specifications are presented in Tab. 4.1). For each experiment one 64 elements array was connected to the array controller, where only channels 1-64 were used for transmitting and receiving. The array was coupled in-contact to the top of the sample opposite to the crack tip. The efficacy of the diffuse phase method is evaluated on the 3PB samples used in the previous studies (see Section 4.3, which have been loaded to produce crack tips (i.e. known sources of nonlinearity)).

To evaluate the dependency of the diffuse field on all the metrics the time series data is captured in the earlier coherent field and then truncated in post-processing to a variety of start gate-times. This process requires the collection of long time traces, for this study a total of 12,000 time points were collected for each acquisition. The sample rate for the acquisition is 25 MHz and 50 MHz (10 MHz transmission only), which results in record lengths, $T = 0.48$ ms and $T = 0.24$ ms respectively. The truncating procedure will emulate capturing data during the multiple wave-field types: coherent, diffuse and random noise. Next, the SNR of each image is calculated using the same process described in Section 4.4 to establish how the performance of the metrics change through the different field types, and ultimately assess how sensitive the metrics are and to what extent they require a diffuse field.

5.2 Results

5.2.1 Phase images

The preliminary analysis investigates the phase images to compare them directly with the performance of the nonlinear energy metric. This was conducted by truncating the long time signals to a start gate-time for each transmission frequency, presented in Tab. 5.1. The chosen gate-times have already proven effective in resolving features in Section 4. The nonlinear images are then normalised to the noise (following the same process defined in Section 4), meaning performance of the metrics can be compared directly.

Trans. Frequency	t_r	T
T1	1.55	1.80
T2.5	0.39	0.60
T5	0.25	0.53
T10	0.10	0.25

TABLE 5.1: Start-time (t_r) and recording window length (T) for the phase study for each transmission frequency used for the 3PB specimens.

The noise normalised γ_n results are presented in Fig. 5.2, displaying improved sensitivity while transmitting at 5 MHz evaluating the phase off-set (PO) compared with the energy metric. The phase gradient (PG) also displays similar levels of sensitivity compared to the existing energy method. When transmitting at 2.5 MHz there is a small improvement in sensitivity using the PO, however this is not observed at the PG where there is no detectability. When transmitting at 10 MHz both the PO and PG show no detectability of the feature, consistent with the energy metric which is unable to detect the feature. When transmitting at 1 MHz there is no detectability using either the PO or PG.

The phase results for 3PB-1 and 3PB-2 (presented in Fig. 5.3 and 5.4) show consistent results compared with 3PB-3, confirming the PO and PG are not applicable to 1 MHz and

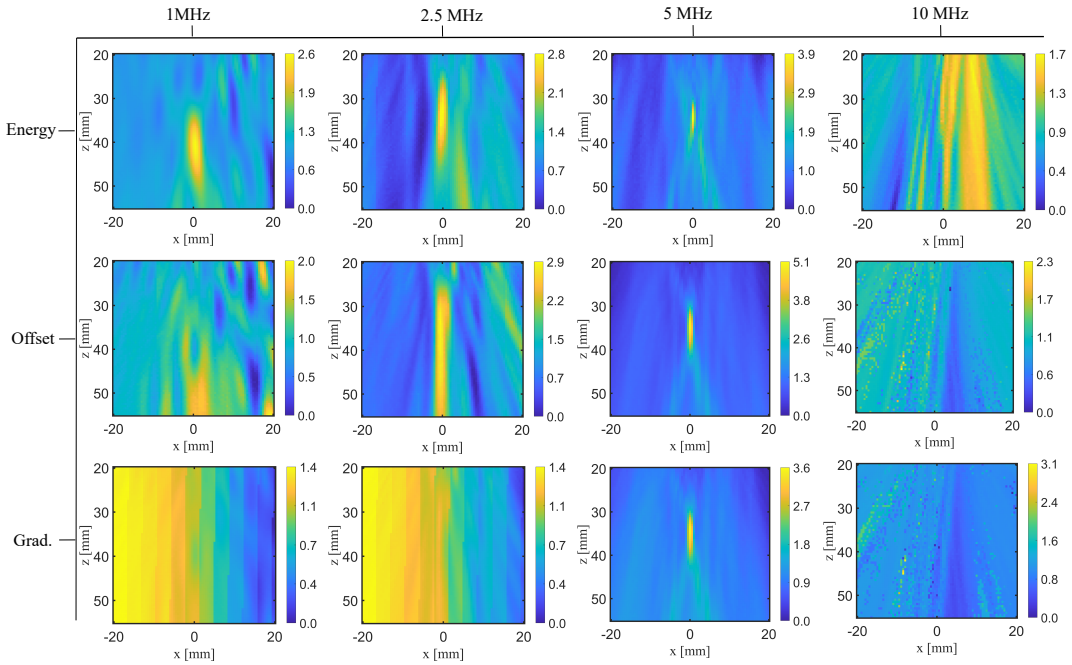

FIGURE 5.2: Nonlinear diffuse images for 3PB-3 displaying the noise normalised metric γ_n for the energy, phase offset and phase gradient metric for multiple transmission frequencies.

10 MHz transmission frequencies. The 1 MHz transmission frequency induces relatively less nonlinearity at the focal point, meaning a smaller phase change will be caused at the focal point, limiting the detectability of the feature in the phase image. At 10 MHz the relatively higher attenuation rate has caused the signal to degrade significantly, increasing the presence of random noise, reducing the nonlinear energy and phase information available to localise the fatigue crack tip above the noise floor.

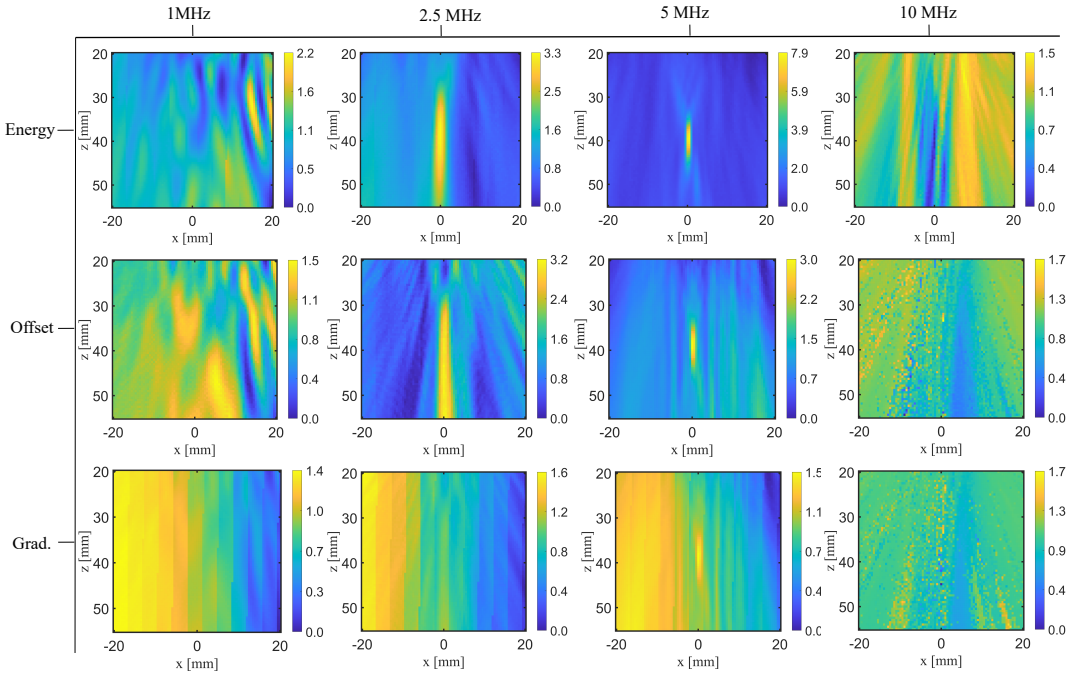

FIGURE 5.3: Nonlinear diffuse images for 3PB-1 displaying the noise normalised metric γ_n for the energy, phase offset and phase gradient metric for multiple transmission frequencies.

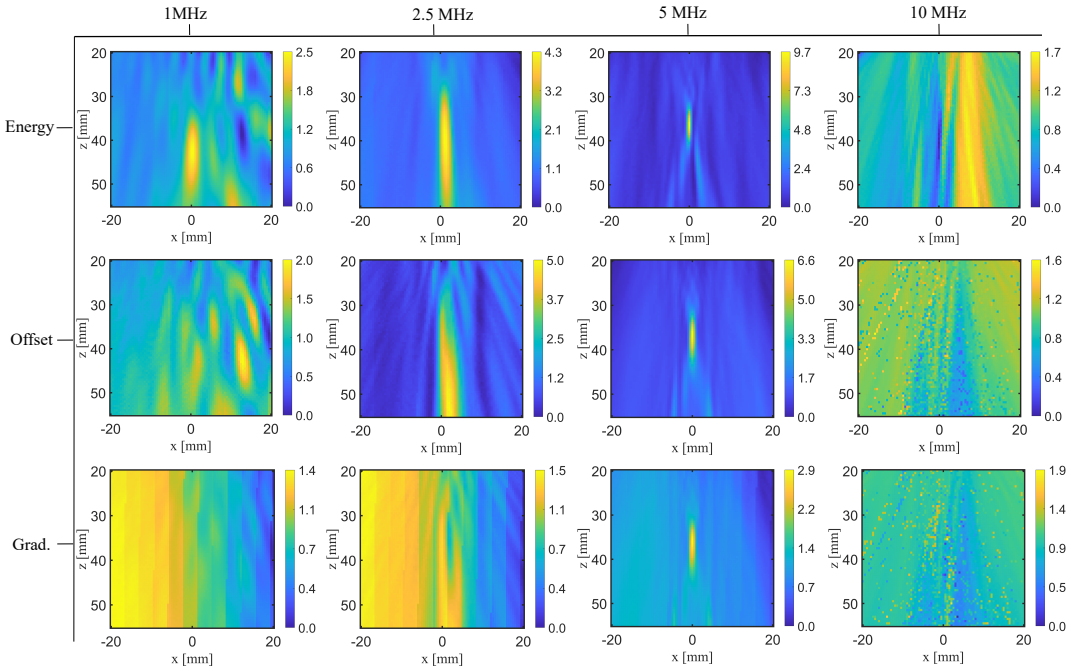

FIGURE 5.4: Nonlinear diffuse images for 3PB-2 displaying the noise normalised metric γ_n for the energy, phase offset and phase gradient metric for multiple transmission frequencies.

However, the detectability of the crack tip when transmitting at 2.5 MHz and 5 MHz has shown to provide similar if not better sensitivity in some cases compared with the energy metric. In the next Section, the sensitivity of these metrics to start gate-times will be investigated to determine whether the phase metric shows reduced sensitivity to a diffuse field, and therefore is potentially more applicable to larger geometries.

5.2.2 Start gate-time analysis

It is expected that the phase metrics are less sensitive to the diffuse field requirement since the metrics are not associated with energy and therefore do not require the wave-field energy to homogenise before capture (assuming relative phase remains consistent). To evaluate this hypothesis, the time series data is truncated in post-processing to a variety of start gate-times (t_s) to produce nonlinear images which represent nonlinear images captured in the three different wave-field conditions: coherent, diffuse and random. The 1 MHz and 10 MHz results have been excluded from this study since the phase metrics show no indication of detecting the fatigue crack tip even under ideal conditions.

The γ_{snr} for each metric using multiple start gate-times and a 5 MHz transmission is presented in Fig. 5.5, and shows that the PO and PG provide some benefits. For example, the results for 3PB-2 (presented in Fig. 5.5(b)) show that early in the coherent field both the PO and PG provide a higher sensitivity than the energy metric. As the start gate-time is increased the field becomes more diffuse the γ_{SNR} of the energy metric increases and surpasses the sensitivity of both the PO and PG, and peaks at approximately 0.25 ms. This peak in sensitivity indicates that the wave-field has homogenised and the field is now diffuse. Fig. 5.5(c) shows similar results for sample 3PB-3, where the PO and PG sensitivity is larger than the energy by a factor of 2 and 3 respectively in the coherent field. When the start gate-time is increased the sensitivity of the energy metric increases, however the PO and PG during this diffuse time

period are still more sensitive to the crack tip. Later in time, the sensitivity of all the metrics are consistent. However, the 3PB-1 results in Fig. 5.5(a) for the energy metric shows that the energy metric is more sensitive than the PO and PG for all start gate-times. This suggests that for this sample in particular the energy metric is not sensitive to the diffuse field compared to samples 3PB-2:3, since the samples are the same volume, this suggests that it is the nonlinear feature that is causing disparity in the reliance on the diffuse field.

These results can be further validated by evaluating the images of these results. The nonlinear images for 3PB-2 are presented in Fig. 5.6 transmitting at 5 MHz for coherent (0.05 ms), diffuse (0.25 ms)and random noise (0.53 ms) field start gate-times. These results confirm the benefits of the phase metrics earlier in time, showing a increase in detection of the feature in both the PO and PG over the established energy metric in the coherent field. In addition, these images confirm the relatively consistent performance across metrics during the diffuse field and reduced performance in the phase metrics in the later random noise field.

When transmitting at 2.5 MHz the PO and PG do not show any clear advantages (see Fig. 5.7(a-c)), despite the PO showing a small improvement in sensitivity for sample 3PB-2 and 3PB-3 using a 0.3 ms start gate-time. The PG is consistently less sensitive than both the PO and the energy for all start gate-times.

The inconsistent performance of the phase metrics across transmission frequency and samples could be due to increased noise caused by times series data being collected with a very early start gate-time (to be truncated in post-processing). During experimental capture the gain level will be set according to the higher amplitude coherent field (early in time), therefore the relatively lower amplitude diffuse field (after the coherent field) will not be captured using the most effective gain level. This will results in random noise dominating during the capture of the diffuse field meaning less nonlinear information is captured from the focal point, leading to significant deviations in nonlinear results.

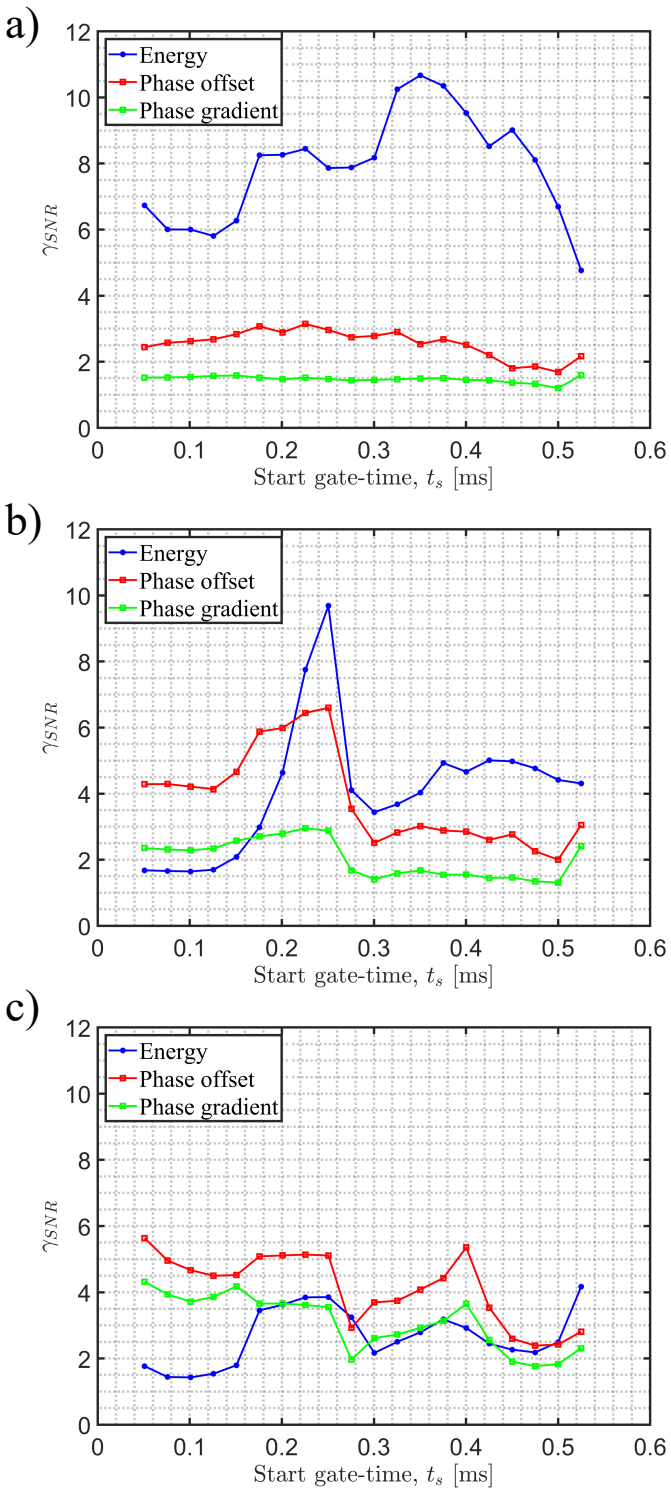

FIGURE 5.5: Nonlinear diffuse SNR, γ_{SNR} for 3PB samples transmitting at 5 MHz: (a) 3PB-1, (b) 3PB-2 and (c) 3PB-3. Both γ_{SNR} for the energy metric (blue), phase offset (red) and phase gradient (green) are plotted.

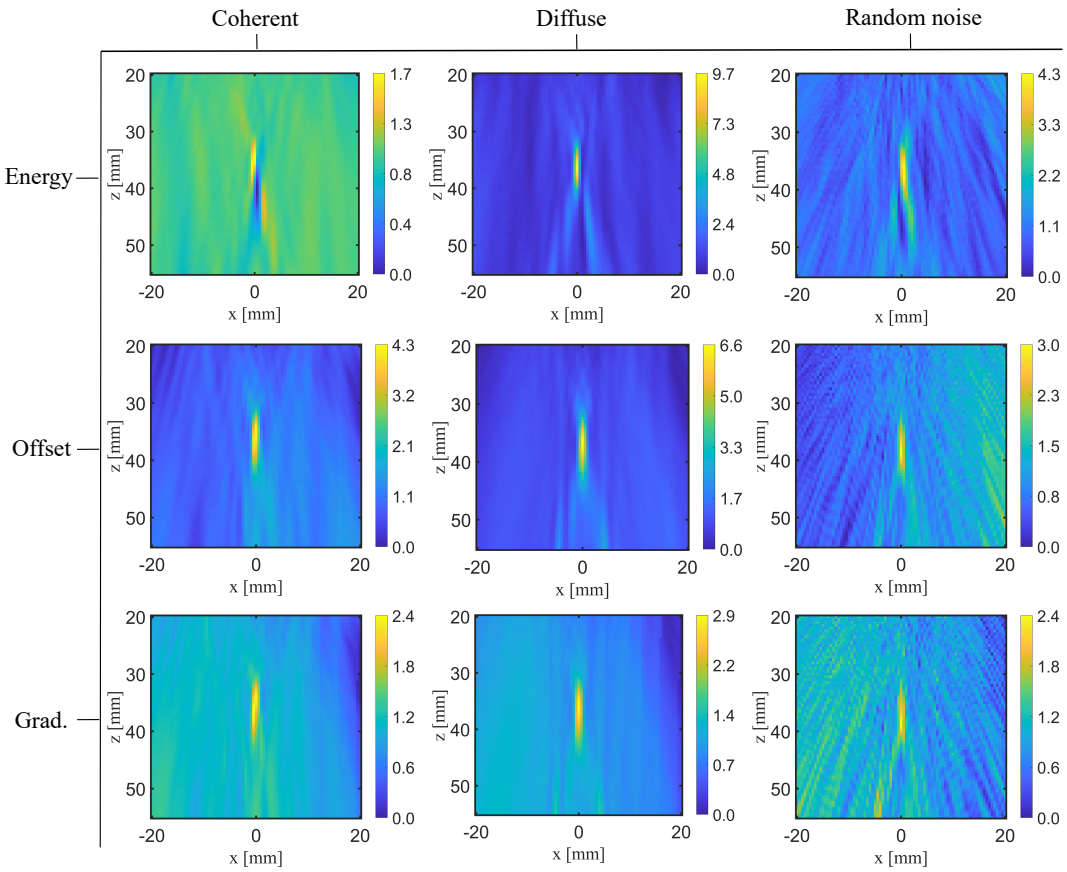

FIGURE 5.6: Nonlinear diffuse images for 3PB-2 displaying the noise normalised metric γ_n for the energy, phase offset and phase gradient metric for different start gate-times: early, medium and late.

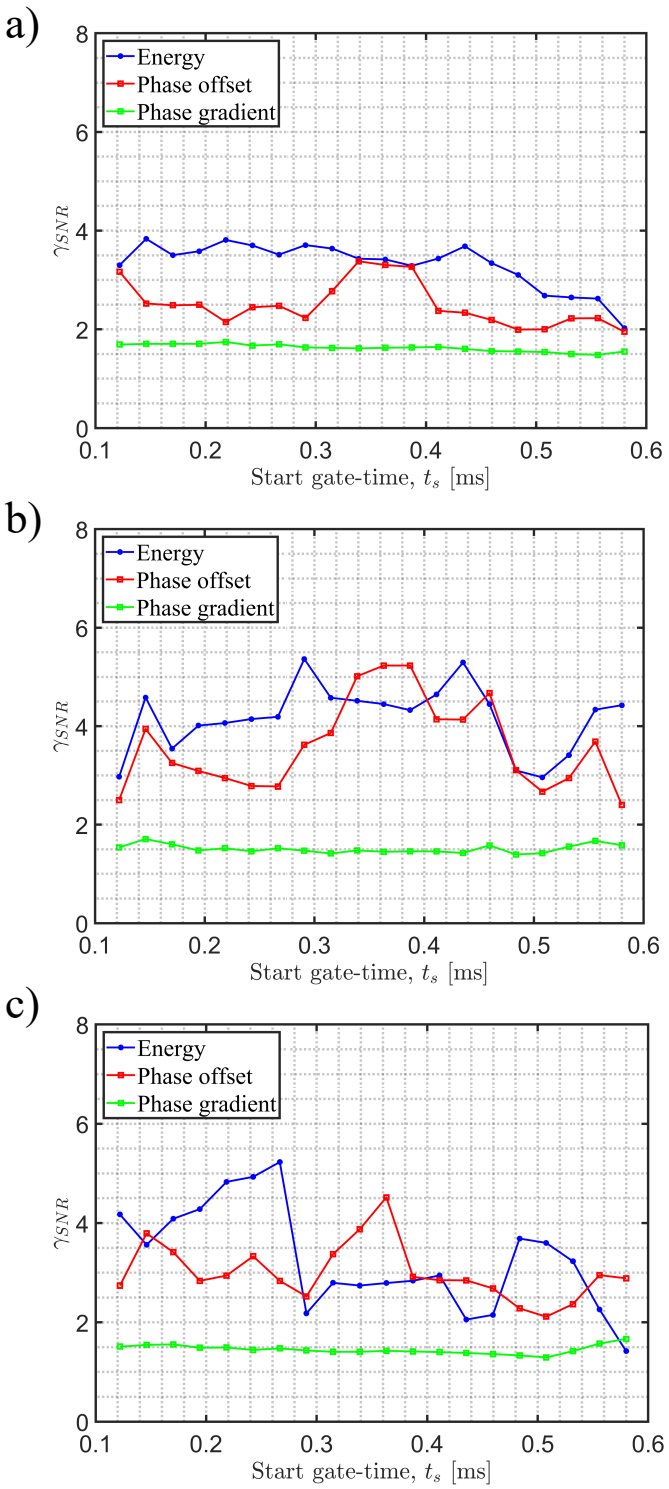

FIGURE 5.7: Nonlinear diffuse SNR, γ_{SNR} for 3PB samples transmitting at 2.5 MHz: (a) 3PB-1, (b) 3PB-2 and (c) 3PB-3. Both γ_{SNR} for the energy metric (blue), phase offset (red) and phase gradient (green) are plotted.

5.3 Conclusion

This study concludes that there are some benefits to implementing the phase metrics for detecting fatigue crack tips during the NUI process. Using a 5 MHz transmission frequency the offset and gradient phase metrics are less sensitive to the requirement for a diffuse field for some samples resulting in a higher detectability of the nonlinear feature. When transmitting at 2.5 MHz only the offset metric has been effective in resolving the feature and performs consistently with the energy metric in response to the changing start gate-time.

Further investigation into the performance of the metric using gain levels which reflect the amplitude level of the diffuse field is desirable. This would further validate the phase metric for industrial use in larger geometries. Since the phase offset can be computed along side the energy metric without serious computational demand the metric can be easily implemented in the NUI processing chain.

Chapter 6

Diffuse field characterisation

6.1 Introduction

In the previous chapters, the diffuse field time is determined through a "trial and error" process to determine the most effective start gate-time (i.e. which provides the best signal-to noise-ratio (SNR)) for detecting the known nonlinear feature in the material (the crack tip). In real life samples where the existence of a crack tip or other nonlinear features is unknown this is not possible, therefore a robust method for determining the time in which the wave-field has statistically homogenised is essential. This chapter optimises the nonlinear ultrasonic diffuse energy imaging (NUI) technique by establishing robust measures to determine the best diffuse field parameters such as start gate-time and record length.

Ensuring a diffuse field state for the NUI method is essential. Further in time, the field will be closer to the strict mathematical definition of diffuse, however the influence of noise is higher, meaning the resolution of the nonlinear feature will be lower, resulting in a degraded SNR. Hence, the time at which the receivers begin capturing, referred to as the start gate-time, is key to the accuracy of this technique. The ability to statistically determine the point in time at which the field is optimally diffuse and implement this as the start gate-time, would improve

reliability, and applicability to industry significantly. More specifically, this would increase the usefulness of this technique for real-world tests where the state of the sample is unknown. As well as the start gate-time, the end gate-time is important to minimise the effect of noise in the captured signals, since further in time random noise contaminates the signals.

The metrics of diffuse state will be tested by evaluating the performance of the NUI technique at multiple start gate-times, and will be assessed for robustness against multiple volumes, cycle lengths and transmission frequencies. The influence of random noise in the received signals will also be investigated as an indication of an appropriate end gate-time, providing the most effective record length. In addition, the repeatability of the NUI method will be investigated to establish its applicability to real industrial samples where the presence of nonlinear features are not controlled and give confidence in results.

6.2 Diffuse Field

6.2.1 Theory

The determination of a diffuse field has been of interest across a variety of research areas such as ultrasonics [71], ocean acoustics [72], room acoustics [73], seismology and structural health monitoring [74, 75]. A diffuse field is defined by Evans et al. as a wave field with evenly distributed wave energy, i.e. the amplitude and wave directivity is random throughout the field and phase is not spatially correlated [75]. This implies that evaluating the phase of the received signals from the array transducers could be used as an indication of a diffuse field.

A diffuse state is likely to occur if all boundaries in the system are diffuse reflectors, meaning the distribution of the reflected wave is not a function of the incident wave angle. In practice, this is not perfectly achievable, however a convergence in approximation will occur if the

wavelength is approximately the same size as the surface features, as the reflected wave will be scattered diffusely [75]. When studying diffuse waves in plates, Weaver et al. sawed and milled the edges of plates to increase the number of reflective boundaries. This was to aid the generation of a diffuse field in his measurements before the effects of attenuation became prevalent [76]. In some instances, a diffuse state will not be achieved due to absorption, most commonly in materials with higher absorption coefficients or in larger samples where the reflection path back to the array is further, thus leading to higher absorption. This observation will be relevant to NUI where it is required that the diffuse field is captured before the effects of attenuation reduce the signal, as this would lead to noise dominating the captured data.

Research into characterisation of diffuse fields in NDT is fairly limited, however there are investigations of diffuse fields in finite systems and poly-crystals that are applicable to NDT [71, 77–79]. The use of Green's functions to correlate with diffuse fields is investigated by Weaver [77] in a theoretical approach, asserting dependencies on the spectrum of the diffuse field and the phase of the receivers. Later work by Weaver [78] investigates a model for uniformly distributed sources in a closed system in which two correlation functions are derived to determine a diffuse field: the mean square correlator and variance [74, 79, 80]. Prior to a diffuse state is a coherent state, whereby the phase of the receivers are correlated. In a diffuse state the phase between receivers are uncorrelated, therefore it is possible to develop a phase coherence metric to determine diffusivity [75].

This paper presents an adaptation of the phase coherence metric to a phased array configuration to allow for diffuse field approximations using full matrix capture (FMC) data. This implementation allows for the measurement to be conducted with the standard nonlinear phased array configuration [5, 6].

6.2.2 Definition of metric

As described above in Section 6.2.1, a metric to determine the phase coherence of a system can be used to determine a diffuse state. Since in a diffuse field the phase of the signals will be uncorrelated [75] we can define the first derivation of the metric as a sum-square correlator, which is the relationship between the square of the sums, and the sum of the squares. For two neighbouring sources $s_1(t)$ and $s_2(t)$, the sum square correlator, $SSC(t)$, can be written as,

$$SSC(t) = \frac{((s_1(t) + s_2(t))^2}{(s_1(t)^2 + s_2(t)^2)} \tag{6.1}$$

if the values are identical (i.e. correlated) then the square of the sum will will be twice the sum of the squares, and results in the SSC being equal to two. If the signals are non-identical, then their SSC will be approximately 1.

The sum-square correlator can be adapted to a phased array FMC configuration whose dimensions are determined by t_n x N^2, where t_n is the number of time points and N is the number of transducer elements in the array. To process the FMC data a moving time window is implemented to process the received signals in segments. The phase coherence is then defined as the general sum squared over the squared sum for all transmit and receive elements over each time window T as,

$$\alpha_{ph}(t) = \frac{\sum_{j=1}^{N} \int_{T_n-\frac{\tau}{2}}^{T_n+\frac{\tau}{2}} \left(\sum_{k=1}^{N} f_{j,k}(t) \right)^2 dt}{\sum_{j=1}^{N} \sum_{k=1}^{N} \int_{T_n-\frac{\tau}{2}}^{T_n+\frac{\tau}{2}} f_{j,k}(t)^2 \ dt} \tag{6.2}$$

where $f_{j,k}$ is the time domain received signal for the j^{th} transmission element and k^{th}

receiver, τ is the temporal window length and T_n is the window number. Early in time, when the field is coherent, it is expected that the square of the sums will be approximately twice the sum of the squares. This is because the received signals are almost identical early in time, and therefore the summation of the signals which are then squared is generally twice the sum of the squares. Later in time, in the diffuse field it is expected that the square of the sum and the sum of the square will become equal because the signals are uncorrelated/random and thus not identical. This is also expected to occur in the presence of random noise where the captured data will be random and not be correlated across received signals. Previous work by Cheng [81] has investigated the application of a phase coherence metric to NUI.

Since NUI is strongly reliant on a diffuse field, the applicability of this metric can be accurately tested against the performance of the technique, which relies on a diffuse field to work. This is achieved by assessing the SNR performance of the nonlinear images for various start gate-times.

6.2.3 Nonlinearity parameter, γ

In this study, the accuracy of the metric for optimising the diffuse field will be tested against the performance of the NUI technique. For this technique we define the nonlinearity parameter, γ, as the difference in energy at the transmission frequency between the parallel and sequential firing modes. The γ parameter is calculated as the subtraction of the parallel energy, E_p, from the sequential, E_s, normalised to the sequential capture,

$$\gamma(r) = \frac{E_s(r) - E_p(r)}{E_s(r)} \tag{6.3}$$

this is calculated for each each focal point, r, in the material, resulting in a map/image of measured nonlinearity [5]. The sensitivity of this metric to a closed crack tip will be used to

test the diffuse field metric.

6.3 Repeatability

The experimental procedure for this study consists of two stages: FMC capture and NUI. The former acquires the FMC data required to compute the diffuse field metric and the latter is to form the nonlinear images (requiring FMC and parallel focusing). The data for both stages were captured using a Verasonics commercial array controller with an Imasonic 5 MHz 64-element array with an elementary pitch of 0.6 mm, a configuration which has already been proved successful for both experimental stages [5, 6, 63]. For both stages 10,000 sample points and a sampling frequency of 25 x 10^6 Hz were selected. A cycle length of 4 was chosen to ensure that sufficient energy was transmitted into the system, thus increasing the dynamic range of the nonlinear feature, but no longer to ensure that the spatial resolution of the crack tip was not reduced.

Before investigating the optimization of NUI, it is important to determine what is the natural variability of the nonlinear measurements to ensure that any variation in measurements can be determined as real variability. The repeatability of NUI is limited by two main factors: coupling gel and the warm up time of the controller. When the array is coupled to the material using a static load and coupling gel it takes some time for the gel to cover the whole surface area of the region between the material and the array, meaning there is variation in energy being efficiently transmitted into the material over this period of time. When the array controller is first turned on the output energy varies until the array controller is warmed up. Therefore, it is required that the array controller reaches a static state where the output energy is constant. Both these factors contribute to a variation in energy being transmitted into the material and therefore will significantly effect the nonlinear information received by the array, effecting the repeatability of these nonlinear experiments. This repeatability study was conducted on the

high volume sample (see Fig. 6.2 and Tab. 6.1 for specifications), which has been three-point loaded to produce a known closed crack tip (a strong nonlinear source).

In order to assess the effect of the coupling gel on repeatability, the array controller was turned on for 24 hours before conducting the study. This was to ensure that the variation in transmission energy is only caused by the coupling gel and not the output energy variation from the array controller. The variation of the mean nonlinear parameter, $\bar{\gamma}$, was investigated over a period of 135 minutes (with each acquisition taking approximately 3 minutes) and is displayed in Fig. 6.1(a). From these results it is clear that the variation in $\bar{\gamma}$ is consistent throughout the measurements. The change in $\bar{\gamma}$ can therefore be associated with the natural variation of the measurement, since the settling of the coupling gel shows no improvement or trend change in sensitivity. Therefore it can be determined that a time delay is not required for the coupling to settle.

To establish the influence of the controller being warmed up the controller was turned off 24 hours before the experiment. The sample was then coupled 10 minutes before the study to ensure any deviation in $\bar{\gamma}$ is caused only by the warming up of the controller (10 minutes was based on a trial and error preliminary study). The results from the warm up experiment are displayed in Fig. 6.1(b). It is clear that after approximately 10 minutes $\bar{\gamma}$ stabilises. During the first 10 minutes of experiments the mean γ reduces by approximately 20%. This reduction tells us that it is necessary to allow the controller to warm up before conducting these experiments to achieve reliable results.

After implementing the warm up time delay to ensure repeatability, the effect of re-coupling was studied. For this experiment the array was re-coupled with new coupling to the material for each capture using enough coupling gel to cover the surface of all transducers in the array between every measurement. The same quantity of coupling gel was used for each measurement to ensure the coupling conditions were kept consistent. The array was held in

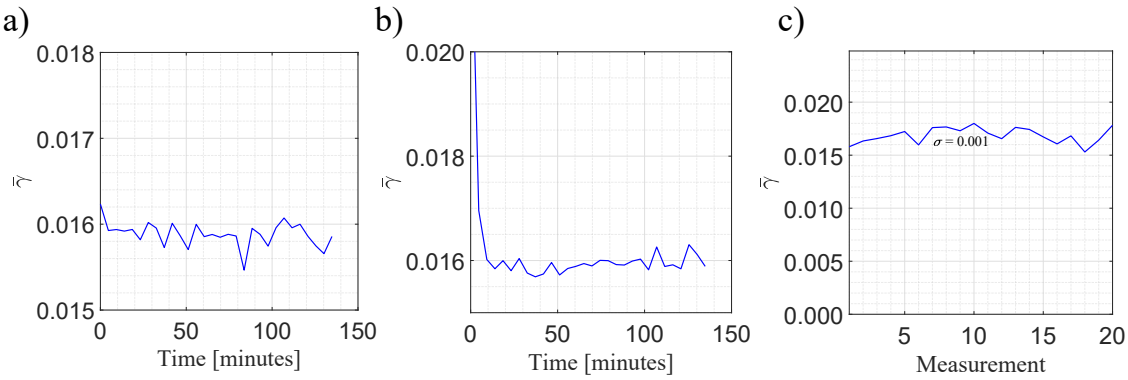

FIGURE 6.1: Repeatability results using the high volume sample displaying the mean nonlinearity parameter $\bar{\gamma}$ for the following studies: (a) coupling, (b) warm up and (c) re-coupling.

position using a fixed mass of 2 kg to ensure a consistent coupling force. Before this study the array controller was turned on 10 minutes before the experiment to reach a static state.

Fig. 6.1(c) displays the variation $\bar{\gamma}$ over 20 experiments. The variation $\bar{\gamma}$ values over the all the measurements is very low (standard deviation, $\sigma = 0.001$). This low standard deviation indicates a small degree of variation in the nonlinear parameter for the maximum values (i.e. the crack tip). The remaining variation in the measurements is potentially caused by a slight change in the position of the array relative to the crack tip between couplings, meaning varying levels of nonlinearity is excited. The confirmation of low variability in the nonlinear measurements means these experimental approaches were implemented throughout the rest of the study to ensure repeatability of results.

6.4 Testing of phase coherence metric

6.4.1 Configuration

Having shown how to make repeatable results, how the diffuse field may be characterised with the defined metric will now be studied. It is expected that the time taken to reach a diffuse field is dependent on volume, geometry and cycle length. The cycle length is defined

as the number of cycles used as the pulse transmission signal to excite the material. It is also expected that the temporal window length τ will have a significant effect on the convergence of the metric. A long window will give a better approximation of the diffuse field (and therefore the convergence will be easier to detect), however if the window length is too long then random noise will significantly contaminate the metric.

Since the NUI technique can potentially be implemented on any geometry, it is vital that this metric can statistically determine the optimum time for a diffuse field to form for various volumes. To assess the metrics sensitivity to volume change, a 3-point bend (3PB) sample was machined down to various volumes (see Fig. 6.2 and Tab. 6.1 for specifications). By machining the sample, this means the nonlinear feature is exactly the same across all studies, therefore the only change to the system is the volume and geometry. The SNR values from the nonlinear feature across multiple gate times will be used to test the metric as the presence of a nonlinear crack tip is known.

The volume alteration study was conducted on an Aluminium (2014T6, c_l = 6000 ms^{-1}) fabricated surface breaking crack specimen, 3-point loaded according to ASTM standard E1820. This sample was machined down to multiple volumes as illustrated in Fig. 6.2. The volumes from each machining stage are presented in Table 6.1. For each stage of machining the nonlinear experiments and FMC data captures were conducted.

Investigation into the influence of cycle lengths (i.e. the number of cycles used in a transmission pulse during FMC) on this metric has also been carried out, as often various input cycles are used in nonlinear phased array imaging. It is assumed that the change in energy transmitted into the system will influence the time taken to reach a diffuse field, and therefore that the convergence of the metric should be dependent of this change in transmission energy.

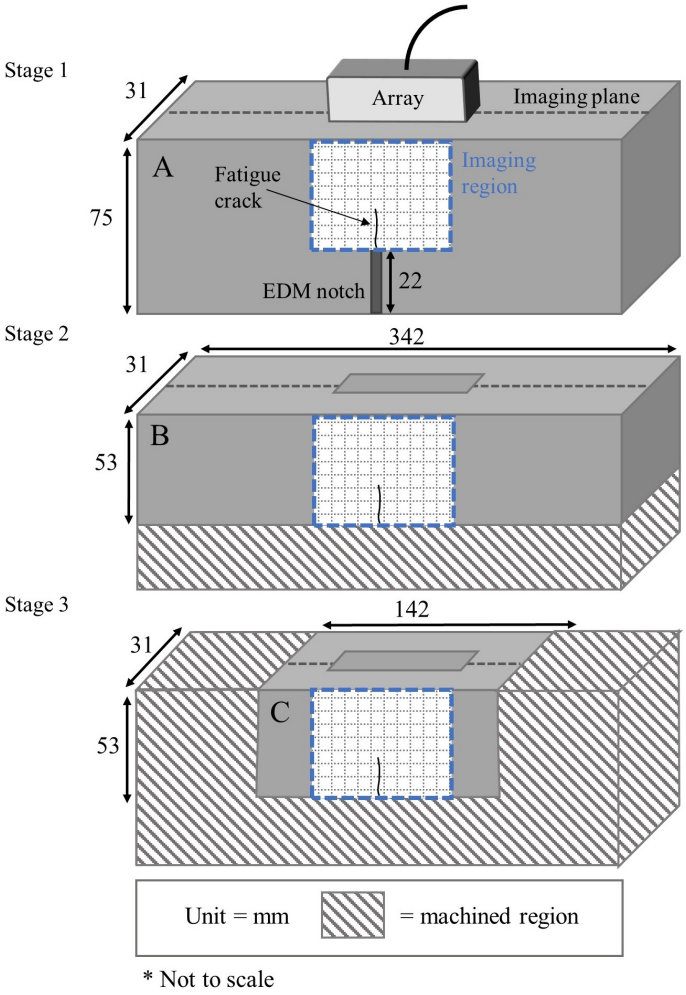

FIGURE 6.2: Geometric sizes for multiple volumes: (A) High, (B) Medium and (C) Low.

Sample ref.	Volume mm^3
High	7.8 x 10^5
Medium	5.6 x 10^5
Low	6.9 x 10^4

TABLE 6.1: Aluminium volumes for each stage of the multiple volume study.

6.4.2 Testing of metric with SNR

The nonlinear phased array experiment was conducted at multiple gate times to assess the SNR for various capture start gate-times. A parameter scan of gate-times was undertaken between 0.01 ms and 0.8 ms at intervals of 0.05 ms. The measure of SNR in these nonlinear images is a valid metric to test the diffuse metric, as the performance of this technique is reliant on a diffuse state and therefore the SNR can be used as a indication of a diffuse field. For consistency across images, we define the signal as the maximum nonlinear metric value in the white box in Fig. 6.3. Any value outside of the white box is considered as noise. The nonlinear values inside the white box are excluded as a measure of noise to ensure that the point spread function of the nonlinear feature is not considered in the measurement of noise. This is particularly important when considering the effect of cycle lengths as this leads to various point spread functions around the nonlinear feature which should not be considered in the SNR measurement. The size of the box is altered accordingly for each image to ensure an accurate measure of the SNR. The γ_{snr} is calculated by the following equation,

$$\gamma_{snr} = \frac{\gamma_{max}}{\gamma_{noise}} \tag{6.4}$$

where γ_{max} is the maximum nonlinear value within the white box and γ_{noise} is the rms of the nonlinear region outside of the white box (considered to be the undamaged region of the material).

Fig. 6.3 shows example nonlinear images to illustrate the typical SNR evolution with start gate-time. In Fig. 6.3(a), the controller start gate-time is set to 0.05 ms and it is clear from this nonlinear image that the nonlinear feature cannot be resolved from the background noise. Early in time, the controller is still capturing the coherent field and therefore the energy is not uniformly distributed. As such, the nonlinearity at the focal point has not yet spread uniformly

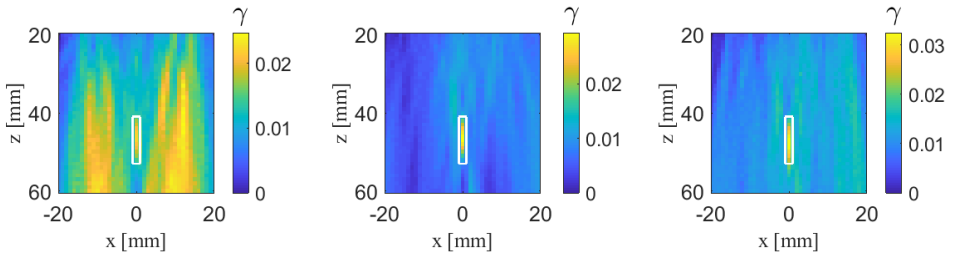

FIGURE 6.3: Nonlinear imaging results displaying the nonlinear metric γ, and the region used as signal (white) for various gate times: (a) 0.05 ms, (b) 0.2 ms and (c) 0.5 ms

throughout the material. Therefore, the energy losses between focal points in the nonlinear image are not relative and the metric is measuring local changes in space. This is caused by the varying propagation distances to the focal point which is captured in the coherent field. As a result, the nonlinear image is then distorted and resolution of the crack tip is limited. In Fig. 6.3(c) the start gate-time is set to 0.5 ms, and the feature is resolved, but the influence of noise begins to dominate. In both cases, the diffuse field has either not fully formed or the signal has become influenced by random noise, illustrating what happens if the incorrect start gate-time is selected. When using a start gate-time of 0.2 ms the nonlinear feature is resolved, see Fig. 6.3(b). The challenge now is to determine when the field is optimally diffuse, so that it is possible to achieve an accurate image without having to produce nonlinear images for multiple gate-times to select the most accurate. More importantly, when the presence of a crack tip or other nonlinear feature is unknown, it is not possible to determine an approximate diffuse field time through SNR analysis, therefore a statistical metric is necessary to ensure the nonlinear images are reliable.

Nonlinear experiments were conducted at multiple gate times to measure the effect of this parameter on γ_{snr} and determine a comparative measure of a diffuse field to test this diffuse metric. The results for the high volume sample are displayed in Fig. 6.4, presenting both the γ_{snr} and the α_{ph} metric implemented with a temporal window length, $\tau = 50\ \mu s$. This window length was long enough to ensure an accurate approximation of the diffuse field, but not so

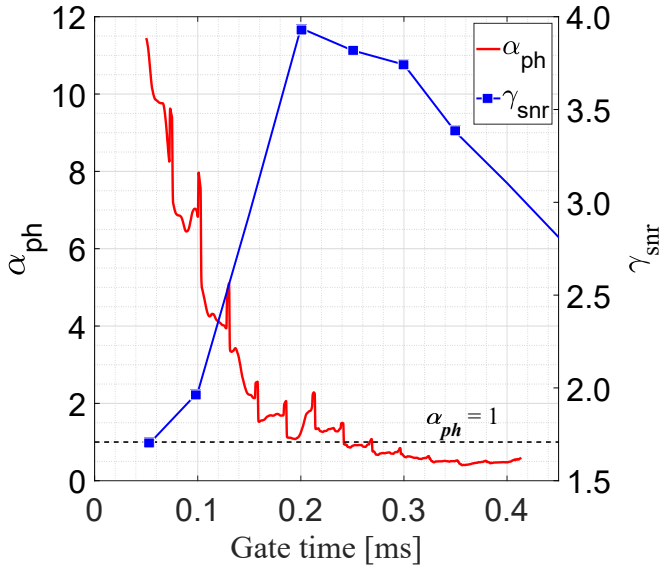

FIGURE 6.4: γ_{snr} results using various gate times and α_{ph} results for the high volume sample.

long that random noise could pollute the metric. The γ_{snr} results clearly indicate that 0.2 ms is the most appropriate gate time to establish a diffuse field for this specimen. This is determined as the gate time of the maximum γ_{snr} result, which suggests that the diffuse field dependent technique operates most successfully at this gate time. The convergence of α_{ph} occurs at 0.25 ms, suggesting that the metric has successfully predicted the time at which the field is most diffuse. The metric is considered to have converged as soon as the metric is equal to or less than 1.

6.4.3 Window size and cycle length

The effect of temporal window size, τ, on the convergence metric α_{ph} has also been investigated. It is assumed that the larger the window length, the better the approximation of a diffuse field, however as the window length increases, random noise becomes dominant and contaminates the metric. To establish the most accurate window length FMC data for the high volume sample was processed using the following window lengths: 10 μs, 50 μs and 200 μs. The results for

the varying temporal window sizes are presented in Fig. 6.5. It is clear that implementing a 200 μs window distorts the convergence of this metric and that the approximation is too coarse, causing the convergence to occur later in time, which incorrectly predicts a diffuse field. When using a 10 μs temporal window the coherent reflections from the back-wall and large boundaries produce dominant spikes in the correlation metric, which is expected in a coherent field. It is necessary to use a temporal window large enough to smooth-out the correlation peaks and troughs in order to accurately determine at which point the field is diffuse.

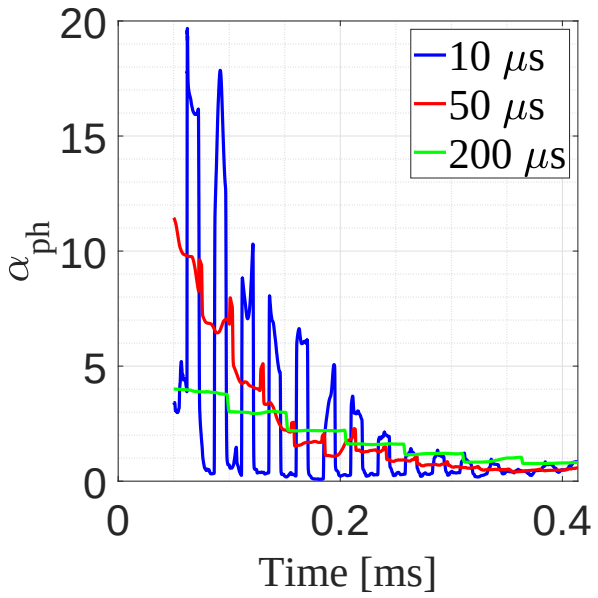

FIGURE 6.5: Phase coherence metric for multiple temporal windows: 10 μs (blue), 50 μs (red) and 200 μs (green).

To evaluate the influence of cycle lengths on the metric, a frame of FMC data was captured for the following cycle lengths: 2, 4 and 8. This FMC data was then post-processed to calculate the metric for various cycle lengths, which is displayed in Fig. 6.6. It is clear that the cycle length of the input signal does not influence the convergence rate of this metric, meaning that the time taken to reach a diffuse field is uncorrelated to cycle length, suggesting that cycle length is an independent variable to the diffuse field time. This is a positive feature as it allows

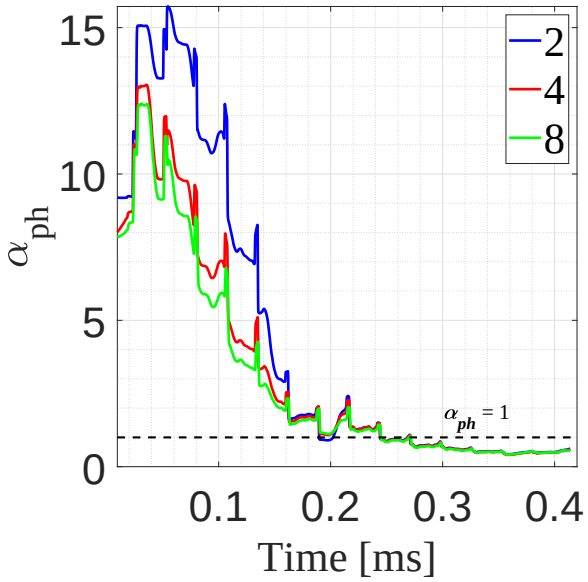

FIGURE 6.6: Phase coherence metric for multiple cycle lengths: 2 (blue), 4 (red) and 8 (green).

for varying cycle lengths to be implemented during phased array imaging without effecting the measurement of the diffuse field.

6.4.4 Volume alteration

The NUI technique is often applied to various sample sizes which require different start-gate times, as the time taken to reach a diffuse field is significantly dependent upon volume. A diffuse field is expected to converge sooner in relatively small geometries compared to large ones. It is important that this metric is a function of the volume, therefore it will now be confirmed that this behaviour should be observed in such experiments.

The effect of volume change was evaluated to test this metric for multiple volumes by machining down the same sample to various volumes (see Fig. 6.2 and table 6.1), ensuring that the nonlinear feature is the same across all three volume stages. For each of these stages FMC data was captured and the phase coherence metric was calculated using a window length

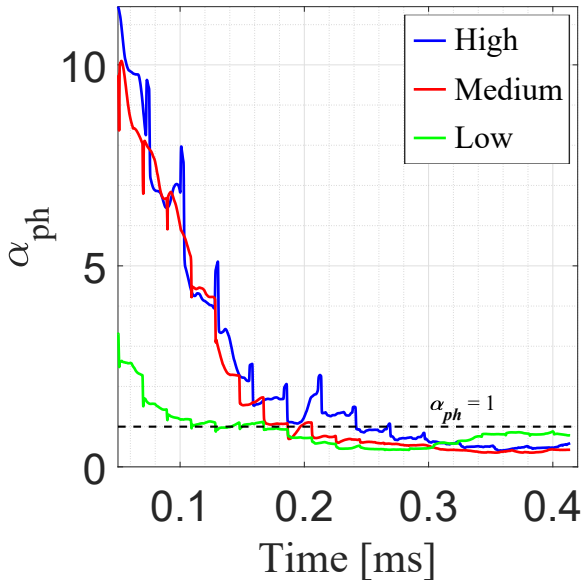

FIGURE 6.7: Phase coherence metric for multiple volumes: high (blue), medium (red) and low (green).

of 50 μs. This window length was chosen as it was determined as the most robust window length for the high volume sample. The results for all three samples are displayed in Fig. 6.7. The metric converges at 0.19 ms and 0.11 ms for the medium and low volumes respectively. The convergence is taken when the metric is less than one, as this value indicates there is no phase correlation between received signals. The convergences of the metric for medium and low sample volumes have also been successfully tested against γ_{snr} results in Fig. 6.8. In Fig. 6.8(a) the convergence of the metric at 0.19 ms agrees with the maximum γ_{snr} value of 0.15 ms for the medium volume sample. In Fig. 6.8(b) the convergence of the metric occurs at 0.11 ms correlates with the maximum γ_{snr} value of 0.1 ms for the low volume sample. These results confirm that this metric is dependent upon volume change, an expected outcome as larger geometries take longer to become diffuse due to reflections occurring later in time (i.e. increased mean propagation time).

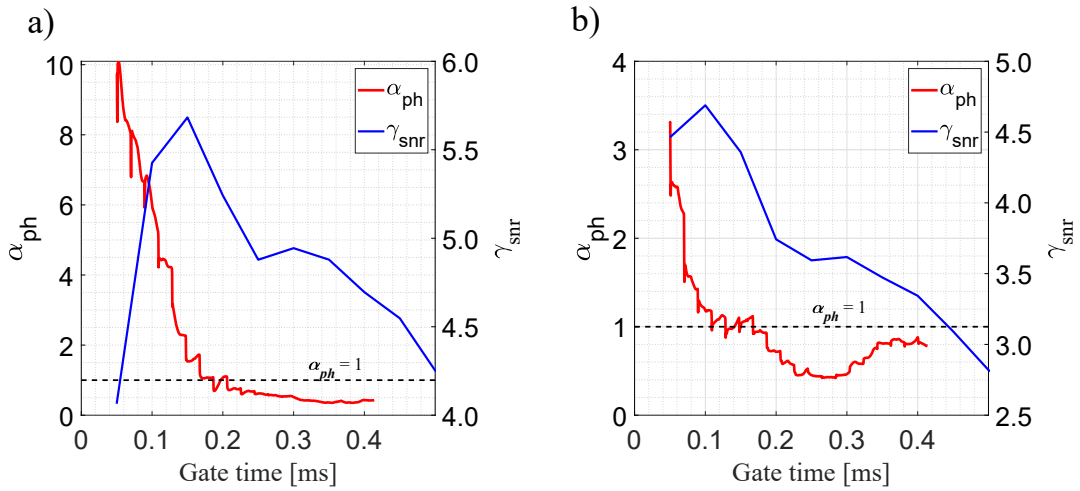

FIGURE 6.8: γ_{snr} results using various gate times and α_{ph} results: (a) medium and (b) low.

6.4.5 Multi-frequency

The influence of transmission frequency on the rate at which a diffuse field is achieved was also evaluated. Achieving a diffuse field using higher transmission frequencies will be challenging due to higher rates of attenuation degrading the signal and allowing random noise to dominate the energy captured. The arrays used for the multi-frequency study are presented in Table 4.1, and are used to evaluate the influence of transmission frequency on the convergence of the phase coherence metric on the low volume fatigue sample (see Fig. 6.2).

The 1 MHz transmission results are presented in Fig. 6.9(a) and it is clear that the convergence of the phase coherence metrics occurs at 0.19 ms using the 50 μs window. The time to converge is longer than in the 5 MHz transmission (see Fig. 6.8) by approximately a factor of 2. The 2.5 MHz transmission converges at approximately 0.1 ms which is consistent with the 5 MHz transmission convergence. For the 10 MHz transmission, there is a convergence at approximately 0.09 ms before the phase coherence begins to ascend. This assent indicates there is a limitation to the application of a 10 MHz array for the NUI method since the convergence of a diffuse field immediately results in noise contaminating the metric. This

is thought to be caused by significant coherent noise between the transducer elements being captured once the ultrasonic signals have been degraded due to higher attenuation rates. This is an important result as it suggests a clear limitation to achieving a diffuse field at higher frequencies.

6.4.6 Large scale geometries

Reaching a diffuse state in larger geometries can be difficult due to rates of attenuation that reduce the level of the received signal and in turn, result in random noise dominating. For large scale application, the metric was tested on a 1.0 x 10^7 mm^3 volume cuboid steel sample which is 1 order of magnitude larger than those previously studied. The FMC data set for this study was captured using the same experimental parameters as used for the previous samples. For this experiment, only FMC data was captured and no nonlinear experiments were conducted, as there is no known nonlinear feature in the material. Using the top and front configuration highlighted in 6.2 the phase coherence metric was tested. Fig. 6.10 (a) displays the results for the top configuration and shows a minima around 0.25 ms, which is most prominent in implementing a temporal window of 50 μs. This indicates a diffuse field before the linear ascent in the metric after 0.25 ms. Once again, this ascent indicates that later in time the received signals are becoming increasingly coherent, which is most likely to be caused by coherent noise between the transducer elements. Since the signals have attenuated significantly at this point in time the noise is now dominant and significantly effects the metric over the random noise. The source of this coherent noise is likely to be from the measuring instruments or grain scattering in the material.

The results for the front configuration in Fig. 6.10(b) display no convergence, only the influence of instrument noise. The performance of this metric to different configurations on the same sample is due to a closer back wall reflection from the top position to the front position,

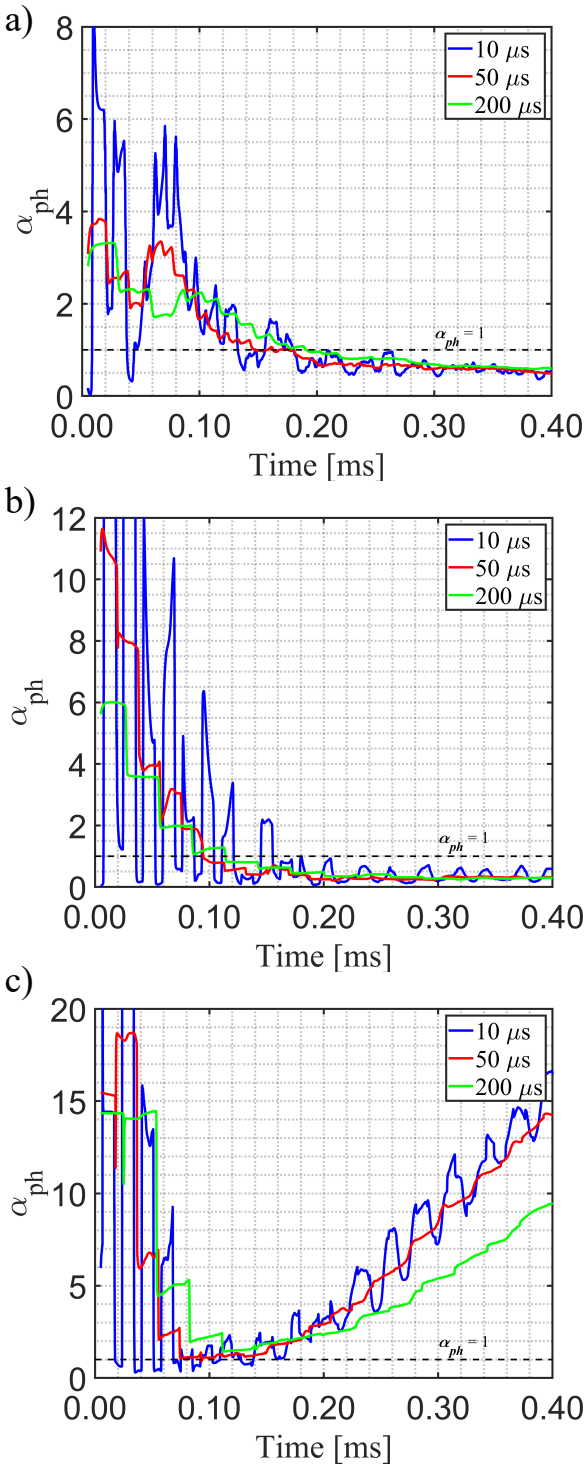

FIGURE 6.9: Phase coherence metric, α_{ph}, for various transmitting frequencies: (a) 1 MHZ, (b) 2.5 MHz and (c) 10 MHz.

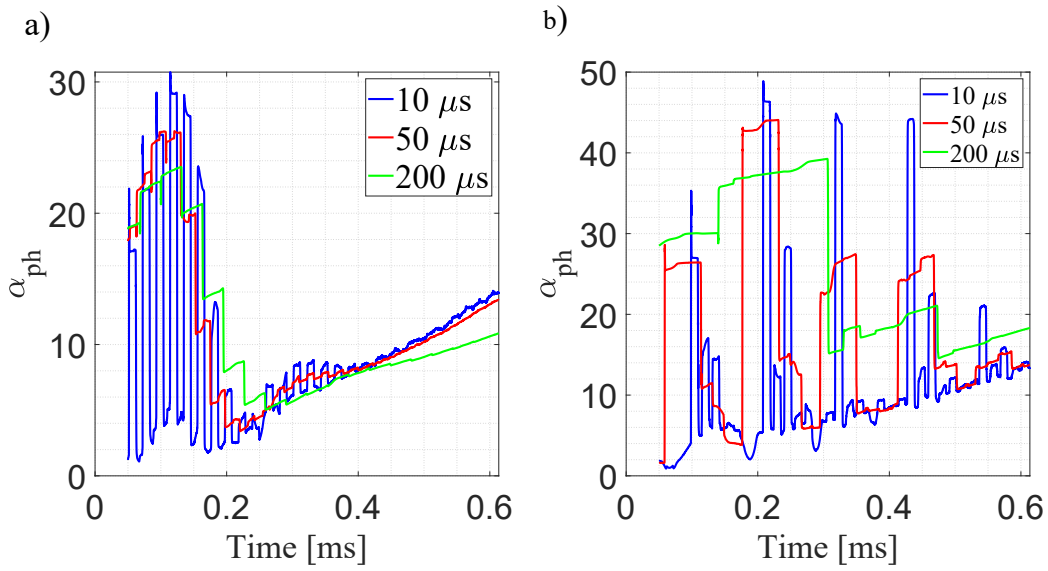

FIGURE 6.10: Phase coherence results for steel samples: (a) top configuration and (b) front configuration.

meaning that more energy is able to propagate back towards the array before attenuation is significant and random noise dominates. The difference in performance suggests there is a limitation to achieving a diffuse field in larger geometries. For larger samples the wave energy will have attenuated significantly before the incident field is able to scatter off multiple boundaries and homogenise.

6.5 Record length optimisation

Once a diffuse field has formed there is an optimum record length, t_r, which is desired in order to allow for capturing whilst the field is diffuse but before random noise begins to dominate. A longer capture will allow the signal to have properties closer to being truly diffuse, meaning a longer signal is desirable but before random noise is included in the capture. An investigation into instrument noise has been used to indicate the point at which noise is prevalent and dominant in the field, and is used as an indication of record length. The instrument noise is

measured as the energy across the array with no material coupled during an FMC. In this air coupled configuration, the propagating signal will not return to the array and predominately instrument noise will be captured. The instrument noise energy is then compared to the energy captured from when the array is coupled to the samples described in Fig. 6.2, and is referred to as the material energy E_{mat}. The percentage of instrument noise energy, E_{ins}, from the material energy, E_{mat}, indicates at which point in time instrument noise will be significant. In the coherent and diffuse field it will be expected that E_{mat} is significantly higher as the wave energy is still high. Later in time it is expected that E_{ins} will become increasingly significant as the wave energy will have attenuated.

To establish an appropriate threshold for the percentage of noise energy, the effect of record length on γ_{snr} was investigated. For this analysis the time series data for the nonlinear experiments was truncated to vary the record length of the captured data. The record length is equal to the time interval between the start gate-time and the end gate-time ($t_r = t_e - t_s$), therefore by analysing the most appropriate end gate-time it is possible to determine the most efficient record length. For this study the start gate-times implemented was 0.2 ms for the high volume and the rest of the parameters were consistent with the study in Section 6.4.2.

The percentage of instrument noise energy from the material energy, E_{ins}/E_{mat}, and the γ_{snr} results for various record lengths is presented in Fig. 6.11. These results confirms that the γ_{snr} is highest when t_r is set to 0.15 ms for the high volume sample. This most effective record length correlates with a percentage instrument noise of 14 %. Therefore a threshold of 14% for the percentage of noise energy can be derived to determine the record length, ensuring that enough of the diffuse field is captured, but before random noise begins to dominate. This process can now be added to the nonlinear imaging methodology.

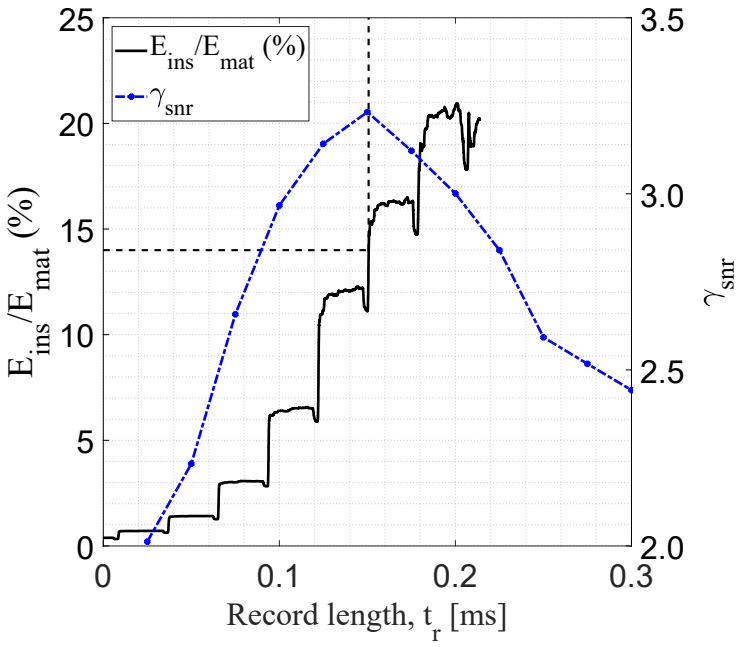

FIGURE 6.11: Percentage of instrument noise energy of material noise energy for high volume sample.

6.6 Conclusion

This study concludes that the phase coherence metric is suitable for determining a diffuse field due to its strong correlation with the highest γ_{snr} for various gate times. The choice of temporal window has proven to be an important factor for determining correct convergence with a diffuse field, therefore it is important that the window size is selected carefully. Most importantly this metric has proved effective and robust for multiple volumes and geometries, cycle lengths and various transmission frequencies. The investigation into transmission frequency shows that it is not possible to achieve a diffuse field at 10 MHz, indicating a clear limitation to the NUI method at higher frequencies. Results for a large-scale geometry suggest that it is challenging to detect a diffuse field using the metric. The top configuration shows some convergence before random noise dominates, which can be used as an insight into the most appropriate start gate-time, despite it not fully converging. Further study into the limitation of the phase coherence metric based on larger volumes would be valuable to establish a critical limit for

this metric. It is also concluded that an appropriate recording length can be established by calculating the percentage of instrument noise energy against energy captured in the material, therefore providing a procedure to reduce random noise in the nonlinear measurement.

This chapter concludes the following procedure should be conducted on a new sample where the presence of a crack tip is unknown:

1. Switch on the controller and allow 10 minutes for the controller to warm up.
2. Collect FMC data when the array is un-coupled to calculate the instrument noise.
3. Couple the array to the specimen to collect FMC data and calculate the phase coherence metric to determine the start gate-time.
4. Process the coupled and un-coupled FMC data to calculate E_{ins}/E_{mat} and determine the record length for the nonlinear experiment.
5. Conduct the nonlinear experiment using the start gate-time and record length parameters.

The optimisation of NUI has improved this technique's reliability significantly and now offers the potential for industrial deployment.

Chapter 7

Classical nonlinearity imaging

7.1 Introduction

The previous chapters of this thesis have been concerned with the optimisation of the nonlinear ultrasonic diffuse energy imaging (NUI) method for detection of fatigue crack tips (i.e. non-classical forms of nonlinearity). The enhanced NUI method proposed in Section 4, has shown to increase the detectability of a fatigue crack tip significantly by evaluating nonlinear energy at multiple frequencies. The implementation and validation of the phase coherence metric in Section 6 allows for accurate determination of a diffuse field to ensure energy is only captured when the wave-field has homogenised, significantly increasing the detectability (i.e. SNR) of fatigue crack tips. In addition, the optimised multi-view method allows for control over the point of the sensitivity profile used in detecting nonlinear features through focusing for multiple reverberations. In this chapter, these optimisations will be implemented in an attempt to resolve classical nonlinearity changes, induced by lattice anharmonicity and dislocations. Since classical forms of nonlinearity do not produce linear scattering, the NUI method is required since its operation does not rely on coherent scattering from nonlinear features. The optimisation of the NUI method to fatigue crack tips is expected to allow for the detection of

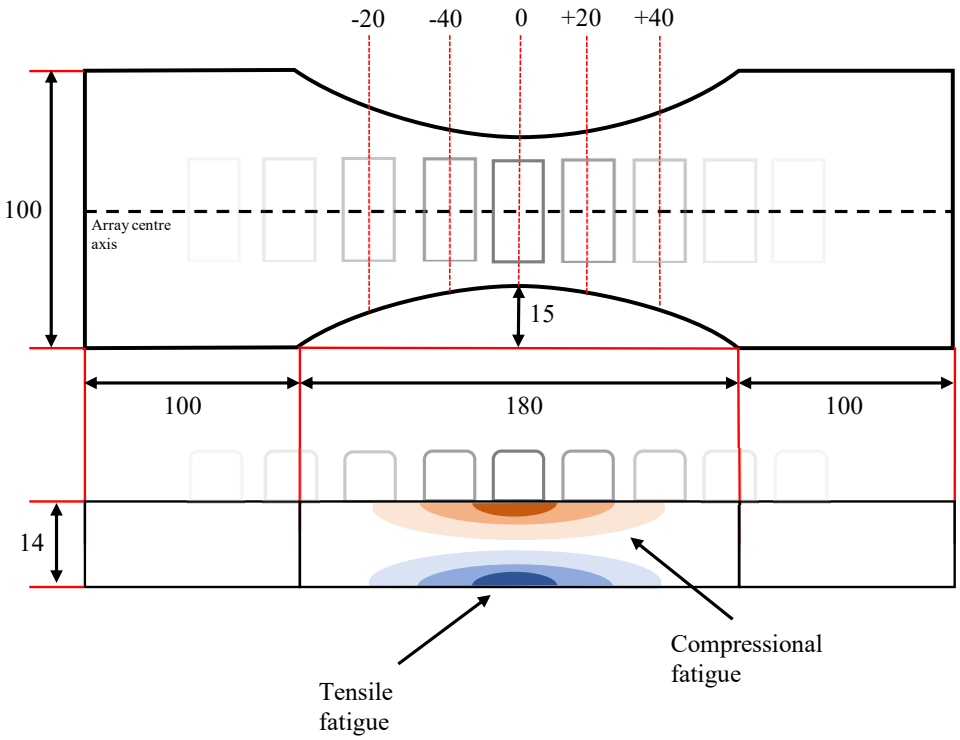

FIGURE 7.1: Dimensions (mm) of the fatigue samples used for the strain field imaging study. The red dashed lines indicated the scanning position and the grey box represent the array position along the centre axis.

the relatively lower level nonlinearity induced by classical sources.

7.2 Test specimens

For this study Al2024-T351 fatigue samples loaded using a 4-point bending jig were used. The dimensions of the sample are presented in Fig. 7.1 and are a "dog bone" shape to increase the localised strain in the centre (narrowest point in the sample) of the sample when it is deformed. This increase in localised strain increases in the centre of the sample and forms fatigue focused on the surfaces. Using a -0.3% to 0.5% strain the fatigued sample was loaded to 80% of fatigue life, where fatigue life is defined as the number of cycles required to reach failure. The loading configuration is designed to produce asymmetric strain in-order to establish focused strain on both sides of the sample.

7.3 Experimental procedure and parameters

The experimental procedure for this study is facilitated using a Verasonics array controller using a collection of phased arrays with different centre frequencies. The successful T5-R1 and T5-R10 dual array methods proposed in Section 4 will be implemented. This is to allow analysis of the low (bandwidth mixing), fundamental and second harmonic energy which has been proven to increase the detectability of nonlinear features. For this configuration channels 1-64 were used for transmitting and receiving, whilst the channels 65-128 were used for receiving only. In addition, a 128 element 10 MHz single frequency configuration (T10-R10)(identical transmit and receive frequencies) is evaluated, since the relatively higher transmission frequency and increased number of elements is expected to increase the nonlinear response of the fatigue. The increased number of transmission elements and frequency transmission is expected to increase the nonlinearity induced in the material. Arbitrary waveform generation was implemented and a cycle length of 10 was selected for the transmission signal. The cycle length allowed for maximum transmission of energy and maintained a narrow bandwidth, to ensure selectivity between frequency components. The cycle length selected is also limited to provide sufficient spatial resolution. The cycle length is longer than those used for detecting crack tips in the previous chapters, this is to prioritise detection over spatial resolution to increase detectability to relatively lower level nonlinearity.

The reception time t_r is set using the phase coherence metric defined in Section 6, which approximates the time taken for the wave-field to homogenise, i.e. the time taken to reach a diffuse field. To calculate the phase coherence metric full matrix capture (FMC) data was captured for each transmission array used across the configurations. In this case, FMC data was captured using a 5 MHz and 10 MHz phased array. The phase coherence results for a 5 MHz and 10 MHz transmission are presented in Fig. 7.2, and confirm that the metric converges below 1 at 0.05 for both transmission frequencies. Generally, high frequencies converge to a

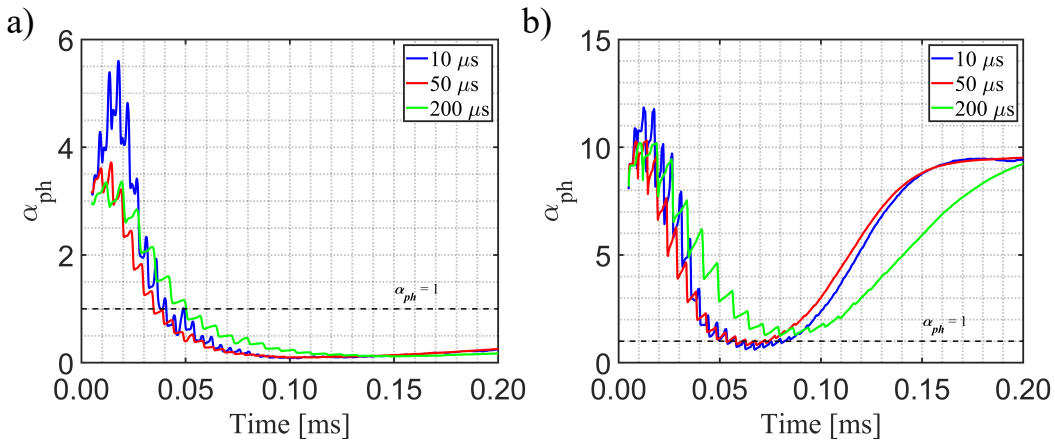

FIGURE 7.2: Phase coherence metric using FMC data collected on the dogbone specimens transmitting at: a) 5 MHz and b) 10 MHz. The phase coherence results are plotted for multiple time window lengths: 10 μs, 50 μs and 200 μs. The dashed line indicates the phase coherence metric equals 1.

diffuse field earlier in time due to attenuation rates (as seen in Section 6.4.5). The consistent convergence of to a diffuse field here is attributed to 128 elements transmitting in the 10 MHz array and only 64 elements for the 5 MHz array. The higher element contribution will cause more energy to be transmitted into the material and therefore the convergence to a diffuse field occurs later in time. When transmitting at 10 MHz the phase coherence metric increases later in time after converging to 1, which is attributed to coherent noise between the transducer elements. The convergence times can now be implemented as the start gate-times for the relevant transmission frequencies to ensure the field is diffuse when capturing data has begun.

In an attempt to increase detectability of the nonlinearity the multi-view method proposed in Chapter 3 will be implemented to ensure the most effective point in the sensitivity profile is used to focus at the nonlinear features. This is achieved by focusing past the back wall in the material and allowing the flat surface on the back-wall (and front-wall) to reflect the beam formed wave-front and focus in the material. This method is expected to expand the sensitivity range of the NUI method as it allows for some dynamic control over the sensitivity profile of the array.

7.4 Results

7.4.1 γ full image

The T5-R5 results taken at the centre point in the sample (0 mm) for the dog bone samples are presented in Fig. 7.3, where the full nonlinear images are plotted displaying the multiple reflections through depth. At the centre point in the sample a high strain field is expected in the fatigued sample, therefore a high γ is expected compared to the non-fatigued sample. The non-fatigue sample provides an indication into the noise floor of the material since there is no fatigued induced nonlinearity in the material, and only background nonlinearity is captured. The spatial distribution and energy levels are consistent across the fatigued and non-fatigued samples suggesting that energy detected in the fatigued sample is noise and is not caused by nonlinearity. This is also seen in the T5-R1 configuration presented in Fig. 7.4 where the nonlinear energy in the image is consistent between the samples, suggesting that the nonlinearity in the material is not being detected above the noise floor.

The T5-R10 results presented in Fig. 7.5 for the fatigue sample also show consistent energy distribution in the image and no clear nonlinear features, once again implying that only noise is being captured. Unexpectedly, using the T5-R10 configuration highly nonlinear features have been detected in the non-fatigued samples at the front wall. These features are potentially caused by nonlinearity induced during the manufacturing process since no mechanical fatigue has been applied to this sample. These inclusions mean that the strain fields can not be validated by comparing the two samples, and therefore is not investigated further.

The T10-R10 configuration shows a similar nonlinear energy distribution between the samples, however the energy in the fatigued sample is significantly less than the noise floor determined from the non-fatigued sample, by a factor of 3. This is potentially caused by a

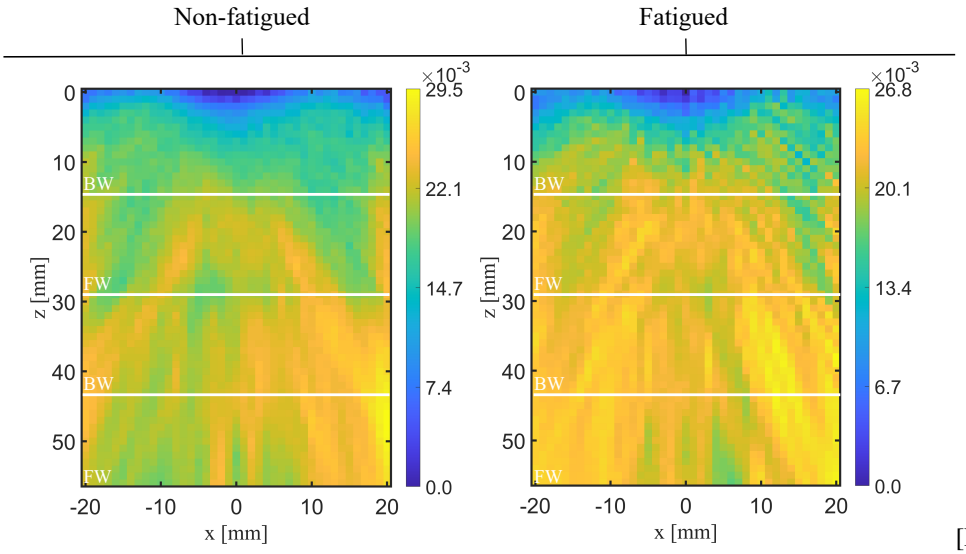

[H]

FIGURE 7.3: Nonlinear diffuse images for multiple reverberations using the T5-R5 configuration. The white lines indicate the back-wall (BW) and front-wall (FW).

change in the relative noise between the two fields between the samples, induced by random noise. It could also suggest that the strain field nonlinearity in the fatigued samples is non-monotonic and therefore the nonlinear parameter is reduced in the presence of the strain field. This has been observed in a previous study where the nonlinear parameter β reduces with loading cycles [82]. This is would explain the loss in nonlinear energy shown in the nonlinear metric γ in the fatigued sample, and therefore could indicate a positive result in detecting the nonlinearity.

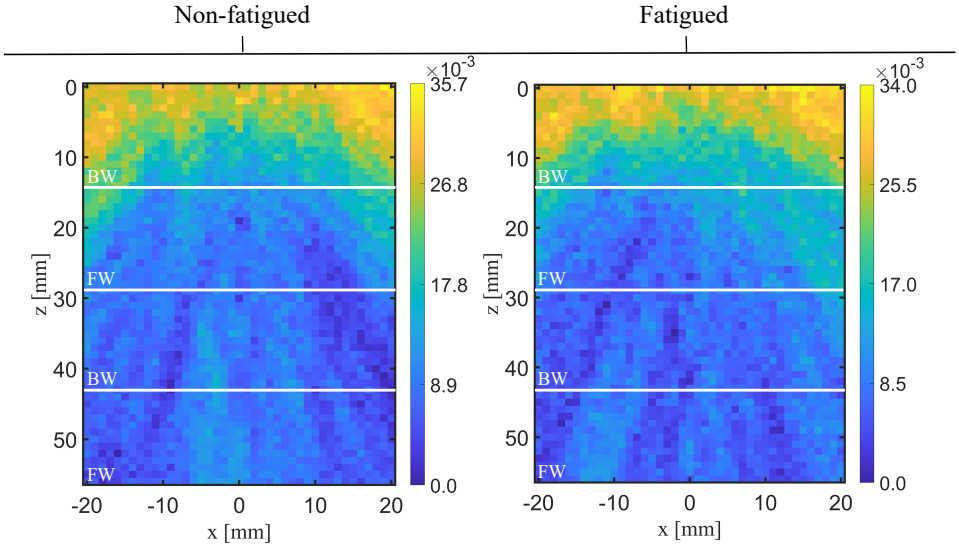

FIGURE 7.4: Nonlinear diffuse images for multiple reverberations using the T5-R1 configuration. The white lines indicate the back-wall (BW) and front-wall (FW).

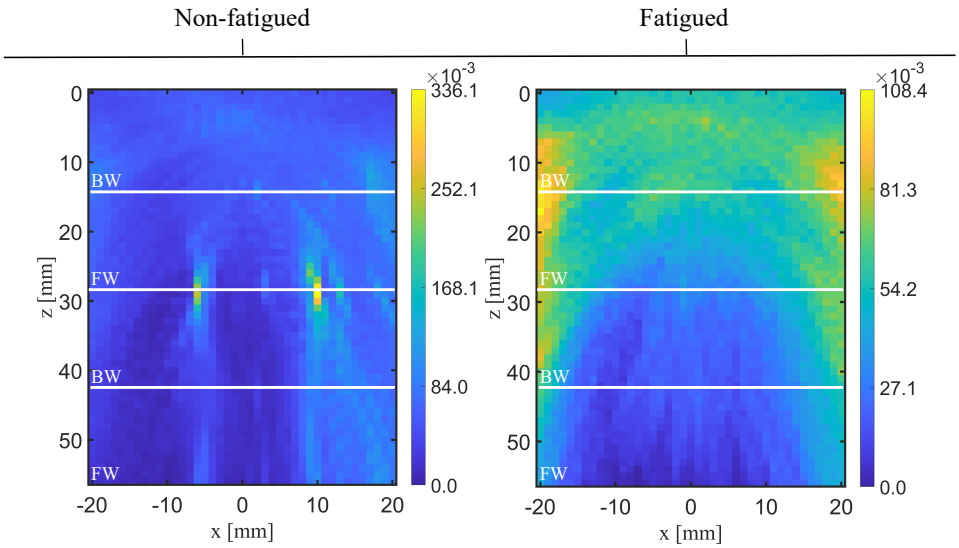

FIGURE 7.5: Nonlinear diffuse images for multiple reverberations using the T5-R10 configuration. The white lines indicate the back-wall (BW) and front-wall (FW).

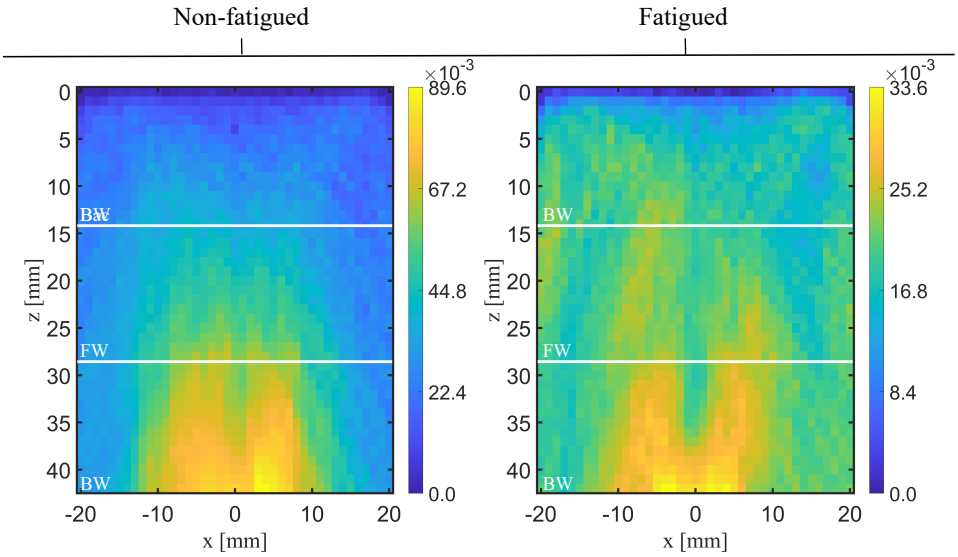

FIGURE 7.6: Nonlinear diffuse images for multiple reverberations using the T10-R10 configuration. The white lines indicate the back-wall (BW) and front-wall (FW).

7.4.2 γ image separation

To investigate the nonlinear results further, the nonlinear images in the previous section containing the nonlinear information for all the reflections (all multi-views) are separated into individual image views. The benefit of this is re-scaling of the image colour axis to allow for relatively small nonlinear energy to be visible in the image since the colour axis range will be adjusted to each view image, rather than a range representing all image views. In addition, the z-axis is has been adjusted and the appropriate reflections have been rotated so the reflected mirror images can be compared directly.

The T5-R5 results for both the fatigue and non-fatigue dog-bone samples are presented in Fig. 7.7 for a total of 4 multi-view images. It can be seen across all image views that the nonlinear energy between the fatigue and non-fatigue samples is relatively consistent both in maximum nonlinear amplitude and spatial distribution. This once again suggests that the strain field in the fatigued sample has not been detected, and only the noise floor is being imaged. This means the nonlinearity induced by the strain field is not causing significant energy loss from the fundamental bandwidth. This is also reflected in the T5-R1 images in Fig. 7.8, where the nonlinear energy captured between the samples is consistent. Despite reduced attenuation rates at the bandwidth mixing frequency causing an increase in nonlinear energy received, the nonlinearity induced by the strain field is still not detectable. The T10-R10 results are presented in Fig. 7.9 and concludes that image separation has increased the variation in the nonlinear parameter between the samples. The reduction in the nonlinear parameter γ by a factor of 2 indicates a detection of nonlinearity in all the image views (assuming non-monotonic nonlinearity).

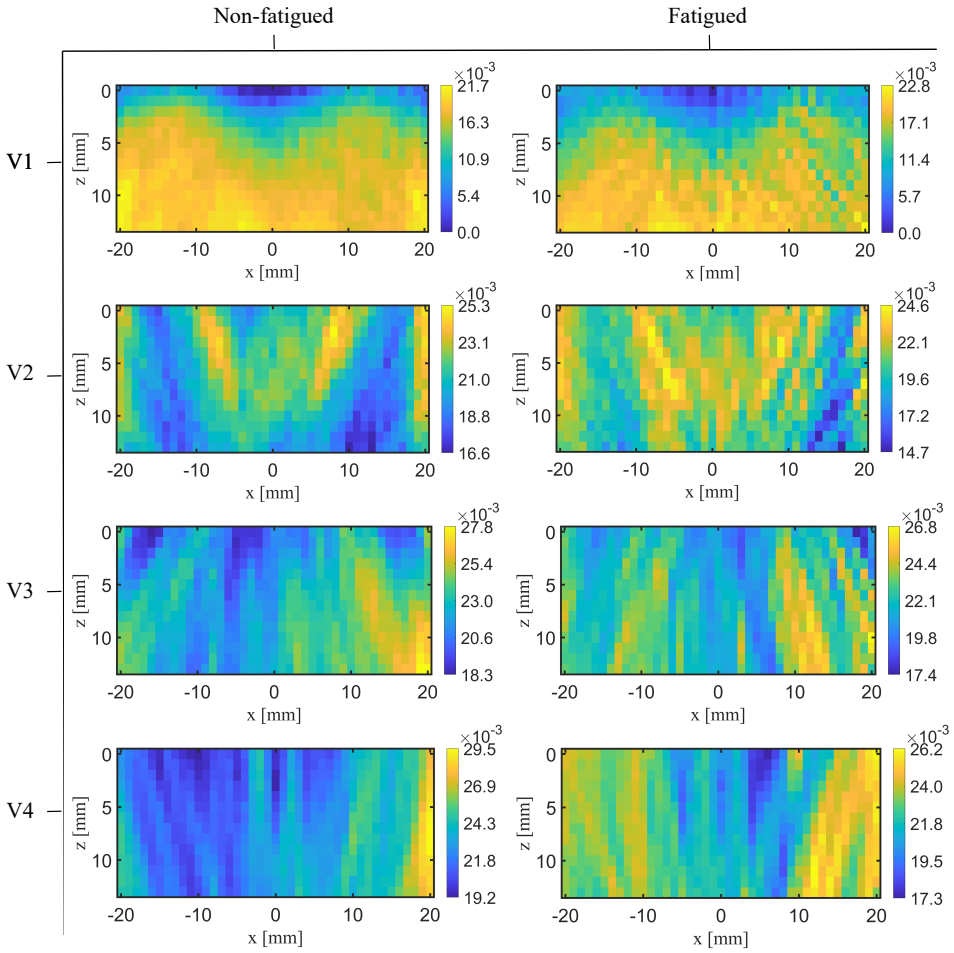

FIGURE 7.7: Nonlinear diffuse imaging results presenting the nonlinear metric γ for the T5-R5 configuration on Aluminium dog bone samples receiving at the fundamental frequency. The fatigued and non-fatigue results are plotted for both for all 4 image views.

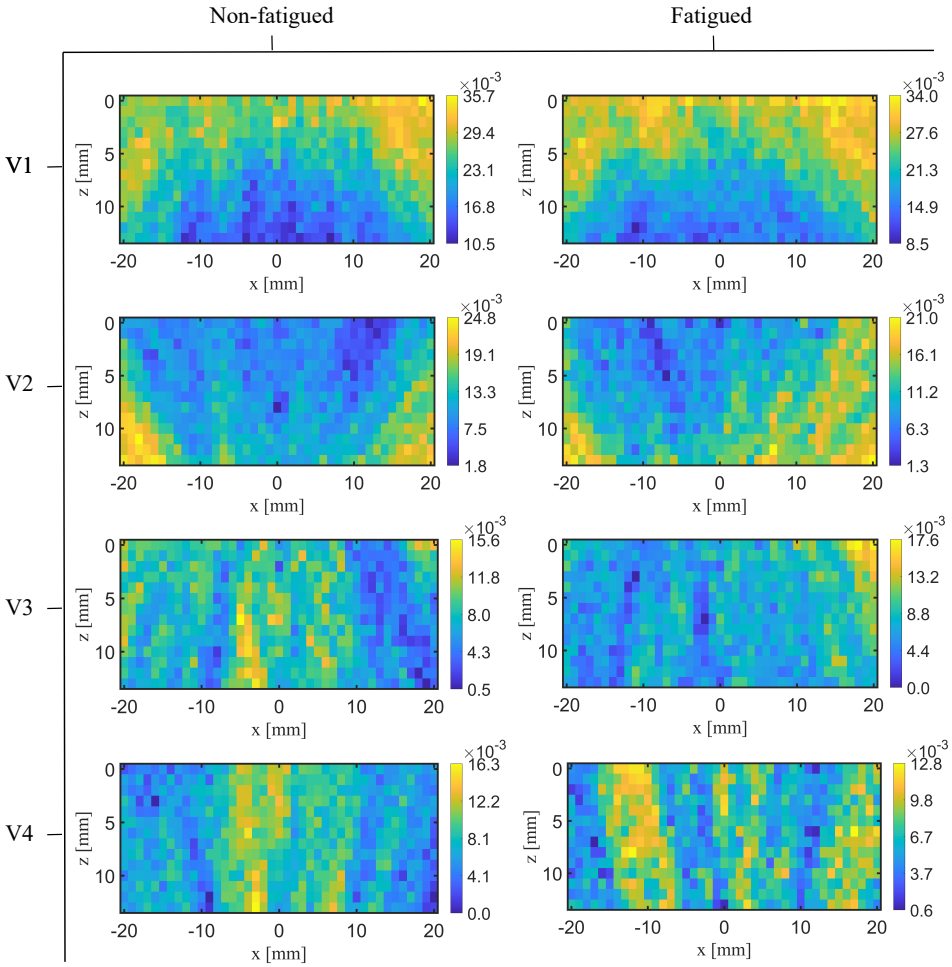

FIGURE 7.8: Nonlinear diffuse imaging results presenting the nonlinear metric γ for the T5-R1 configuration on Aluminium dog bone samples receiving at the bandwidth frequency. The fatigued and non-fatigue results are plotted for both for all 4 image views.

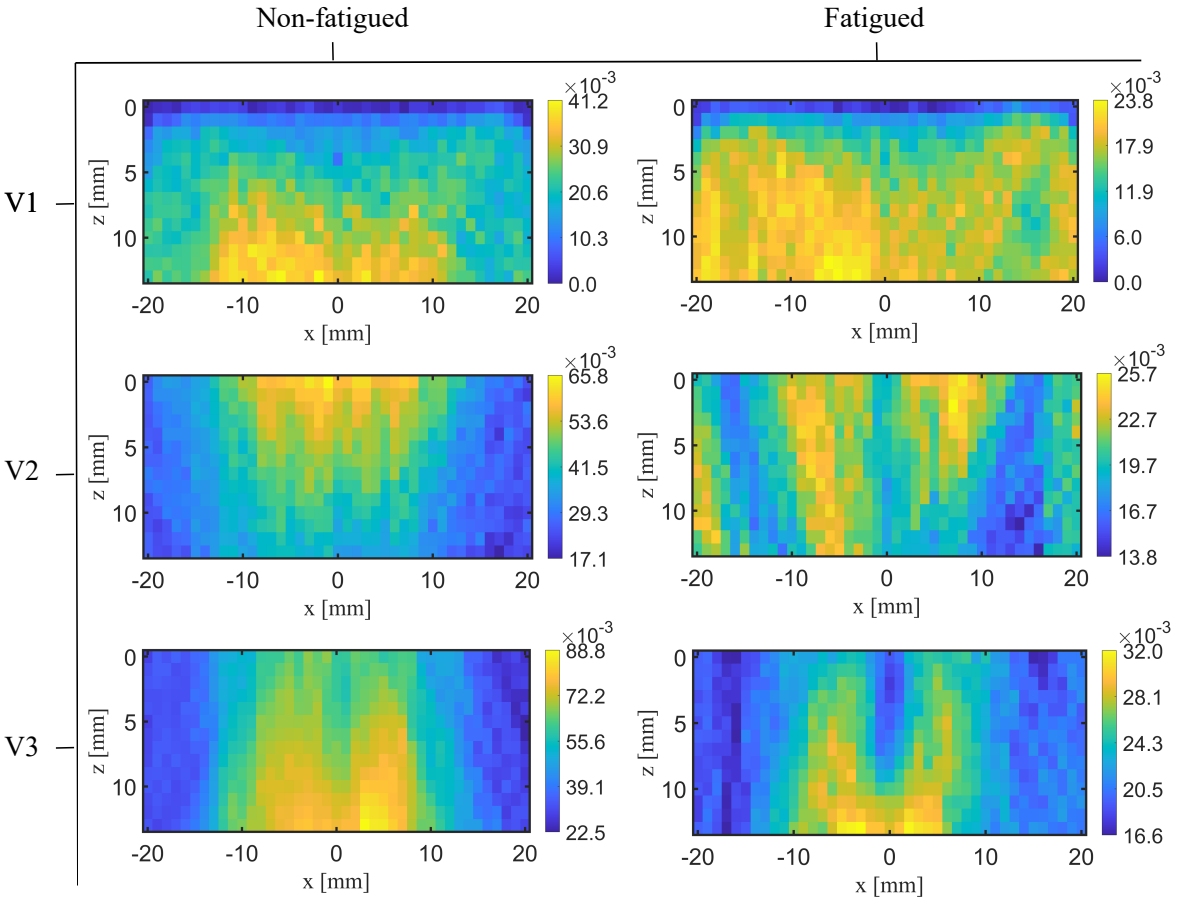

FIGURE 7.9: Nonlinear diffuse imaging results presenting the nonlinear metric γ for the T10-R10 configuration on Aluminium dog bone samples. The fatigued and non-fatigue results are plotted for both for all 4 image views.

7.4.3 γ averaging

In this section, nonlinear images are taken at 20 mm intervals along the sample (illustrated in Fig. 7.1) along the length of the material in the scanning direction. A strain gradient is expected through depth in the material and in the array scanning direction. Therefore, the mean of the nonlinear metric γ along the x-axis for each image view is computed in an attempt to reduce the presence of noise in the image (as illustrated in Fig. 7.10), since constant properties are expected in the x-direction. Despite reduction of localised nonlinearity from the image domain to a single point, there is still a degree of spatially resolved nonlinearity through the process of scanning the array across the sample. It is expected that as the array is translated across the sample the mean nonlinear metric γ will be highest in the centre of the sample (the centre scanning position), since the narrowest point in the sample will have the highest localised fatigue. As the array is translated in either direction away from the centre, the fatigue damage decreases and therefore a variation in $\bar{\gamma}$ is expected. Therefore a change in γ is expected at the surface (the top and bottom of the image) and a decrease in γ in the centre.

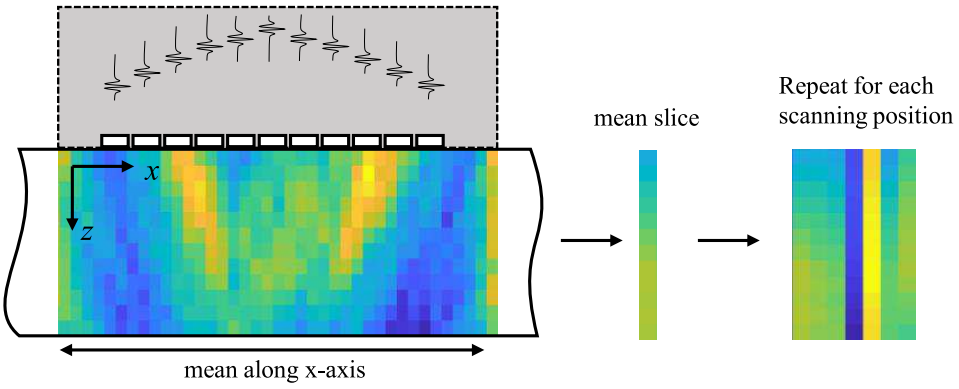

FIGURE 7.10: Illustration of γ averaging process used for reducing noise.

The scan results for T5-R5 presented in Fig. 7.11 show consistency in γ across the scanning lengths for both the fatigued and non-fatigued samples. The distribution of nonlinear energy γ throughout the scanning positions and the depth is consistent across samples confirming there is no increase in γ in the presence of fatigue. However, the reduction in the nonlinear

parameter across all V1-3 could be potentially caused by non-monotonic nonlinearity.

The T5-R1 results in Fig. 7.12 show no clear strain gradient along the scanning positions and through depth, as well as no significant change in γ between samples in image views V1-2. This suggests random noise is being captured instead of nonlinear information. In image views V3-4 there is varying distribution of nonlinear energy between samples, and a reduction in the nonlinear parameter in the fatigued samples, suggesting some non-monotonic nonlinear energy is being captured.

The T10-R10 results, presented in Fig. 7.13, show that γ is lower in the fatigued case for all image views. Interestingly, the distribution of nonlinear energy along the scanning length is not consistent with the base noise level in the non-fatigued sample. There is significantly more nonlinear energy present in one direction of the scanning length. It could be suggested that this is caused by the strain field, however the loading applied to the specimen is expected to produce a symmetrical strain gradient (line of symmetry at the centre point 0 mm) along the scanning positions, therefore it is likely that the cause of this change in nonlinear energy between samples is caused by experimental error. This is caused by inconsistent coupling between image captures, particularly effecting higher frequency.

It is clear the averaging process has not effectively resolved the strain gradient in the fatigued sample across the scanning positions and through depth by reducing noise. In addition, this averaging process has not improved differentiation between the fatigue and non-fatigue samples.

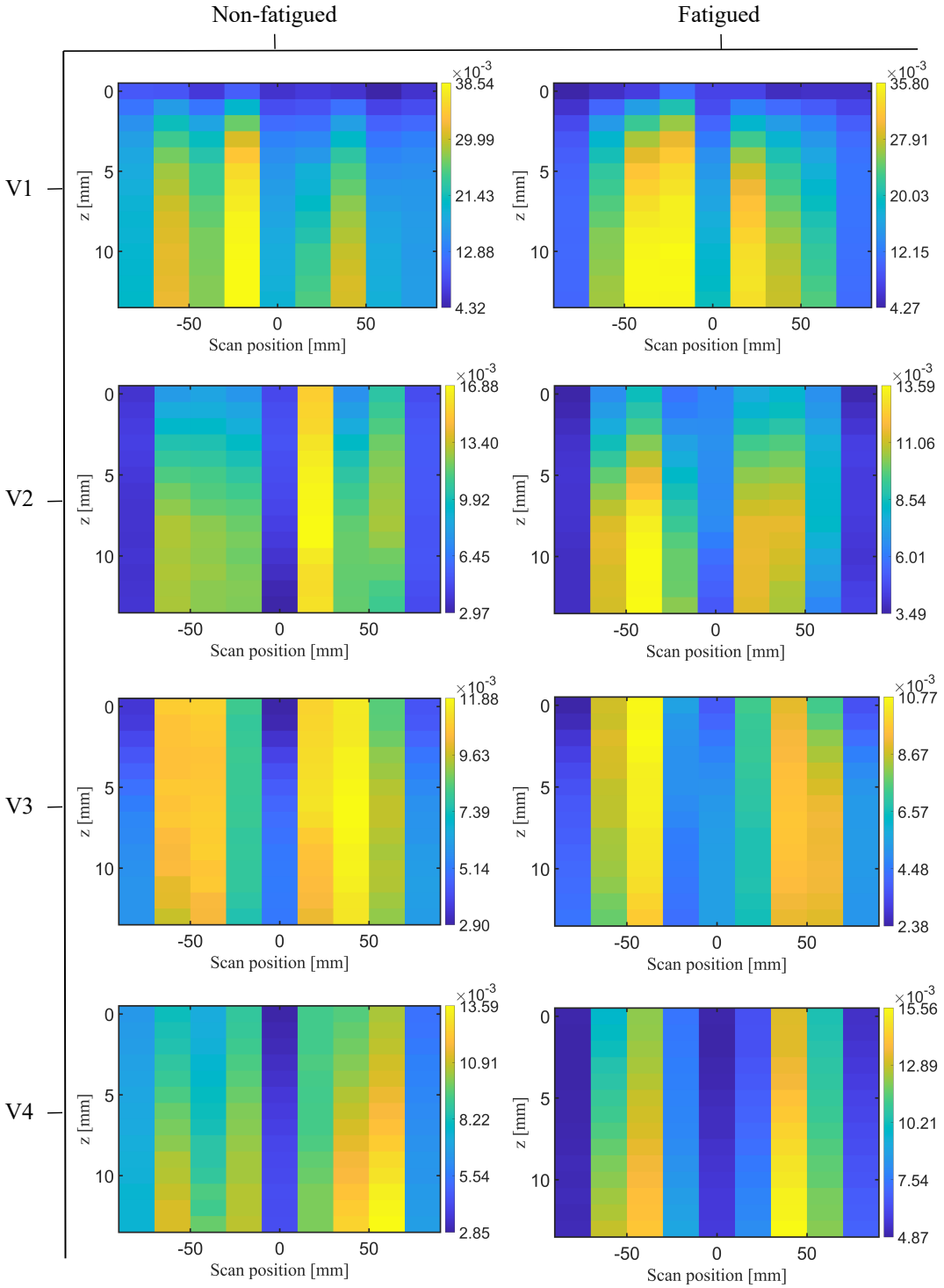

FIGURE 7.11: Average nonlinear diffuse imaging results presenting the nonlinear metric γ for the T5-R5 configuration on Aluminium dog bone samples for each scanning position. The fatigued and non-fatigue results are plotted for both for all 4 image views.

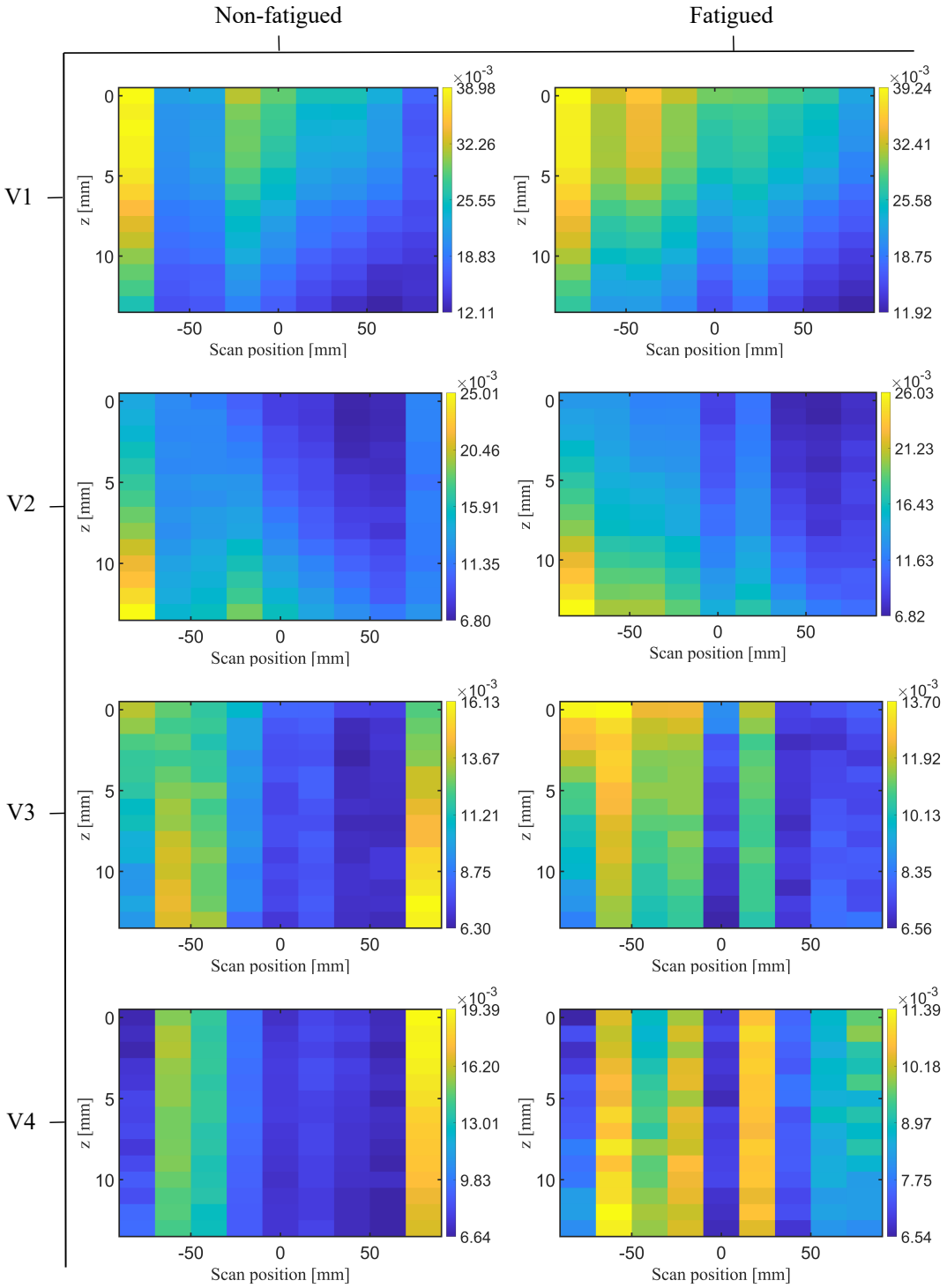

FIGURE 7.12: Average nonlinear diffuse imaging results presenting the nonlinear metric γ for the T5-R1 configuration on Aluminium dog bone samples for each scanning position. The fatigued and non-fatigue results are plotted for all 4 image views.

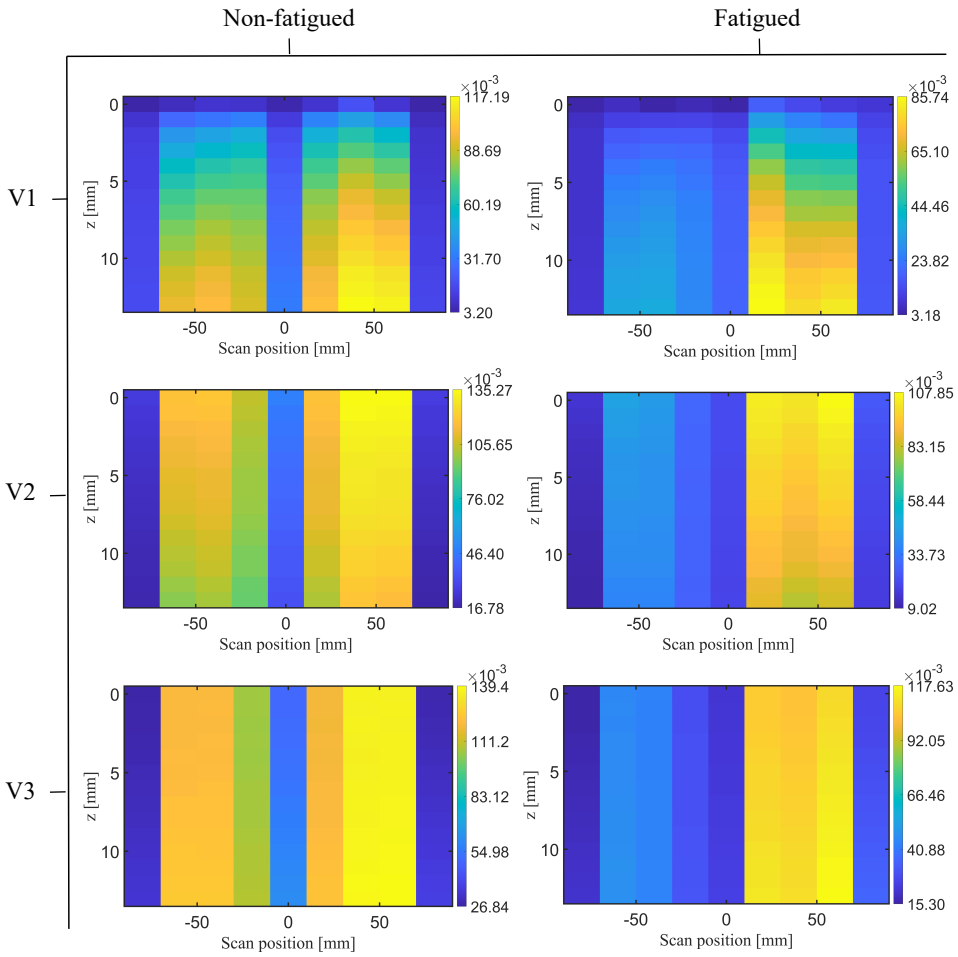

FIGURE 7.13: Average nonlinear diffuse imaging results presenting the nonlinear metric γ for the T10-R10 configuration on Aluminium dog bone samples for each scanning position. The fatigued and non-fatigue results are plotted for all 4 image views.

In an attempt to reduce noise further, the total mean of the nonlinear images for each scanning position is calculated. Despite loss of spatial resolution it would still be beneficial to evaluate material nonlinearity as a function of scanning position, providing some spatial resolution of fatigue. The mean of the nonlinear images, $\bar{\gamma}$ are presented in Fig. 7.14. These results show consistent $\bar{\gamma}$ across both samples for all configurations, suggesting once again that nonlinearity is not being detected in the fatigue sample. Using the T10-R10 configuration (presented in Fig. 7.15) the fatigue sample across all views shows a reduction in $\bar{\gamma}$ across all scanning positions. This disparity could once again indicate that nonlinearity is varying in a non-monotonic manner (i.e. the metric reduces in the presence of nonlinearity) and therefore the nonlinearity parameter is reducing in the presence of the strain field.

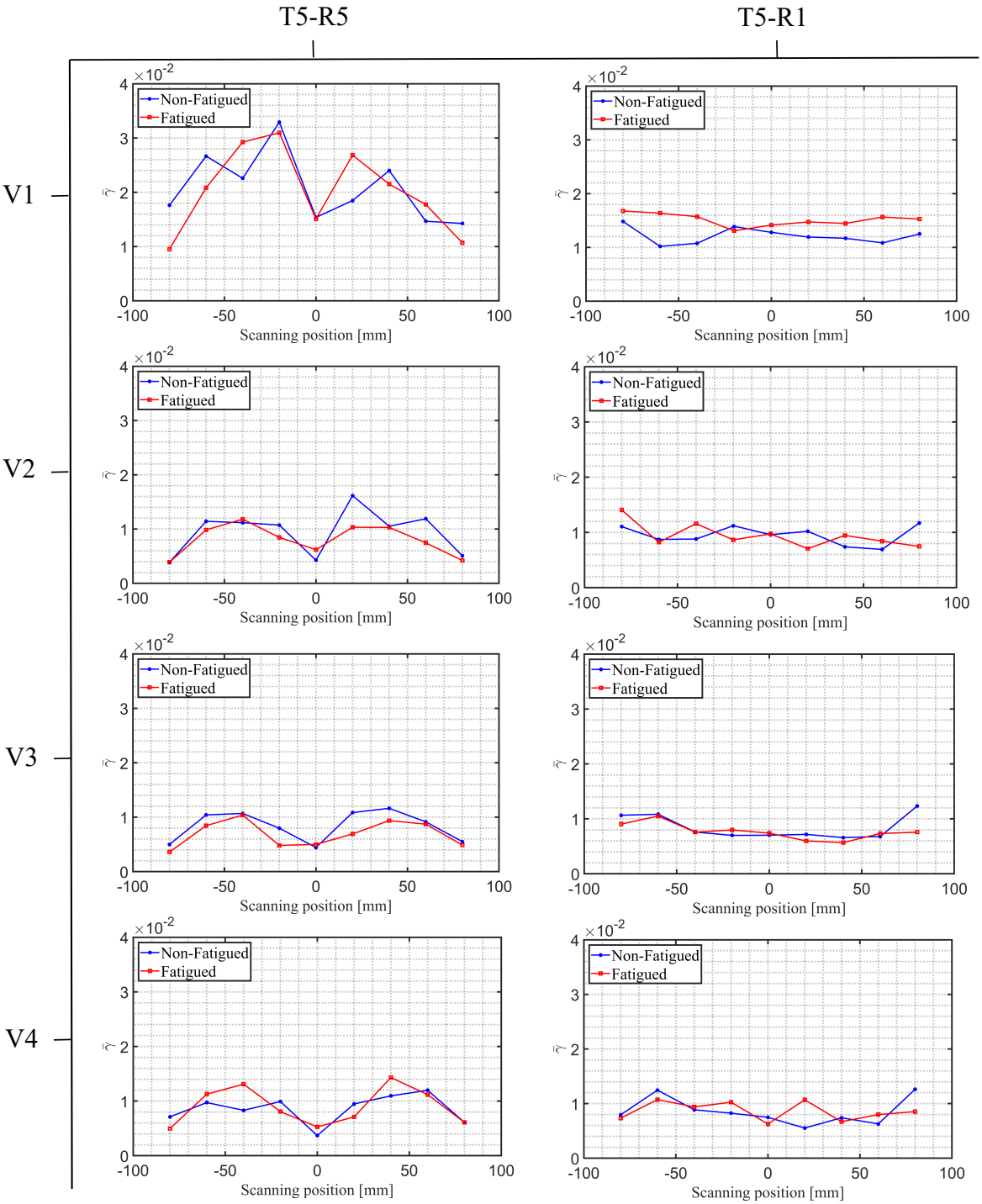

FIGURE 7.14: Average nonlinear diffuse imaging results presenting the nonlinear metric $\bar{\gamma}$ of the full image for the T5-R5:R1 configuration on Aluminium dog bone samples for each scanning position. The fatigued and non-fatigue results are plotted for all 4 image views.

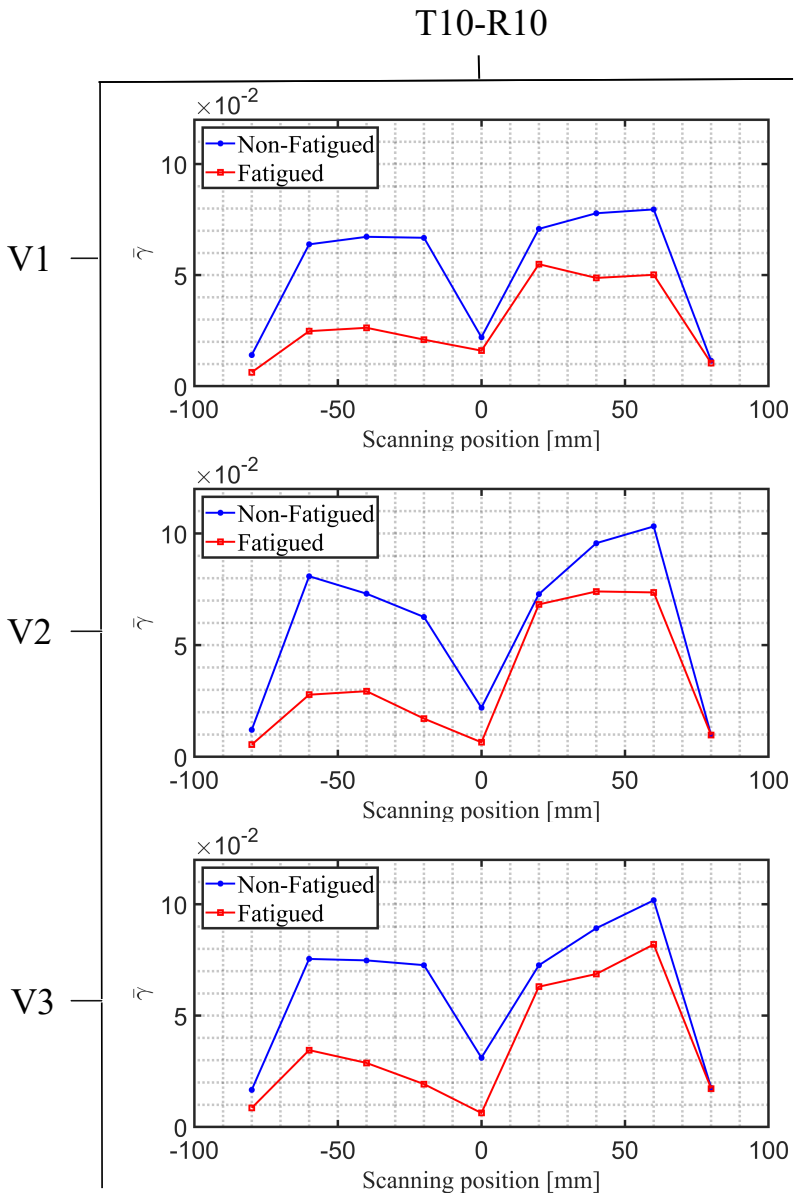

FIGURE 7.15: Average nonlinear diffuse imaging results presenting the nonlinear metric $\bar{\gamma}$ of the full image for the T10-R10 configuration on Aluminium dog bone samples for each scanning position. The fatigued and non-fatigue results are plotted for all 4 image views.

7.5 Conclusion

This chapter has attempted to resolve classical nonlinearity using previously optimised NUI methods for detecting crack tips (non-classical nonlinearity). The results from this study are in-conclusive and show that the most sensitive multi-frequency NUI configurations (T5-R5, T5-R1, T5-R10, T10-R10) are only capable of detecting nonlinear energy consistent with the baseline background noise levels. However, through averaging operations some results show an indication of non-monotonic nonlinearity from reduced nonlinear parameter levels but this is yet to be validated. Despite diffuse field time optimisation (phase coherence metric), multi-frequency optimisation and sensitivity profile control using the multi-view method, the NUI technique is not sensitive enough in its current configuration to the strain fields.

Chapter 8

Conclusion

8.1 Summary of findings

The aim of this thesis was to optimise and adapt the current nonlinear ultrasonic diffuse energy imaging (NUI) method for detecting fatigue crack tips. This is to ensure defect sensitivity is as high as possible, resulting in accurate detection and characterisation of nonlinear features.

Chapter 3 investigated the sensitivity profile of the NUI method and presented a multi-view adaptation for increased detectability. The sensitivity profile was investigated through experimental and simulation analysis. The sensitivity profiles showed consistency in the location of maximum sensitivity relative to the array for all frequencies. However, inconsistencies were observed in the distribution of the sensitivity profile, which has been attributed to exposure to the crack tip during incident excitation. When evaluating the influence of attenuation and frequency on the simulated sensitivity profile, the competing effects of increased attenuation and increased nonlinearity results in consistent nonlinear sensitivity for 1, 2.5 and 5 MHz transmission frequencies. The proposed multi-view method has proven to be effective at 5 MHz in detecting closed crack tips where the nonlinear feature is close to the array. However, the results for 1 and 2.5 MHz are inconclusive and require further investigation.

Chapter 4 presented a multi-frequency NUI method which is an adaptation of the current single frequency NUI method for detecting fatigue crack tips in three-point bend (3PB) Aluminium samples. The experimental results showed increased detectability by analysing additional nonlinear frequency components. The low and second harmonic frequency components when transmitting at 5 MHz displayed an increase in signal-to-noise ratio (SNR) by a factor of 4 and 6 respectively, compared with the current fundamental frequency method. In addition, analysis of the low frequency components allowed for detection of features with relatively lower levels of nonlinearity, which were not detectable using the single frequency method. The increase in sensitivity across multiple crack tip samples using this dual array configuration justifies the more complex configuration.

Chapter 5 investigated a diffuse phase metric for detecting fatigue crack tips in 3PB samples. Two phase metrics were investigated: offset and gradient. These metrics evaluate the change in phase between the two fields at the focal point and the study evaluated the sensitivity of this metrics through the various wave-field types (coherent, diffuse, noise). It was concluded that the phase metrics are less sensitive to a diffuse field when transmitting at 5 MHz resulting in a higher detectability of features earlier in time in the coherent wave-field. The results suggest the phase metrics would be effective in samples where a diffuse field is hard to achieve, such as larger geometries.

An effective phase coherence metric has been validated in Chapter 6 for determining the time in which the wave-field has homogenised in a structure (i.e. when the field is diffuse). The metric determines the coherence of the signals stored in a full matrix capture (FMC), when the signals are no longer coherent the metric converges, indicating a diffuse field. The convergence of the metric has been validated with NUI results capturing at different wave-field stages. The convergence of the metric strongly correlates with the time the highest SNR NUI result is captured, indicating it is correctly identifying a diffuse field. The metrics

have also proved to be robust to multiple volumes and geometries, cycle length, and various transmission frequencies. Importantly, a limitation to achieving a diffuse field with higher transmission frequencies has been established. In addition, a procedure for coupling based on a repeatability study is concluded to achieve reliable results.

Using the optimisations presented in this thesis for the NUI method, Chapter 7 attempts to resolve classical nonlinearity in fatigue samples. This study implements the multi-view NUI method determined from the sensitivity analysis, optimised multi-frequency methods, phase coherent metric for determining the diffuse time and the procedure for coupling. The results for this study conclude that there is no sensitivity to the strain field induced from bending, which suggests the NUI technique requires further optimisations to detect this type of nonlinear damage and more knowledge about how nonlinearity manifests (i.e. monotonically or non-monotonically).

8.2 Future work

Future work based on this thesis is as follows:

1. Advances in numerical models (finite element) to characterise the behaviour of nonlinear mechanisms, such as contact-acoustic nonlinearity (CAN) and material "bulk" nonlinearity, to better understand the underlying physics of the interactions. This is especially required since the sensitivity research in this thesis suggests classical and non-classical forms of nonlinearity produce different sensitivity profiles. It is also desirable to determine the level of fatigue for a given γ value from both experimental and numerical results to understand the level of fatigue and relate the metrics quantitatively to micro-features (such as roughness, corrosion and state of crack tip). This level of understanding would contribute to Chapter 4, where the multi-frequency nonlinear contributions of energy

from different transmission frequencies can be associated with different types of non-linear damage. A numerical investigation into minimum detectable nonlinearity would provide valuable insight into the detectability of classical nonlinearity. This level of analysis would provide beneficial insight into the performance of the multi-frequency NUI method for detecting strain fields in bending samples investigated in Chapter 7. This advance in modelling would greatly contribute to defect characterisation for determining the degree of fatigue and a minimum detection threshold.

2. Future work should implement the phase coherence metrics for determining the time in-which a field is diffuse, more specifically to determine the start gate-time of NUI experiments. The phase coherence metric has been validated extensively for determining when the field is diffuse and has shown to be robust to multiple parameters used in NUI. A study into determining when the diffuse field has decayed and the random noise field is approaching is key to optimising this method further. A metric for approximating the end gate-time would be valuable to improve the SNR of NUI and ultimately increase detectability.

3. This thesis has been concerned with in-contact coupling through out which is an exhaustive process considering the run time of NUI experiments. The adaptation of the NUI method to a scanning rig using immersion coupling (water) is desirable for industrial application. This process will require an investigation into achieving a diffuse field in water which may be challenging due to transmission of ultrasonic energy from the sample into the water through all surface boundaries.

Appendix A: Expansion of three-dimensional nonlinear wave equation

Prior to implementing finite difference stencils it is necessary to expand the Einstein notation for derivatives in Eq. 3.14 and 3.15. Expanding the linear derivatives in rectangular 2-dimensional space (co-ordinates 1 and 2) gives the following,

$$\frac{\partial^2 u_1^{(s)}}{\partial t^2} = 1/\rho_0 \left(\frac{\partial^2 u_1^{(s)}}{\partial x_k \partial x_k} + K + \frac{\mu}{3} \frac{\partial^2 u_l^{(s)}}{\partial x_l \partial x_1} + F_i \right) \tag{1}$$

$$\frac{\partial^2 u_1^{(s)}}{\partial t^2} = 1/\rho_0 \left(\mu \left[\frac{\partial^2 u_1^{(s)}}{\partial x_1 \partial x_1} + \frac{\partial^2 u_1^{(s)}}{\partial x_2 \partial x_2} \right] + \left(K + \frac{\mu}{3} \right) \left[\frac{\partial^2 u_1^{(s)}}{\partial x_1 \partial x_1} + \frac{\partial^2 u_2^{(s)}}{\partial x_2 \partial x_1} \right] + F_1 \right) \tag{2}$$

$$\frac{\partial^2 u_2^{(s)}}{\partial t^2} = 1/\rho_0 \left(\frac{\partial^2 u_2^{(s)}}{\partial x_k \partial x_k} + K + \frac{\mu}{3} \frac{\partial^2 u_l^{(s)}}{\partial x_l \partial x_2} + F_2 \right) \tag{3}$$

$$\frac{\partial^2 u_2^{(s)}}{\partial t^2} = 1/\rho_0 \left(\mu \left[\frac{\partial^2 u_2^{(s)}}{\partial x_1 \partial x_1} + \frac{\partial^2 u_2(s)}{\partial x_2 \partial x_2} \right] + \left(K + \frac{\mu}{3} \right) \left[\frac{\partial^2 u_1^{(s)}}{\partial x_1 \partial x_2} + \frac{\partial^2 u_2^{(s)}}{\partial x_2 \partial x_2} \right] + F_2 \right) \tag{4}$$

The nonlinear forcing term derivatives are expanded as,

$$
\begin{aligned}
F_1 = &\left(\mu + \frac{A}{4}\right)\left(\frac{\partial^2 u_l^{(0)}}{\partial x_k \partial x_k}\frac{\partial u_l^{(0)}}{\partial x_1} + \frac{\partial^2 u_l^{(0)}}{\partial x_k \partial x_k}\frac{\partial u_1^{(0)}}{\partial x_l} + 2\frac{\partial^2 u_1^{(0)}}{\partial x_l \partial x_k}\frac{\partial u_l^{(0)}}{\partial x_k}\right) + \\
&\left(K + \frac{\mu}{3} + \frac{A}{4} + B\right)\left(\frac{\partial^2 u_l^{(0)}}{\partial x_1 \partial x_k}\frac{\partial u_l^{(0)}}{\partial x_k} + \frac{\partial^2 u_k^{(0)}}{\partial x_l \partial x_k}\frac{\partial u_1^{(0)}}{\partial x_l}\right) + \\
&\left(K - \frac{2}{3\mu} + B\right)\left(\frac{\partial^2 u_1^{(0)}}{\partial x_k \partial x_k}\frac{\partial u_l^{(0)}}{\partial x_l}\right) + \left(\frac{A}{4} + B\right)\left(\frac{\partial^2 u_k^{(0)}}{\partial x_l \partial x_k}\frac{\partial u_l^{(0)}}{\partial x_1} + \frac{\partial^2 u_l^{(0)}}{\partial x_1 \partial x_k}\frac{\partial u_k^{(0)}}{\partial x_k}\right) + \\
&(B + 2C)\left(\frac{\partial^2 u_k^{(0)}}{\partial x_1 \partial x_k}\frac{\partial u_l^{(0)}}{\partial x_l}\right)
\end{aligned} \tag{5}
$$

$$
\begin{aligned}
F_1 = &\left(\mu + \frac{A}{4}\right)\left(\left[\frac{\partial^2 u_1^{(0)}}{\partial x_1 \partial x_1}\frac{\partial u_1^{(0)}}{\partial x_1} + \frac{\partial^2 u_1^{(0)}}{\partial x_2 \partial x_2}\frac{\partial u_1^{(0)}}{\partial x_1} + \frac{\partial^2 u_2^{(0)}}{\partial x_1 \partial x_1}\frac{\partial u_2^{(0)}}{\partial x_1} + \frac{\partial^2 u_2^{(0)}}{\partial x_2 \partial x_2}\frac{\partial u_2^{(0)}}{\partial x_1}\right] + \right. \\
&\left[\frac{\partial^2 u_1^{(0)}}{\partial x_1 \partial x_1}\frac{\partial u_1^{(0)}}{\partial x_1} + \frac{\partial^2 u_1^{(0)}}{\partial x_2 \partial x_2}\frac{\partial u_1^{(0)}}{\partial x_1} + \frac{\partial^2 u_2^{(0)}}{\partial x_1 \partial x_1}\frac{\partial u_1^{(0)}}{\partial x_2} + \frac{\partial^2 u_2^{(0)}}{\partial x_2 \partial x_2}\frac{\partial u_1^{(0)}}{\partial x_2}\right] + \\
&\left. 2\left[\frac{\partial^2 u_1^{(0)}}{\partial x_1 \partial x_1}\frac{\partial u_1^{(0)}}{\partial x_1} + \frac{\partial^2 u_1^{(0)}}{\partial x_1 \partial x_2}\frac{\partial u_1^{(0)}}{\partial x_2} + \frac{\partial^2 u_1^{(0)}}{\partial x_2 \partial x_1}\frac{\partial u_2^{(0)}}{\partial x_1} + \frac{\partial^2 u_1^{(0)}}{\partial x_2 \partial x_2}\frac{\partial u_2^{(0)}}{\partial x_2}\right]\right) + \\
&\left(K + \frac{\mu}{3} + \frac{A}{4} + B\right)\left(\left[\frac{\partial^2 u_1^{(0)}}{\partial x_1 \partial x_1}\frac{\partial u_1^{(0)}}{\partial x_1} + \frac{\partial^2 u_1^{(0)}}{\partial x_1 \partial x_2}\frac{\partial u_1^{(0)}}{\partial x_2} + \frac{\partial^2 u_2^{(0)}}{\partial x_1 \partial x_1}\frac{\partial u_2^{(0)}}{\partial x_1} + \frac{\partial^2 u_2^{(0)}}{\partial x_1 \partial x_2}\frac{\partial u_2^{(0)}}{\partial x_2}\right] + \right. \\
&\left.\left[\frac{\partial^2 u_1^{(0)}}{\partial x_1 \partial x_1}\frac{\partial u_1^{(0)}}{\partial x_1} + \frac{\partial^2 u_2^{(0)}}{\partial x_1 \partial x_2}\frac{\partial u_1^{(0)}}{\partial x_1} + \frac{\partial^2 u_1^{(0)}}{\partial x_2 \partial x_1}\frac{\partial u_1^{(0)}}{\partial x_2} + \frac{\partial^2 u_2^{(0)}}{\partial x_2 \partial x_2}\frac{\partial u_1^{(0)}}{\partial x_2}\right]\right) \\
&\left(K - \frac{2}{3\mu} + B\right)\left(\left[\frac{\partial^2 u_1^{(0)}}{\partial x_1 \partial x_1}\frac{\partial u_1^{(0)}}{\partial x_1} + \frac{\partial^2 u_1^{(0)}}{\partial x_2 \partial x_2}\frac{\partial u_1^{(0)}}{\partial x_1} + \frac{\partial^2 u_1^{(0)}}{\partial x_1 \partial x_1}\frac{\partial u_2^{(0)}}{\partial x_2} + \frac{\partial^2 u_1^{(0)}}{\partial x_2 \partial x_2}\frac{\partial u_2^{(0)}}{\partial x_2}\right]\right. \\
&\left(\frac{A}{4} + B\right)\left(\left[\frac{\partial^2 u_1^{(0)}}{\partial x_1 \partial x_1}\frac{\partial u_1^{(0)}}{\partial x_1} + \frac{\partial^2 u_2^{(0)}}{\partial x_1 \partial x_2}\frac{\partial u_1^{(0)}}{\partial x_1} + \frac{\partial^2 u_1^{(0)}}{\partial x_2 \partial x_1}\frac{\partial u_2^{(0)}}{\partial x_1} + \frac{\partial^2 u_2^{(0)}}{\partial x_2 \partial x_2}\frac{\partial u_2^{(0)}}{\partial x_1}\right] + \right. \\
&\left.\left[\frac{\partial^2 u_1^{(0)}}{\partial x_1 \partial x_1}\frac{\partial u_1^{(0)}}{\partial x_1} + \frac{\partial^2 u_1^{(0)}}{\partial x_1 \partial x_2}\frac{\partial u_2^{(0)}}{\partial x_1} + \frac{\partial^2 u_2^{(0)}}{\partial x_1 \partial x_1}\frac{\partial u_1^{(0)}}{\partial x_2} + \frac{\partial^2 u_2^{(0)}}{\partial x_1 \partial x_2}\frac{\partial u_2^{(0)}}{\partial x_2}\right]\right) \\
&(B + 2C)\left(\left[\frac{\partial^2 u_1^{(0)}}{\partial x_1 \partial x_1}\frac{\partial u_1^{(0)}}{\partial x_1} + \frac{\partial^2 u_2^{(0)}}{\partial x_1 \partial x_2}\frac{\partial u_1^{(0)}}{\partial x_1} + \frac{\partial^2 u_1^{(0)}}{\partial x_1 \partial x_1}\frac{\partial u_2^{(0)}}{\partial x_2} + \frac{\partial^2 u_2^{(0)}}{\partial x_1 \partial x_2}\frac{\partial u_2^{(0)}}{\partial x_2}\right]\right)
\end{aligned} \tag{6}
$$

$$
\begin{aligned}
F_2 = &\left(\mu + \frac{A}{4}\right)\left(\frac{\partial^2 u_l^{(0)}}{\partial x_k \partial x_k}\frac{\partial u_l^{(0)}}{\partial x_2} + \frac{\partial^2 u_l^{(0)}}{\partial x_k \partial x_k}\frac{\partial u_2^{(0)}}{\partial x_l} + 2\frac{\partial^2 u_2^{(0)}}{\partial x_l \partial x_k}\frac{\partial u_l^{(0)}}{\partial x_k}\right) + \\
&\left(K + \frac{\mu}{3} + \frac{A}{4} + B\right)\left(\frac{\partial^2 u_l^{(0)}}{\partial x_2 \partial x_k}\frac{\partial u_l^{(0)}}{\partial x_k} + \frac{\partial^2 u_k^{(0)}}{\partial x_l \partial x_k}\frac{\partial u_2^{(0)}}{\partial x_l}\right) + \\
&\left(K - \frac{2}{3\mu} + B\right)\left(\frac{\partial^2 u_2^{(0)}}{\partial x_k \partial x_k}\frac{\partial u_l^{(0)}}{\partial x_l}\right) + \left(\frac{A}{4} + B\right)\left(\frac{\partial^2 u_k^{(0)}}{\partial x_l \partial x_k}\frac{\partial u_l^{(0)}}{\partial x_2} + \frac{\partial^2 u_l^{(0)}}{\partial x_2 \partial x_k}\frac{\partial u_k^{(0)}}{\partial x_k}\right) + \\
&(B + 2C)\left(\frac{\partial^2 u_k^{(0)}}{\partial x_2 \partial x_k}\frac{\partial u_l^{(0)}}{\partial x_l}\right)
\end{aligned} \tag{7}
$$

$$
\begin{aligned}
F_2 = &\left(\mu + \frac{A}{4}\right)\left(\left[\frac{\partial^2 u_1^{(0)}}{\partial x_1 \partial x_1}\frac{\partial u_1^{(0)}}{\partial x_2} + \frac{\partial^2 u_1^{(0)}}{\partial x_2 \partial x_1}\frac{\partial u_1^{(0)}}{\partial x_2} + \frac{\partial^2 u_2^{(0)}}{\partial x_1 \partial x_1}\frac{\partial u_2^{(0)}}{\partial x_2} + \frac{\partial^2 u_2^{(0)}}{\partial x_2 \partial x_2}\frac{\partial u_2^{(0)}}{\partial x_2}\right] + \right. \\
&\left[\frac{\partial^2 u_1^{(0)}}{\partial x_1 \partial x_1}\frac{\partial u_2^{(0)}}{\partial x_1} + \frac{\partial^2 u_1^{(0)}}{\partial x_2 \partial x_2}\frac{\partial u_2^{(0)}}{\partial x_1} + \frac{\partial^2 u_2^{(0)}}{\partial x_1 \partial x_1}\frac{\partial u_2^{(0)}}{\partial x_2} + \frac{\partial^2 u_2^{(0)}}{\partial x_2 \partial x_2}\frac{\partial u_2^{(0)}}{\partial x_2}\right] + \\
&\left. 2\left[\frac{\partial^2 u_2^{(0)}}{\partial x_1 \partial x_1}\frac{\partial u_1^{(0)}}{\partial x_1} + \frac{\partial^2 u_2^{(0)}}{\partial x_1 \partial x_2}\frac{\partial u_1^{(0)}}{\partial x_2} + \frac{\partial^2 u_2^{(0)}}{\partial x_2 \partial x_1}\frac{\partial u_2^{(0)}}{\partial x_1} + \frac{\partial^2 u_2^{(0)}}{\partial x_2 \partial x_2}\frac{\partial u_2^{(0)}}{\partial x_2}\right]\right) + \\
&\left(K + \frac{\mu}{3} + \frac{A}{4} + B\right)\left(\left[\frac{\partial^2 u_1^{(0)}}{\partial x_2 \partial x_1}\frac{\partial u_1^{(0)}}{\partial x_1} + \frac{\partial^2 u_1^{(0)}}{\partial x_2 \partial x_2}\frac{\partial u_1^{(0)}}{\partial x_2} + \frac{\partial^2 u_2^{(0)}}{\partial x_2 \partial x_1}\frac{\partial u_2^{(0)}}{\partial x_1} + \frac{\partial^2 u_2^{(0)}}{\partial x_2 \partial x_2}\frac{\partial u_2^{(0)}}{\partial x_2}\right] + \right. \\
&\left.\left[\frac{\partial^2 u_1^{(0)}}{\partial x_1 \partial x_1}\frac{\partial u_2^{(0)}}{\partial x_1} + \frac{\partial^2 u_2^{(0)}}{\partial x_1 \partial x_2}\frac{\partial u_2^{(0)}}{\partial x_1} + \frac{\partial^2 u_1^{(0)}}{\partial x_2 \partial x_1}\frac{\partial u_2^{(0)}}{\partial x_2} + \frac{\partial^2 u_2^{(0)}}{\partial x_2 \partial x_2}\frac{\partial u_2^{(0)}}{\partial x_2}\right]\right) \\
&\left(K - \frac{2}{3\mu} + B\right)\left(\left[\frac{\partial^2 u_2^{(0)}}{\partial x_1 \partial x_1}\frac{\partial u_1^{(0)}}{\partial x_1} + \frac{\partial^2 u_2^{(0)}}{\partial x_2 \partial x_2}\frac{\partial u_1^{(0)}}{\partial x_1} + \frac{\partial^2 u_2^{(0)}}{\partial x_1 \partial x_1}\frac{\partial u_2^{(0)}}{\partial x_2} + \frac{\partial^2 u_2^{(0)}}{\partial x_2 \partial x_2}\frac{\partial u_2^{(0)}}{\partial x_2}\right]\right. \\
&\left(\frac{A}{4} + B\right)\left(\left[\frac{\partial^2 u_1^{(0)}}{\partial x_1 \partial x_1}\frac{\partial u_1^{(0)}}{\partial x_2} + \frac{\partial^2 u_2^{(0)}}{\partial x_1 \partial x_2}\frac{\partial u_1^{(0)}}{\partial x_2} + \frac{\partial^2 u_1^{(0)}}{\partial x_2 \partial x_1}\frac{\partial u_2^{(0)}}{\partial x_2} + \frac{\partial^2 u_2^{(0)}}{\partial x_2 \partial x_2}\frac{\partial u_2^{(0)}}{\partial x_2}\right] + \right. \\
&\left.\left[\frac{\partial^2 u_1^{(0)}}{\partial x_1 \partial x_2}\frac{\partial u_1^{(0)}}{\partial x_1} + \frac{\partial^2 u_1^{(0)}}{\partial x_2 \partial x_2}\frac{\partial u_2^{(0)}}{\partial x_1} + \frac{\partial^2 u_2^{(0)}}{\partial x_1 \partial x_2}\frac{\partial u_1^{(0)}}{\partial x_2} + \frac{\partial^2 u_2^{(0)}}{\partial x_2 \partial x_2}\frac{\partial u_2^{(0)}}{\partial x_2}\right]\right) \\
&(B + 2C)\left(\left[\frac{\partial^2 u_1^{(0)}}{\partial x_2 \partial x_1}\frac{\partial u_1^{(0)}}{\partial x_1} + \frac{\partial^2 u_2^{(0)}}{\partial x_2 \partial x_2}\frac{\partial u_1^{(0)}}{\partial x_1} + \frac{\partial^2 u_1^{(0)}}{\partial x_2 \partial x_1}\frac{\partial u_2^{(0)}}{\partial x_2} + \frac{\partial^2 u_2^{(0)}}{\partial x_2 \partial x_2}\frac{\partial u_2^{(0)}}{\partial x_2}\right]\right)
\end{aligned} \tag{8}
$$

Appendix B: Finite Difference Methods

Fig. 1 displays an illustration of the finite difference scheme implemented to solve the derivatives in Eq. 3.14 and 3.15, post the expansion discussed in Appendix A. The 4th order central difference technique calculates the current value i, j by fitting a quadratic polynomial to the two adjacent neighbouring points in the ith and jth directions.

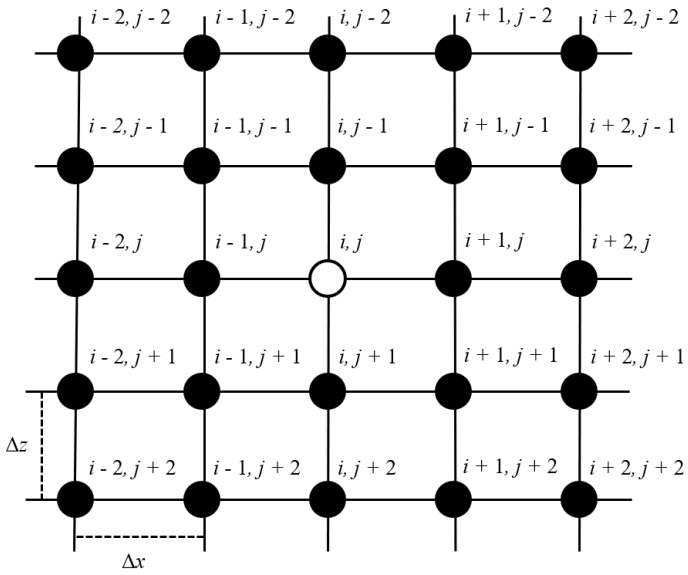

FIGURE 1: Schemetic of the 5-point FD stencil implemented

Implementing the 4th order central difference technique we define the partial derivatives for shear displacement in the x direction as,

$$\frac{\partial u_{x,i,j}}{\partial x} = \frac{u_{x,i-2,j} - 8u_{x,i-1,j} + 8u_{x,i+1,j} - u_{x,i+2,j}}{12\Delta x}, \tag{9}$$

$$\tag{10}$$

$$\frac{\partial^2 u_{x,i,j}}{\partial x^2} = \frac{-u_{x,i-2,j} + 16u_{x,i-1,j} - 30u_{x,i,j} + 16u_{x,i+1,j} - u_{x,i+2,j}}{12\Delta x^2} \tag{11}$$

and the partial derivatives for longitudinal displacement in the z direction as,

$$\frac{\partial u_{z,i,j}}{\partial z} = \frac{u_{z,i,j-2} - 8u_{z,i,j-1} + 8u_{z,i,j+1} - u_{z,i,j+2}}{12\Delta z}, \tag{12}$$

$$\tag{13}$$

$$\frac{\partial^2 u_{z,i,j}}{\partial z^2} = \frac{-u_{z,i,j-2} + 16u_{z,i,j-1} - 30u_{z,i,j} + 16u_{z,i,j+1} - u_{z,i,j+2}}{12\Delta z^2} \tag{14}$$

For mixed partial derivatives (w.r.t both x and z dimensions) the partial derivative is simplified and multiple stencils are implemented. For displacement in the x direction this can be written as,

$$\frac{\partial^2 u_{x,i,j}}{\partial z \partial x} = \frac{\partial}{\partial z}\left(\frac{\partial u_{x,i,j}}{\partial x}\right) = \frac{\frac{\partial u_{x,i,j-2}}{\partial x} - 8\frac{\partial u_{x,i,j-1}}{\partial x} + 8\frac{\partial u_{x,i,j+1}}{\partial x} - \frac{\partial u_{x,i,j+2}}{\partial x}}{12\Delta z} \tag{15}$$

and in the z direction as,

$$\frac{\partial^2 u_{z,i,j}}{\partial x \partial z} = \frac{\partial}{\partial x}\left(\frac{\partial u_{z,i,j}}{\partial z}\right) = \frac{\frac{\partial u_{z,i-2,j}}{\partial z} - 8\frac{\partial u_{z,i-1,j}}{\partial z} + 8\frac{\partial u_{z,i+1,j}}{\partial z} - \frac{\partial u_{z,i+2,j}}{\partial z}}{12\Delta x} \tag{16}$$

The time-stepping was computed using an explicit Runge-Kutta 4th (RKM4) order scheme which implements a temporal discretization to approximate the differential equations. The

RKM method is an adaptation of the Taylor Series method but does not require the computation of higher derivatives, due to the temporal discretization. The RKM4 routine has the higher-order local truncation error of the Taylor Series method but without the computational demands. The complete derivation of this method is beyond the scope of this thesis, for further reading see the publication by Mathews and Kurtis [83].

Firstly, we define the initial value problem as the second order temporal derivative in Eq. 3.14,

$$\frac{\partial^2 u}{\partial t} = f(t,u), u(t_0) = u_0 \tag{17}$$

where u is the generalised displacement values of the current time-step. The step-size h is defined and u can be calculated for the proceeding time-step,

$$u_{n+1} = u_n + \frac{1}{6}h(k_1 + 2k_2 + 2k_3 + k_4) \tag{18}$$

where $h == \Delta t$ and using,

$$\begin{aligned} k_1 &= f(t_n, u_n), \\ k_2 &= f(t_n + \frac{h}{2}, u_n + h\frac{k_1}{2}), \\ k_3 &= f(t_n + \frac{h}{2}, u_n + h\frac{k_2}{2}), \\ k_4 &= f(t_n + h, u_n + hk_3). \end{aligned} \tag{19}$$

This method was used to compute the derivatives of the wave equation over time. Note that both the first and second derivatives of this term are computed during the time-stepping process and are computed for both the longitudinal and shear components separately.

Appendix C: Fatigue crack growth

The CT test specimens described in the previous sections were loaded using a 250 kN hydraulic testing machine (INSTRON 8800) using a pair of grips and pins (see Fig. 2). The test specimen was subjected to cyclic loading at a constant amplitude to produce a fatigue crack in the specimen.

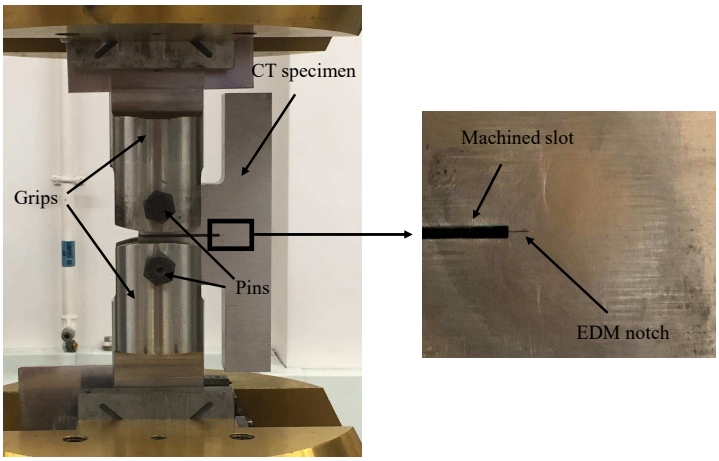

FIGURE 2: Experimental set-up of the fatigue testing for CT specimens

To establish the required loads, calculations followed the E647 ATSM (American Standard of Testing Materials). The minimum and maximum loads were determined for the cyclic loads. Firstly, the maximum stress intensity factor K_{max} was calculated,

$$K_{max} = \frac{K_{IC}}{3} \tag{20}$$

where K_{IC} is the nominal fracture toughness of the material. The minimum stress intensity factor K_{min} is calculated using Eq. 21, using a stress ratio value of $R = 0.1$. The stress ratio R, is the minimum to maximum load in a cycle and is calculated using the following relationships,

$$R = \frac{P_{min}}{P_{max}} \tag{21}$$

$$R = \frac{K_{min}}{K_{max}} \tag{22}$$

Next, the stress intensity factor range ΔK is calculated,

$$\Delta K = K_{max} - K_{min} \tag{23}$$

and finally the load range ΔP is calculated,

$$\Delta P = P_{max} - P_{min} \tag{24}$$

Complying with the ASTM standard E647-02, the geometry factor for the CT specimen is known meaning the stress intensity factor ΔK can be expressed as,

$$\Delta K = \frac{\Delta P}{B\sqrt{W}} \frac{(2+\alpha)}{(1-\alpha^{\frac{3}{2}})} (0.886 + 4.64\alpha - 13.32\alpha^2 + 14.72\alpha^3 - 5.6\alpha^4) \tag{25}$$

where B is the thickness of the specimen and $\alpha = \frac{a}{W}$. For CT specimens, a is the distance from the loading bearing points to the load of the crack tip and W is the width of the CT specimen. Following this analytical process the loads were determined for the fatigue loading

test. For aluminium this was found to be 0.5 kN and 6 kN for the minimum and maximum respectively [84].

Bibliography

[1] K. E.-A. Van Den Abeele, A. Sutin, J. Carmeliet, and P. A. Johnson, "Micro-damage diagnostics using nonlinear elastic wave spectroscopy (news)," *NDT & E International*, vol. 34, no. 4, pp. 239 – 248, 2001.

[2] I. Solodov, J. Wackerl, K. Pfleiderer, and G. Busse, "Nonlinear self-modulation and subharmonic acoustic spectroscopy for damage detection and location," *Applied Physics Letters*, vol. 84, no. 26, pp. 5386–5388, 2004.

[3] M. Ikeuchi, K. Jinno, Y. Ohara, and K. Yamanaka, "Improvement of closed crack selectivity in nonlinear ultrasonic imaging using fundamental wave amplitude difference," *Japanese Journal of Applied Physics*, vol. 52, 07 2013.

[4] O. Yoshikazu, M. Tsuyoshi, S. Ryouta, O. Toshihiro, Y. Setsu, K. Yuuki, and Y. Kazushi, "Imaging of closed cracks using nonlinear response of elastic waves at subharmonic frequency," *Applied Physics Letters*, vol. 90, no. 1, p. 011902, 2007.

[5] J. Potter, A. Croxford, and P. Wilcox, "Nonlinear ultrasonic phased array imaging," *Physical review letters*, vol. 113, p. 144301, 10 2014.

[6] J. Cheng, J. N. Potter, A. J. Croxford, and B. W. Drinkwater, "Monitoring fatigue crack growth using nonlinear ultrasonic phased array imaging," *Smart Materials and Structures*, vol. 26, p. 055006, apr 2017.

[7] V. Lubarda, "New estimates of the third-order elastic constants for isotropic aggregates of cubic crystals," *Journal of the Mechanics and Physics of Solids*, vol. 45, no. 4, pp. 471–490, 1997.

[8] S. Takahashi, "Measurement of third-order elastic constants and stress dependent coefficients for steels," *Mech Adv Mater Mod Process*, vol. 4, no. 2, 2018.

[9] L. J. GK. Matlack, J. Kim and J. Qu, "Review of second harmonic generation measurement techniques for material state determination in metals," *Journal of Nondestructive Evaluation*, vol. 34, 2015.

[10] H. Tsuda, J.-R. Lee, and Y. Guan, "Fatigue crack propagation monitoring of stainless steel using fiber bragg grating ultrasound sensors," *Smart Materials and Structures*, vol. 15, pp. 1429–1437, sep 2006.

[11] R. Thomas, B. W. Drinkwater, and D. Liaptsis, "The reflection of ultrasound from partially contacting rough surfaces," *The Journal of the Acoustical Society of America*, vol. 117, no. 2, pp. 638–645, 2005.

[12] J. M. Papazian, J. Nardiello, R. P. Silberstein, G. Welsh, D. Grundy, C. Craven, L. Evans, N. Goldfine, J. E. Michaels, T. E. Michaels, Y. Li, and C. Laird, "Sensors for monitoring early stage fatigue cracking," *International Journal of Fatigue*, vol. 29, no. 9, pp. 1668–1680, 2007. Fatigue Damage of Structural Materials VI.

[13] T. Suzuki, A. Hikata, and C. Elbaum, "Anharmonicity due to glide motion of dislocations," *Journal of Applied Physics*, vol. 35, no. 9, pp. 2761–2766, 1964.

[14] J. Zhang, F. zhen Xuan, and Y. Xiang, "Dislocation characterization in cold rolled stainless steel using nonlinear ultrasonic techniques: A comprehensive model," *EPL (Europhysics Letters)*, vol. 103, p. 68003, sep 2013.

[15] J. H. Cantrell and W. T. Yost, "Acoustic harmonic generation from fatigue-induced dislocation dipoles," *Philosophical Magazine A*, vol. 69, no. 2, pp. 315–326, 1994.

[16] I. Y. Solodov, "Ultrasonics of non-linear contacts: propagation, reflection and nde-applications," *Ultrasonics*, vol. 36, no. 1, pp. 383 – 390, 1998. Ultrasonics International 1997.

[17] I. Solodov, N. Krohn, and G. Busse, "CAN: an example of nonclassical acoustic nonlinearity in solids," *Ultrasonics*, vol. 40, no. 1, pp. 621 – 625, 2002.

[18] M. A. Breazeale and D. O. Thompson, "Finite-amplitude ultrasonic waves in aluminium," *Applied Physics Letters*, vol. 3, no. 5, pp. 77–78, 1963.

[19] A. Gedroits and V. Krasilnikov, "Finite-amplitude elastic waves in solids and deviations from hooke's law," *Soviet Phys. JETP*, vol. 16, pp. 1122–1126, 1963.

[20] Z. Su, C. Zhou, M. Hong, L. Cheng, Q. Wang, and X. Qing, "Acousto-ultrasonics-based fatigue damage characterization: Linear versus nonlinear signal features," *Mechanical Systems and Signal Processing*, vol. 45, no. 1, pp. 225–239, 2014.

[21] H. J. Lim, B. Song, B. Park, and H. Sohn, "Noncontact fatigue crack visualization using nonlinear ultrasonic modulation," *NDT & E International*, vol. 73, pp. 8–14, 2015.

[22] G. P. M. Fierro and M. Meo, "Residual fatigue life estimation using a nonlinear ultrasound modulation method," *Smart Materials and Structures*, vol. 24, no. 2, p. 025040, 2015.

[23] J. Cantrell and W. Yost, "Nonlinear ultrasonic characterization of fatigue microstructures," *International Journal of Fatigue*, vol. 23, 2001.

[24] A. Croxford, P. Wilcox, B. Drinkwater, and P. Nagy, "The use of non-collinear mixing for nonlinear ultrasonic detection of plasticity and fatigue," *The Journal of the Acoustical Society of America*, vol. 126, no. 5, pp. EL117–EL122, 2009.

[25] Z. Yan and P. Nagy, "Thermo-optical modulation for improved ultrasonic fatigue crack detection in Ti–6al–4v," *NDT & E International*, vol. 33, no. 4, pp. 213–223, 2000.

[26] Y. Ohara, K. Takahashi, Y. Ino, K. Yamanaka, T. Tsuji, and T. Mihara, "High-selectivity imaging of closed cracks in a coarse-grained stainless steel by nonlinear ultrasonic phased array," *NDT & E International*, vol. 91, pp. 139–147, 2017.

[27] J. Cheng, J. Potter, and B. Drinkwater, "The parallel-sequential field subtraction technique for coherent nonlinear ultrasonic imaging," *Smart Materials and Structures*, vol. 27, June 2018.

[28] S. Haupert, G. Renaud, and A. Schumm, "Ultrasonic imaging of nonlinear scatterers buried in a medium," *NDT & E International*, vol. 87, pp. 1 – 6, 2017.

[29] F. D. Murnaghan, "Finite deformations of an elastic solid," *American Journal of Mathematics*, vol. 59, no. 2, pp. 235–260, 1937.

[30] J. H. Cantrell, "Substructural organization, dislocation plasticity and harmonic generation in cyclically stressed wavy slip metals," *Proceedings of the Royal Society of London. Series A: Mathematical, Physical and Engineering Sciences*, vol. 460, no. 2043, pp. 757–780, 2004.

[31] P. B. Nagy, "Fatigue damage assessment by nonlinear ultrasonic materials characterization," *Ultrasonics*, vol. 36, no. 1, pp. 375 – 381, 1998. Ultrasonics International 1997.

[32] L. K. Zarembo and V. A. Krasil'nikov, "Nonlinear phenomena in the propagation of elastic waves in solids," *Soviet Physics Uspekhi*, vol. 13, pp. 778–797, jun 1971.

[33] J. Ginsberg, *Nonlinear Acoustics, Chapter10: "PerturbationMethods"*. Academic Press, 1998.

[34] E. L. L. Landau, *Theory of Elasticity (Third Edition)*. Butterworth-Heinemann, 1986.

[35] A. Moussatov, V. Gusev, and B. Castagnède, "Self-induced hysteresis for nonlinear acoustic waves in cracked material," *Phys. Rev. Lett.*, vol. 90, p. 124301, Mar 2003.

[36] B. Korshak, I. Solodov, and E. Ballad, "DC effects, sub-harmonics, stochasticity and memory for contact acoustic non-linearity," *Ultrasonics*, vol. 40, no. 1, pp. 707 – 713, 2002.

[37] C. Brotherhood, B. Drinkwater, and S. Dixon, "The detectability of kissing bonds in adhesive joints using ultrasonic techniques," *Ultrasonics*, vol. 41 (7), pp. 521 – 529, 2003.

[38] P. Blanloeuil, L. Rose, J. Guinto, M. Veidt, and C.-H. Wang, "Closed crack imaging using time reversal method based on fundamental and second harmonic scattering," *Wave Motion*, vol. 66, 06 2016.

[39] Y. Ohara, T. Mihara, and K. Yamanaka, "Effect of adhesion force between crack planes on subharmonic and dc responses in nonlinear ultrasound," *Ultrasonics*, vol. 44, no. 2, pp. 194 – 199, 2006.

[40] K. Yamanaka, T. Mihara, and T. Tsuji, "Evaluation of closed cracks by model analysis of subharmonic ultrasound," *Japanese Journal of Applied Physics*, vol. 43, no. 5B, pp. 3082–3087, 2004.

[41] R. Sasaki, T. Ogata, Y. Ohara, T. Mihara, and K. Yamanaka, "Simulation and analysis of subharmonics and tail effect for ultrasonic nondestructive evaluation of closed cracks," *Japanese Journal of Applied Physics*, vol. 44, pp. 4389–4393, jun 2005.

[42] A. L. S. A. Meziane, A. N. Norris, "Nonlinear shear wave interaction at a frictional interface: Energy dissipation and generation of harmonics," *The Journal of the Acoustical Society of America*, vol. 130, pp. 1820 – 1828, 2011.

[43] S. Best, A. Croxford, and S. Neild, "Pulse-echo harmonic generation measurements for non-destructive evaluation," *Journal of Nondestructive Evaluation*, vol. 33, no. 2, pp. 205–215, 2014.

[44] H. Jeong, S. Cho, S. Zhang, and X. Li, "Acoustic nonlinearity parameter measurements in a pulse-echo setup with the stress-free reflection boundary," *The Journal of the Acoustical Society of America*, vol. 143, no. 4, pp. EL237–EL242, 2018.

[45] J. H. Cantrell, "Ultrasonic harmonic generation from fatigue-induced dislocation substructures in planar slip metals and assessment of remaining fatigue life," *Journal of Applied Physics*, vol. 106, no. 9, p. 093516, 2009.

[46] J. Q. S. Walker, J. Kim and L. Jacobs, "Fatigue damage evaluation in a36 steel using nonlinear rayleigh surface waves," *NDT & E International*, vol. 48, pp. 10–15, 2012.

[47] J. Frouin, S. Sathish, T. E. Matikas, and J. K. Na, "Ultrasonic linear and nonlinear behavior of fatigued ti6al4v," *Journal of Materials Research*, vol. 14, no. 4, 1999.

[48] V. V. S. Jaya Rao, E. Kannan, R. V. Prakash, and K. Balasubramaniam, "Fatigue damage characterization using surface acoustic wave nonlinearity in aluminum alloy aa7175-t7351," *Journal of Applied Physics*, vol. 104, no. 12, p. 123508, 2008.

[49] J. H. Cantrell, "Fundamentals and applications of nonlinear ultrasonic nondestructive evaluation.," *Ultrasonic nondestructive evaluation*, pp. 377–448, 2003.

[50] D. C. Hurley and C. M. Fortunko, "Determination of the nonlinear ultrasonic parameter using a michelson interferometer," *Measurement Science and Technology*, vol. 8, no. 6, pp. 634–642, 1997.

[51] L. Taylor and F. Rollins, "Ultrasonic study of three-phonon interactions. i. theory," *Physical Review - PHYS REV X*, vol. 136, pp. 591–596, 11 1964.

[52] S. Liu, S. Best, S. Neild, A. Croxford, and Z. Zhou, "Measuring bulk material nonlinearity using harmonic generation," *NDT & E International*, vol. 48, 2012.

[53] G. Jones and D. Kobett, "Interaction of elastic waves in an isotropic solid," *The Journal of the Acoustical Society of America*, vol. 35, pp. 5–10, 1963.

[54] A. Demcenko, R. Akkerman, P. Nagy, and R. Loendersloot, "Non-collinear wave mixing for non-linear ultrasonic detection of physical ageing in pvc," *NDT & E International*, vol. 49, pp. 34 – 39, 2012.

[55] J. Alston, A. Croxford, J. Potter, and P. Blanloeuil, "Nonlinear non-collinear ultrasonic detection and characterisation of kissing bonds," *NDT & E International*, vol. 99, pp. 105 – 116, 2018.

[56] J. Jiao, H. Lv, C. He, and B. Wu, "Fatigue crack evaluation using the non-collinear wave mixing technique," *Smart Materials and Structures*, vol. 26, p. 065005, may 2017.

[57] C. R. Courtney, B. W. Drinkwater, S. A. Neild, and P. D. Wilcox, "Factors affecting the ultrasonic intermodulation crack detection technique using bispectral analysis," *NDT & E International*, vol. 41, no. 3, pp. 223 – 234, 2008.

[58] M. Meo and G. Zumpano, "Nonlinear elastic wave spectroscopy identification of impact damage on a sandwich plate," *Composite Structures*, vol. 71, no. 3, pp. 469 – 474, 2005. Fifth International Conference on Composite Science and Technology.

[59] M. Meo, U. Polimeno, and G. Zumpano, "Detecting damage in composite material using nonlinear elastic wave spectroscopy methods," *Applied Composite Materials*, vol. 15, pp. 115–126, 5 2008.

[60] T. J. Ulrich, P. A. Johnson, and R. A. Guyer, "Interaction dynamics of elastic waves with a complex nonlinear scatterer through the use of a time reversal mirror," *Phys. Rev. Lett.*, vol. 98, p. 104301, Mar 2007.

[61] A. Clay, S. Wooh, and L. Azar, "Experimental study of phased array beam steering characteristics," *Journal of Nondestructive Evaluation*, vol. 18, pp. 59 – 71, 1999.

[62] P. Wells, "Ultrasonics: A window into biomedical science," *Ultrasonics*, vol. 30, no. 1, pp. 3 – 7, 1992.

[63] C. Holmes, B. Drinkwater, and P. Wilcox, "Post-processing of the full matrix of ultrasonic transmit-receive array data for non-destructive evaluation," *NDT & E International*, vol. 38, pp. 701–711, 12 2005. Publisher: Elsevier Other: in press.

[64] D. H. Simpson, C. T. Chin, and P. N. Burns, "Pulse inversion doppler: a new method for detecting nonlinear echoes from microbubble contrast agents," *IEEE Transactions on Ultrasonics, Ferroelectrics, and Frequency Control*, vol. 46, no. 2, pp. 372–382, 1999.

[65] G. A. Brock-Fisher, "Means for increasing sensitivity in non-linear ultrasound imaging systems," *Acoustical Society of America Journal*, vol. 101, p. 3240, June 1997.

[66] J. Potter and A. J. Croxford, "Characterization of nonlinear ultrasonic diffuse energy imaging," *IEEE Transactions on Ultrasonics, Ferroelectrics, and Frequency Control*, vol. 65, pp. 870–880, May 2018.

[67] G. F. Miller and H. Pursey, "The field and radiation impedance of mechanical radiators on the free surface of a semi-infinite isotropic solid," *Proceedings of the Royal Society of London. Series A, Mathematical and Physical Sciences*, vol. 223, no. 1155, pp. 521–541, 1954.

[68] J. Zhang, Y. Song, X. Li, and C. Zhong, "Comparison of experimental measurements of material grain size using ultrasound," *Journal of Nondestructive Evaluation*, vol. 39, Mar. 2020.

[69] L. Brillouin, "Les tensions de radiation ; leur interprétation en mécanique classique et en relativité," *J. Phys. Radium*, vol. 6, no. 11, pp. 337–353, 1925.

[70] D. S. Hughes and J. L. Kelly, "Second-order elastic deformation of solids," *Phys. Rev.*, vol. 92, pp. 1145–1149, Dec 1953.

[71] R. Weaver, "Diffusivity of ultrasound in polycrystals," *Journal of the Mechanics and Physics of Solids*, vol. 38, no. 1, pp. 55 – 86, 1990.

[72] K. G. Sabra, P. Roux, and W. A. Kuperman, "Arrival-time structure of the time-averaged ambient noise cross-correlation function in an oceanic waveguide," *The Journal of the Acoustical Society of America*, vol. 117, no. 1, pp. 164–174, 2005.

[73] P. Roux, K. G. Sabra, W. A. Kuperman, and A. Roux, "Ambient noise cross correlation in free space: Theoretical approach," *The Journal of the Acoustical Society of America*, vol. 117, no. 1, pp. 79–84, 2005.

[74] A. Duroux, K. G. Sabra, J. Ayers, and M. Ruzzene, "Extracting guided waves from cross-correlations of elastic diffuse fields: Applications to remote structural health monitoring," *The Journal of the Acoustical Society of America*, vol. 127, no. 1, pp. 204–215, 2010.

[75] M. J. Evans and P. Cawley, "Measurement and prediction of diffuse fields in structures," *The Journal of the Acoustical Society of America*, vol. 106, no. 6, pp. 3348–3361, 1999.

[76] R. L. Weaver, "On diffuse waves in solid media," *The Journal of the Acoustical Society of America*, vol. 71, no. 6, pp. 1608–1609, 1982.

[77] R. L. Weaver, "Equipartition and mean-square responses in large undamped structures," *The Journal of the Acoustical Society of America*, vol. 110, no. 2, pp. 894–903, 2001.

[78] R. L. Weaver and I. Lobkis, "Diffuse fields in open systems and the emergence of the Green's function (l)," *The Journal of the Acoustical Society of America*, vol. 116, no. 5, pp. 2731–2734, 2004.

[79] O. I. Lobkis and R. L. Weaver, "On the emergence of the Green's function in the correlations of a diffuse field," *The Journal of the Acoustical Society of America*, vol. 110, no. 6, pp. 3011–3017, 2001.

[80] K. Sabra, A. Srivastava, F. Lanza di Scalea, I. Bartoli, P. Rizzo, and S. Conti, "Structural health monitoring by extraction of coherent guided waves from diffuse fields," *The Journal of the Acoustical Society of America*, vol. 123, pp. EL8–13, 02 2008.

[81] J. Cheng, *Nonlinear Ultrasonic Imaging Techniques for Non-Destructive Testing*. PhD thesis, University of Bristol, 10 2018.

[82] S. Baby, B. Nagaraja Kowmudi, C. Omprakash, D. Satyanarayana, K. Balasubramaniam, and V. Kumar, "Creep damage assessment in titanium alloy using a nonlinear ultrasonic technique," *Scripta Materialia*, vol. 59, no. 8, pp. 818–821, 2008.

[83] Mathews and K. Fink, *Numerical methods using MATLAB*. Prentice-Hall of India, 2005.

[84] D. Liaptsis, "The ultrasonic detectability and sizing of rough partially closed cracks in real structures," 2008.